

1N-02
199886
103P

Aerodynamic Characteristics and Pressure Distributions for an Executive-Jet Baseline Airfoil Section

Dennis O. Allison and Raymond E. Mineck

DECEMBER 1993

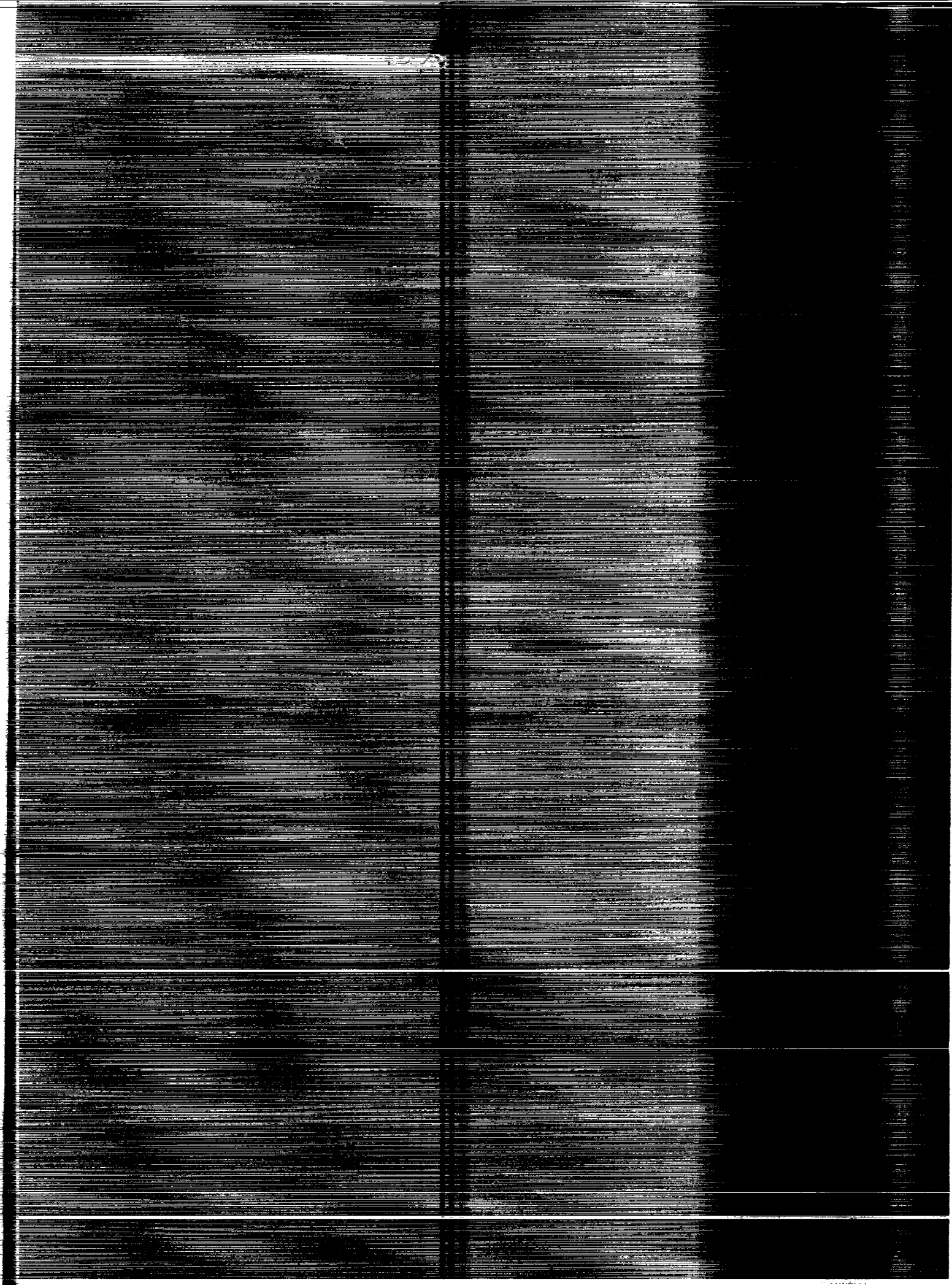
N94-24586

Unclass

H1/02 0199886

(NASA-TM-4529) AERODYNAMIC
CHARACTERISTICS AND PRESSURE
DISTRIBUTIONS FOR AN EXECUTIVE-JET
BASELINE AIRFOIL SECTION (NASA)
103 p

NASA



NASA Technical Memorandum 4529

Aerodynamic Characteristics and Pressure Distributions for an Executive-Jet Baseline Airfoil Section

Dennis O. Allison and Raymond E. Mineck
Langley Research Center
Hampton, Virginia



National Aeronautics and
Space Administration

Office of Management

Scientific and Technical
Information Program

1993

Contents

Summary	1
Introduction	1
Symbols	1
Wind Tunnel	2
Test Section	2
Wake Rake	2
Model	2
Test Instrumentation	3
Tunnel Flow Conditions	3
Airfoil Model Pressures	3
Wall and Wake Pressures	3
Procedures	3
Data Reduction	4
Integrated Coefficients	4
Two-Dimensional Flow	4
Presentation of Data	5
Data Repeatability	5
Force and Moment Coefficients	5
Chordwise Pressure Distributions	6
Free Transition	6
Concluding Remarks	7
Appendix—Data for $c_n > 1.2$	8
References	12
Tables	13
Figures	17

Summary

A wind tunnel test of an executive-jet baseline airfoil model was conducted in the adaptive-wall test section of the NASA Langley 0.3-Meter Transonic Cryogenic Tunnel. The primary goal of the test was to measure airfoil aerodynamic characteristics over a wide range of flow conditions that encompass two design points. The two design Mach numbers were 0.654 and 0.735 with corresponding Reynolds numbers of 4.5×10^6 and 8.9×10^6 based on chord, respectively, and normal-force coefficients of 0.98 and 0.51, respectively. The tests were conducted over a Mach number range from 0.250 to 0.780 and a chord Reynolds number range from 3.0×10^6 to 18.0×10^6 . The angle of attack was varied from -2° to a maximum below 10° with one exception in which the maximum was 14° for a Mach number of 0.250 at a chord Reynolds number of 4.5×10^6 . Boundary-layer transition was fixed at 5 percent of chord on both the upper and lower surfaces of the model for most of the test. The adaptive-wall test section had flexible top and bottom walls and rigid sidewalls. Wall interference was minimized by the movement of the adaptive walls, and the airfoil aerodynamic characteristics were corrected for any residual top and bottom wall interference.

The data are presented graphically as integrated force and moment coefficients and chordwise pressure distributions. For increasing Mach number, the maximum normal-force coefficient decreases. With increasing Mach number at a constant normal-force coefficient in the linear region, an increase occurs in the variation of normal-force coefficient with angle of attack, in the negative pitching-moment coefficient, and in the drag coefficient. With increasing Reynolds number at a constant normal-force coefficient, the negative pitching-moment coefficient becomes more negative and the drag coefficient decreases. The pressure distributions reveal that separation begins at the trailing edge. Free transition results in lower drag coefficients and slightly stronger negative pitching-moment coefficients.

Introduction

The Langley Research Center has been involved in a cooperative program with the Cessna Aircraft Company to design and test preliminary airfoils and wings for a proposed executive-jet configuration. The objective of this program was to apply Langley-developed advanced computational fluid dynamics (CFD) design methods to improve the overall performance of a baseline executive-jet configuration. Part of the cooperative program involved a baseline airfoil and two design points that were pro-

vided by the Cessna Aircraft Company. The design points were for low- and high-speed cruise and consisted of the following combinations of Mach number, chord Reynolds number, and normal-force coefficient: 0.654, 4.5×10^6 , and 0.98, respectively; and 0.735, 8.9×10^6 , and 0.51, respectively. A multipoint design approach which used the Constrained Direct Iterative Surface Curvature (CDISC) design method (ref. 1) was used to design a modified airfoil that had a lower predicted wave drag at both design points.

The purpose of the current paper is to present wind tunnel aerodynamic characteristics for the baseline airfoil. The tests were conducted in the Langley 0.3-Meter Transonic Cryogenic Tunnel (0.3-m TCT) for Mach numbers from 0.250 to 0.780 and chord Reynolds numbers from 3.0×10^6 to 18.0×10^6 . The angle of attack ranged from -2° to a maximum below 10° with one exception in which the maximum was 14° for a Mach number of 0.250 at a chord Reynolds number of 4.5×10^6 . The upper limit on angle of attack was usually determined by model stall and sometimes by the inability of the adaptive walls to adjust to high lift levels. Boundary-layer transition was fixed at 5 percent of chord on both the upper and lower surfaces of the airfoil model for most of the test. The 6-in-chord model spanned the width of the test section and was instrumented for chordwise pressure distribution measurements. A wake rake was used to measure pressure losses for drag determination.

Symbols

The measurements and calculations were made in the U.S. Customary Units. The symbols used in this report are defined as follows:

c	model chord ($c = 6$ in.)
c_d	section drag coefficient, measured on tunnel centerline
c_m	section pitching-moment coefficient, resolved about $x = 0.25c$
c_n	section normal-force coefficient
$c_{n,\max}$	section maximum normal-force coefficient
C_p	local pressure coefficient
C_p^*	pressure coefficient for sonic condition
D	diameter
M_∞	free-stream Mach number
Re_c	free-stream Reynolds number based on model chord

x	chordwise position, measured aft from leading edge, in.
y	vertical position, measured up from model chord plane, in.
α	angle of attack, deg

Wind Tunnel

The tests were conducted in the 13- by 13-in. two-dimensional adaptive-wall test section of the Langley 0.3-m TCT. A sketch of the tunnel is presented in figure 1, and a photograph of the upper leg of the tunnel circuit is presented in figure 2. The 0.3-m TCT is a fan-driven, cryogenic pressure tunnel that uses gaseous nitrogen as a test medium. It is capable of operating at stagnation temperatures from just above the boiling point of liquid nitrogen (approximately 144°R (80 K)) to 589°R (327 K) and at stagnation pressures from 1.2 to 6.0 atm. The fan speed is variable so that the empty test section Mach number can be varied continuously from about 0.20 to 0.95. This combination of test conditions provides a test envelope of chord Reynolds numbers up to about 50×10^6 based on a model chord of 6 in. Additional details of the tunnel may be found in reference 2. Wind tunnels with adaptive walls attempt to eliminate the wall-induced interference at its source. This is accomplished by modifying the flow field near the test section boundaries such that the flow field in the vicinity of the model duplicates "free air" conditions. Specific details of the method are given in reference 3.

Test Section

Sketches of the adaptive-wall test section with the plenum sidewall removed are presented in figure 3, and photographs of the test section region are presented in figures 4 and 5. The model mounting system is designed for two-dimensional models with chords up to 13 in. A model is supported between two turntables centered 30.7 in. downstream of the test section entrance. The turntables are driven by an electric stepper motor that is connected through a yoke to the perimeter of both turntables. This arrangement drives both turntables to eliminate possible model twisting. The angular position of the turntables, and therefore the geometric angle of attack of the model, is measured using a digital shaft encoder geared to the left turntable.

The test section is 13 in. by 13 in. at the entrance, and all four walls are solid. The sidewalls are rigid whereas the top and bottom walls are flexible and movable. The flexible walls are 71.7 in. long and are anchored at the upstream end. The rear 15.9-in. portion diverges 4.1° to form a transition between the

test section and the high-speed diffuser. The test section is therefore considered to be 55.8 in. long. The shape of each wall is determined by 21 independent jacks. The jack locations relative to the center of the model-mounting turntable are presented in table 1. Each wall-positioning jack is driven by a stepper motor located outside the test section plenum. The jacks have a design displacement range of 3 in. up and 1 in. down. However, the available displacement for each jack varies because of limits on allowable wall stress due to curvature. Pressure orifices are located on the top and bottom wall centerlines at the jack positions and 1.0 in. upstream of the wall anchor point. The jack at -1.75 in. (upstream of the turntable) on the bottom wall was inoperative during this test. Because the connection between this jack and the flexible wall was removed, the wall displacement could not be determined at this station. The wall was free to "float" to a position determined by the jack just upstream and the jack just downstream of the inoperative jack.

Wake Rake

A horizontal rake is used to survey the wake pressure field. A vertical traversing mechanism moves the rake within the limits of 3 in. below to 5 in. above the centerline. The traversing mechanism is driven by a stepper motor mounted externally to the tunnel, and the number of steps used to traverse the wake is 75 for this test. The vertical position of the traversing mechanism is measured by a digital shaft encoder geared to the stepper motor. The traversing mechanism supports a wake rake with three static and six total pressure probes (tubes), as shown in figure 6. This arrangement allows the total pressure variation in the model wake to be determined at six spanwise locations. The wake rake can be installed at one of three streamwise stations, the forward, center, and rear stations, which are located at 12.5, 17.5, and 22.5 in., respectively, downstream of the center of the turntable. The wake rake should be 1 or 2 chords or more downstream of the model trailing edge to avoid aerodynamic interference with the model. For this test, the wake rake is located at the center station (fig. 7), which is 2.17 model chords downstream of the model trailing edge.

Model

The model used in this test was supported by mounting blocks, as shown in figure 8, and the blocks were bolted to the tunnel-wall turntables. The model chord was on the test section centerline, and the angle of attack was changed by rotation about the 0.513c position. The model had a 6-in. chord, a 13-in.

span, and a baseline airfoil section that was $0.115c$ thick with the maximum thickness at $0.31c$. The leading-edge radius was $0.016c$. The design and measured model coordinates are presented in tables 2 and 3, respectively, and a sketch of the airfoil section is presented in figure 9. The maximum difference between the measured profile and the design profile was $0.0004c$.

The model was equipped with 46 pressure orifices: 20 on the lower surface in a chordwise row at the spanwise center and 26 on the upper surface in an offset chordwise row. For ease of fabrication, the upper surface row of orifices was offset 0.5 in. to the right from the spanwise center and the upper surface orifices in the nose region (for $x < 0.4$ in.) were staggered to within ± 0.05 in. in the spanwise direction. The chordwise orifice locations, which are shown in the airfoil sketch in figure 9 are listed in table 4. All the orifices were 0.010 in. in diameter.

Test Instrumentation

A detailed discussion of the instrumentation and procedures for the calibration and control of the 0.3-m TCT can be found in reference 4. For two-dimensional airfoil tests, the 0.3-m TCT is equipped to obtain static pressure measurements on the airfoil model surface, total pressure measurements in the model wake, and static pressure measurements on the test section sidewalls, top wall, and bottom wall. The following sections describe instrumentation for tunnel flow conditions, airfoil model pressures, wall pressures, and wake pressures.

Tunnel Flow Conditions

The tunnel flow conditions are determined by three primary measurements: total pressure, static pressure, and total temperature. The total pressure and static pressure are measured by individual quartz differential pressure transducers referenced to a vacuum to function as absolute pressure devices. Each transducer has a range of ± 100 psi and an accuracy of ± 0.006 psi plus ± 0.012 percent of the pressure reading. The stagnation temperature is measured by a platinum resistance thermometer. The analog output from each of these devices is converted to digital form by individual digital voltmeters for display and recording.

Airfoil Model Pressures

The pressures on the airfoil model are measured by individual transducers connected by tubing to each orifice on the model. The transducers are a high-precision variable-capacitance type. The

maximum range of these differential transducers is ± 100 psi with an accuracy of ± 0.25 percent of the reading from -25 percent to 100 percent of full scale. They are located outside the high-pressure cryogenic environment of the tunnel but as close as possible to the test section to minimize the tubing length and reduce the response time. To provide increased accuracy, the transducers are mounted on thermostatically controlled heater bases to maintain a constant temperature and on "shock" mounts to reduce possible vibration effects. The electrical signals from the transducers are processed by individual signal conditioners located in the tunnel control room. The signal conditioners are autoranging and have seven ranges available. As a result of the autoranging capability, the analog output to the data acquisition system is kept at a high level even though the pressure transducer may be operating at the low end of its range.

Wall and Wake Pressures

The top and bottom flexible-wall pressures are measured using a pressure scanning system operating two 48-port valves. Because of the large changes in the pressure of the tunnel over its operational range, the same type of variable-capacitance pressure transducers and autoranging signal conditioners described above are used with the pressure scanning system instead of the more typical strain gauge transducer.

The total pressure loss in the model wake is measured with the rake described previously. The pressure in each of the six total pressure tubes is measured with the same type of variable-capacitance pressure transducer described above but with a maximum range of ± 20 psi. The static pressure in the model wake is the average of measured pressures on the right sidewall at eight vertical positions at the tunnel station of the wake rake (which is on the left sidewall). The static pressure probes on the rake were not used because they have not provided reliable data in the past.

Procedures

Test conditions were chosen to cover a wide range of Mach numbers and Reynolds numbers that encompass two design points ($M_\infty = 0.654$, $R_c = 4.5 \times 10^6$, and $c_n = 0.98$; and $M_\infty = 0.735$, $R_c = 8.9 \times 10^6$, and $c_n = 0.51$). Table 5 shows the combinations of M_∞ versus R_c (written herein as M_∞ - R_c) in the test program, and dashed underlines indicate the combinations for the two design points. Figure numbers are listed in table 5 for each M_∞ - R_c combination in the program as an aid to locating pressure data for given test conditions. (The Mach numbers in the text, in

table 5, and in the figure titles are nominal values, whereas the Mach numbers in the figure keys are slightly different because they are measured values.)

Most of the test was conducted with transition strips placed at the 5-percent-chord location on both surfaces of the model so that boundary-layer transition locations would be known. The authors assumed that the 5-percent-chord location would be behind the stagnation point and in front of the natural transition location on both surfaces of the model for the conditions of this test. The grit size was determined by using the method of reference 5 for a Reynolds number of 9×10^6 per foot ($R_c = 4.5 \times 10^6$). The glass compound transition grit used for this test was class 5 close-sized unispheres of 0.0016-in. nominal diameter, and the strips were approximately $1/16$ in. wide. The transition strips were removed near the end of the test and some free-transition data were taken.

The following procedure was used to set the test conditions. The tunnel total pressure, total temperature, and fan speed were set for the desired Mach number and Reynolds number, and the model turntable was adjusted to the desired angle of attack. When the test conditions became stable, the wall-adaptation process in reference 3 was initiated, and after completion, the flexible-wall position and static pressures associated with the adapted walls were recorded on the data tape. Twenty samples of the airfoil static pressures, the test conditions, the wake rake total pressures, and the wake static pressures were then recorded during a 1-sec interval. Each sample consisted of simultaneous static pressure readings from all orifices on the model. The wake rake was moved to the next vertical location and another 20 samples of wake data were recorded. Wake data were obtained at 75 vertical locations of the model wake rake.

Data Reduction

Because the tunnel operating envelope included high pressures and low temperatures, real-gas effects were included in the data reduction for the tunnel test conditions using the thermodynamic properties of nitrogen gas calculated from the Beattie-Bridgeman equation of state. This equation of state was shown in reference 6 to give essentially the same thermodynamic properties and flow calculation results as were given by the more complicated Jacobsen equation of state for the temperature-pressure realm of the 0.3-m TCT. Detailed discussions of real-gas effects when testing in cryogenic nitrogen were given in references 7 and 8. Wall interference was minimized by appropriate movement of the flexible (adaptive)

walls. The method of reference 9 was used to correct the data for any residual top and bottom wall interference effects.

Integrated Coefficients

Section normal-force and pitching-moment coefficients were calculated by integration of measured surface pressures. A polynomial curve fit (ref. 10) of the measured pressure coefficients was used to enrich the distribution of points by a factor of 10, followed by the trapezoidal method of integration. A gap occurred in the measured pressure distribution from $x = 0.0107c$ to $0.0604c$ on the upper surface because three successive orifices had leaks inside the model and thus were missing in the reduced data. The slope of the pressure distribution at $x = 0.0107c$ was not defined well enough for a meaningful curve fit in the region of the missing orifices. Therefore, a pressure coefficient, taken as the average of those for the orifices at $x = 0.0048c$ and $0.0107c$, was added at an x position determined by quadratic interpolation using pressure coefficients from the orifices at $x = 0.0000c$, $0.0048c$, and $0.0107c$. Linear interpolation was used when, for $\alpha \approx -2^\circ$, the coefficient of the squared term in the quadratic interpolation equation was negative because the negative term caused the curvature to be incompatible with that of the experimental data. The result was that in the region of the missing orifices, the character of the curve fits with the interpolated point more closely resembled the character of pressure distributions predicted by the two-dimensional (2D) transonic full-potential code of reference 11. Figure 10 illustrates the result of this process for the flow condition in which $M_\infty \approx 0.700$, $R_c = 6.5 \times 10^6$, and $c_n = 0.69$ ($\alpha = 2.1^\circ$).

The section drag coefficient was calculated from the wake survey pressures by first computing an incremental or point drag coefficient by the method of reference 12 for each rake tube total pressure at each rake location. These point drag coefficients were then numerically integrated across the model wake in the vertical direction using the trapezoidal method. The results of this integration are total drag coefficients at each of the six spanwise locations of the wake rake total pressure tubes. All drag data presented in this report are for the total pressure tube on the tunnel centerline.

Two-Dimensional Flow

The pressure data for each of the six total pressure tubes were examined to ensure that the wake survey covered the entire wake and to determine when two-dimensional flow was not present across

the model. The data from the tube that was 1 in. from the sidewall (fig. 6) were not consistent with the data from the other five total pressure tubes, probably because this tube is immersed in the combined sidewall boundary layer and model wake. Therefore, this tube was not included in the final data reduction. An examination of the spanwise distributions of section drag coefficient showed that as the normal-force coefficient increased above a certain level, the section drag began to vary across the span, an indication that two-dimensional flow was beginning to break down. This c_n level decreased with increasing Mach number. The flow was considered to be two dimensional when the section drag coefficient was within ± 10 percent of the section drag coefficient at the centerline of the tunnel. Two-dimensional flow was measured across the centerline and two adjacent total pressure tubes (at least one-third of the model span) for normal-force coefficients up to 0.1 below the maximum normal-force coefficient for each run. Caution should be exercised when using data in which the normal-force coefficient is close to the maximum (within 0.1 of $c_{n,\max}$) for a given Mach number.

Presentation of Data

The data from this test are presented graphically and were taken with fixed transition except where noted. Data repeatability is presented, which is followed by the effects of M_∞ and R_c on integrated force and moment coefficients. Then, the effect of α on chordwise pressure distributions at all 26 flow conditions is presented. Finally, the limited amount of data available for free transition is presented.

Data Repeatability

Data repeatability for the wind tunnel test was examined by repeating an angle-of-attack variation at a given subsonic condition and then by repeating one angle of attack at a given transonic condition several times during the test. An angle-of-attack variation at $M_\infty \approx 0.250$ and $R_c = 4.5 \times 10^6$, which was a tunnel checkout run on the first day of the test (run A in fig. 11), was repeated (run B in fig. 11) on the second day. For those two runs, force and moment data were compared (figs. 11(a) and 11(b)) and pressure distributions for angles of attack of 0° and 5° were compared (fig. 11(c)). Subsequently during the test, a case at $\alpha = 4^\circ$ from an early transonic run (run A in fig. 12) was repeated four times (runs B, C, D, and E in fig. 12). Force and moment data were compared (figs. 12(a) and 12(b)), and pressure distributions were compared for two points with a similar normal-force coefficient (runs A and E in fig. 12(c)).

Some small differences were evident in the repeated data. An angle-of-attack disagreement of about 0.1° occurred in figure 11(a) for $c_n = 0.50$ to 0.70 and in figure 12(a) for $c_n = 0.96$. (See the triangle symbol for run D.) This uncertainty may relate to some play in the mechanism that measures the angle of attack. Repeatability of c_m is very good (fig. 11(a)) and repeatability of c_d is approximately 0.0002 – 0.0003 (fig. 11(b)). A consistent (but small) shift occurred in the C_p level on both the upper and lower surfaces between runs A and B for $\alpha = 0^\circ$ in figure 11(c), even though the measured Mach number was exactly 0.250 for the data points in figure 11(c). Because this type of shift is not present for $\alpha = 5^\circ$, it may be due to some adjustment that may have been made during the tunnel checkout that was in progress during run A of figure 11. The pressure distribution comparisons for $\alpha = 5^\circ$ in figure 11(c) and $\alpha = 4^\circ$ in figure 12(c) show a small shift in the upper surface C_p level for $x/c = 0$ to 0.4 , which is explained by a small difference in α (and the corresponding c_n values) between the two points in each case. The data from run B in figure 11 and from run A in figure 12 are included in the following data without the designation of run A or run B.

Force and Moment Coefficients

The effect of free-stream Mach number on integrated force and moment coefficients at a constant Reynolds number is presented in figure 13 for the following five Reynolds numbers: 3.0×10^6 , 4.5×10^6 , 6.5×10^6 , 9.0×10^6 , and 13.5×10^6 . The data at $R_c = 4.5 \times 10^6$ (figs. 13(c) and 13(d)) are replotted in the appendix (fig. A1) with different scales to show the data for $c_n > 1.2$ at $M_\infty \approx 0.250$. For the data at constant Reynolds number, the general trends with increasing Mach number are described as follows: the maximum normal-force coefficient decreases; and, for a constant c_n in the linear c_n - α range, the c_n - α slope increases, the negative pitching moment becomes more negative, and the drag coefficient increases. However, the drag coefficient in the linear c_n - α range at $R_c = 9.0 \times 10^6$ (fig. 13(h)) for $M_\infty \approx 0.250$ is larger than that for $M_\infty \approx 0.500$. This trend reversal is suspected to have been caused by boundary-layer transition ahead of the transition strips which could result from a high turbulence level at $M_\infty \approx 0.250$. The tunnel total pressure for a constant Reynolds number was higher at $M_\infty \approx 0.250$ than it was at $M_\infty \approx 0.500$.

The effect of free-stream Reynolds number at a constant Mach number on integrated force and moment coefficients is presented in figure 14 for Mach numbers of 0.250 , 0.500 , 0.600 , 0.655 , 0.670 ,

0.700, 0.735, and 0.760. The effect of Reynolds number on normal-force coefficient is small. (See especially figs. 14(g) and 14(m).) Part of the effect may be caused by some play in the mechanism that measures angle of attack as mentioned previously in the discussion of figure 11(a) in the section "Data Repeatability," where α was found to be repeatable only within $\pm 0.1^\circ$. The effect is in the direction of a higher normal-force coefficient at a higher Reynolds number, which is expected, because the aft camber in the airfoil can be effectively reduced by the boundary layer. As Reynolds number increases, the boundary layer becomes thinner and less effective at reducing aft camber. The negative pitching moment becomes more negative with increasing Reynolds numbers, which is also expected, because a thinner boundary layer is less effective at decambering over the rear part of the airfoil.

For low drag levels ($c_d < 0.01$), drag coefficient at a constant c_n decreases with increasing Reynolds number for Mach numbers up to 0.735. This trend is expected because skin-friction drag decreases as Reynolds number increases. This general trend is not seen at $M_\infty \approx 0.760$ (fig. 14(p)). For $M_\infty \approx 0.760$ at $c_n \approx -0.05$, 0.2, and 0.4, the presence of shock waves can be seen in the pressure distributions presented in figure 15. (Note that the level of the sonic pressure coefficient (C_p^*) is indicated.) As Reynolds number is increased, the increases in wave drag can overcome decreases in friction drag. At $c_n \approx -0.05$, the drag coefficient increases as Reynolds number increases (fig. 14(p)) because the lower surface shock wave becomes stronger (fig. 15(a)). However, for $c_n \approx 0.2$, the drag coefficient decreases as R_c increases from 4.5×10^6 to 6.5×10^6 ; then, for $R_c = 9.0 \times 10^6$ the drag coefficient does not decrease farther (fig. 14(p)) because the shock waves on both airfoil surfaces become stronger (fig. 15(b)). At $c_n \approx 0.4$, the drag coefficient again increases as Reynolds number increases (fig. 14(p)) because the upper surface shock wave becomes stronger (fig. 15(c)).

Chordwise Pressure Distributions

The effect of angle of attack on chordwise pressure distributions is presented in figures 16 to 24 for the program of M_∞ - R_c test conditions in table 5. In figures 17 to 24 the level of the sonic pressure coefficient (C_p^*) is included as an aid in understanding which areas on the model have local supersonic or near-supersonic flow. The C_p scale increment per grid division is changed from -0.4 to -0.2 for figures 22 to 24 to better display the features of the pressure distributions at high Mach numbers.

The plotted pressure distributions for each M_∞ - R_c combination include a representative set of four or five angles of attack which is sufficient for covering the available range of data and illustrating the onset of separation. The following comments apply to figures A2 and 17 to 24. (See, for example, fig. 17(a).) The behavior of the upper surface suction peak indicates that separation does not begin at the leading edge. As angle of attack increases, the upper surface suction peak near the leading edge remains intact as the positive trailing-edge pressure coefficient begins to become more negative, a result which indicates that separation begins at the trailing edge. The data in figures 18 to 24 (see, for example, fig. 18(a)) show that as angle of attack increases, the upper surface shock wave reaches a maximum rearward location, and then moves forward as separation begins.

Free Transition

Free-transition data were obtained at the end of the test at the following five combinations of M_∞ - R_c : 0.655 - 4.5×10^6 , 0.735 - 4.5×10^6 , 0.700 - 6.5×10^6 , 0.655 - 9.0×10^6 , and 0.735 - 9.0×10^6 . The effect of fixed transition on force and moment coefficients is presented in figure 25, and the effect of angle of attack on pressure distributions with free transition is presented in figure 26. The effects of fixed transition on c_n and c_m discussed below are illustrated at the M_∞ - R_c combinations for the two design points (0.655 - 4.5×10^6 and 0.735 - 9.0×10^6) by showing the effect of fixed transition on pressure distributions in figure 27. To make small differences in C_p visible, the C_p scale in figure 27(a) has a grid line increment of -0.2 , unlike that in figure 26(a).

Fixed transition generally caused decreased c_n , less negative c_m , and increased c_d in the linear c_n - α range (fig. 25). The effects of fixed transition are largest at the lowest Reynolds number (4.5×10^6) and highest Mach number (0.735). The slightly decreased c_n with fixed transition for the 0.655 - 4.5×10^6 combination in figure 25(a) results from slight decreases in loading over most of the airfoil surface that outweigh localized increases in loading (fig. 27(a)). The very slight decrease in c_n with fixed transition for the 0.735 - 9.0×10^6 combination in figure 25(e) results primarily from decreased loading on the upper surface from $x/c = 0.2$ to 0.5 (fig. 27(b)). The slightly less negative c_m with fixed transition for the 0.655 - 4.5×10^6 combination in figure 25(a) results primarily from the slight decrease in aft loading in figure 27(a). The slightly less negative c_m with fixed transition for the 0.735 - 9.0×10^6 combination in figure 25(e) results

from both a slight increase in front loading and a slight decrease in loading aft of $x/c = 0.25$ in figure 27(b). These changes in load distribution result from shorter runs of laminar flow on the upper and/or lower surfaces with fixed transition. The increase in drag coefficient for both M_∞ - R_c combinations (see figs. 25(b) and 25(f)) is a result of the higher drag of the turbulent boundary layer and is more significant for the 0.655 - 4.5×10^6 combination.

Concluding Remarks

A wind tunnel test of a baseline executive-jet airfoil model was conducted in the two-dimensional adaptive-wall test section of the Langley 0.3-Meter Transonic Cryogenic Tunnel to measure aerodynamic characteristics for a wide range of flow conditions. Top and bottom wall interference was minimized by the appropriate movement of the flexible (adaptive) walls, and the data were corrected for residual wall effects. For increasing Mach number, the

maximum normal-force coefficient decreased. With increasing Mach number at a constant normal-force coefficient in the linear range of normal-force coefficient (c_n) versus angle of attack (α), increases occurred in the c_n - α slope, the negative pitching-moment coefficient, and the drag coefficient. With increasing Reynolds number at a constant normal-force coefficient, the negative pitching-moment coefficient became more negative and the drag coefficient decreased. The pressure distributions revealed that separation began at the trailing edge. Fixed transition generally resulted in higher drag coefficients (particularly for the lowest Reynolds number), slightly lower normal-force coefficients, and slightly less negative pitching-moment coefficients.

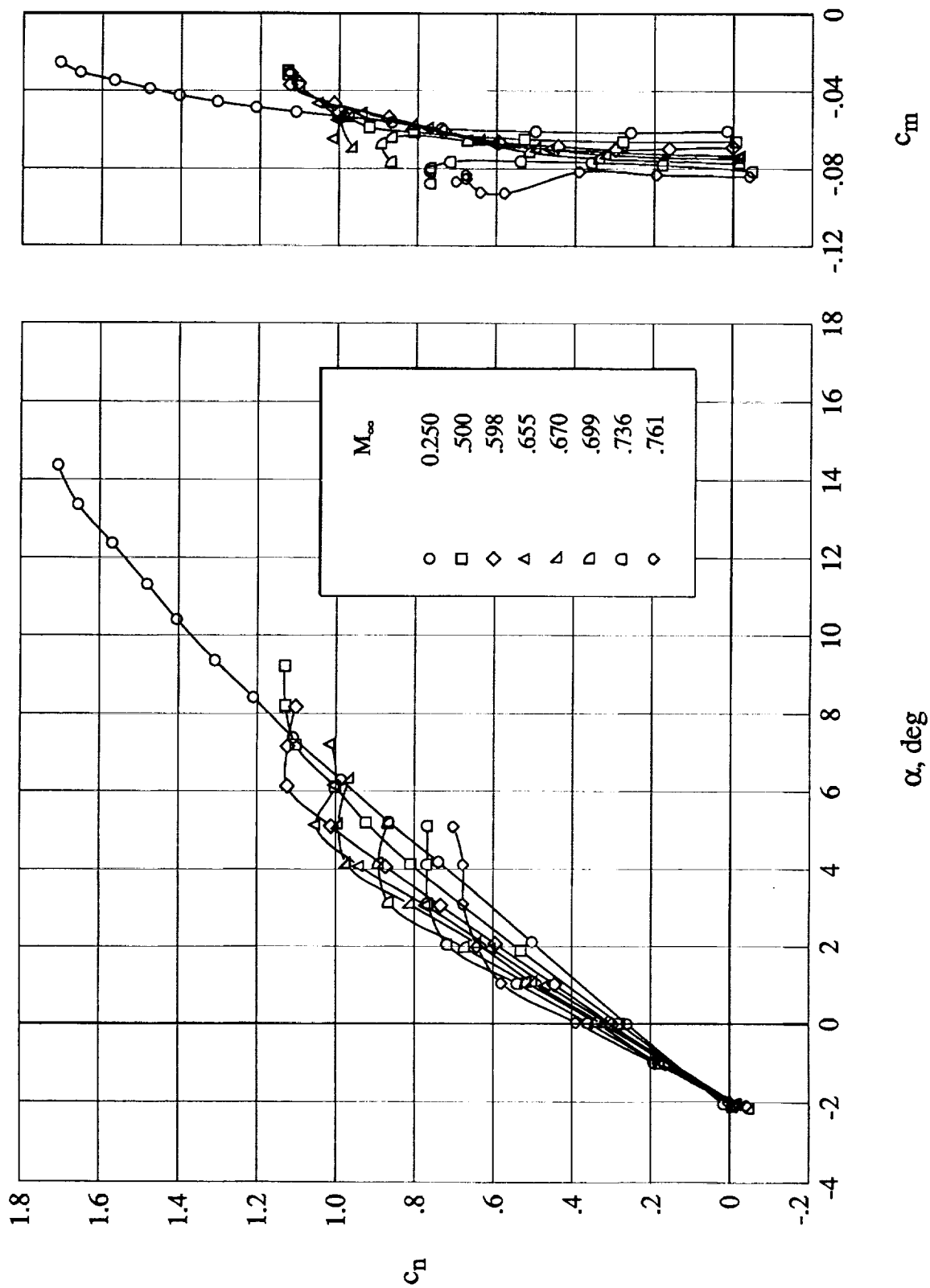
NASA Langley Research Center
Hampton, VA 23681-0001
September 29, 1993

Appendix

Data for $c_n > 1.2$

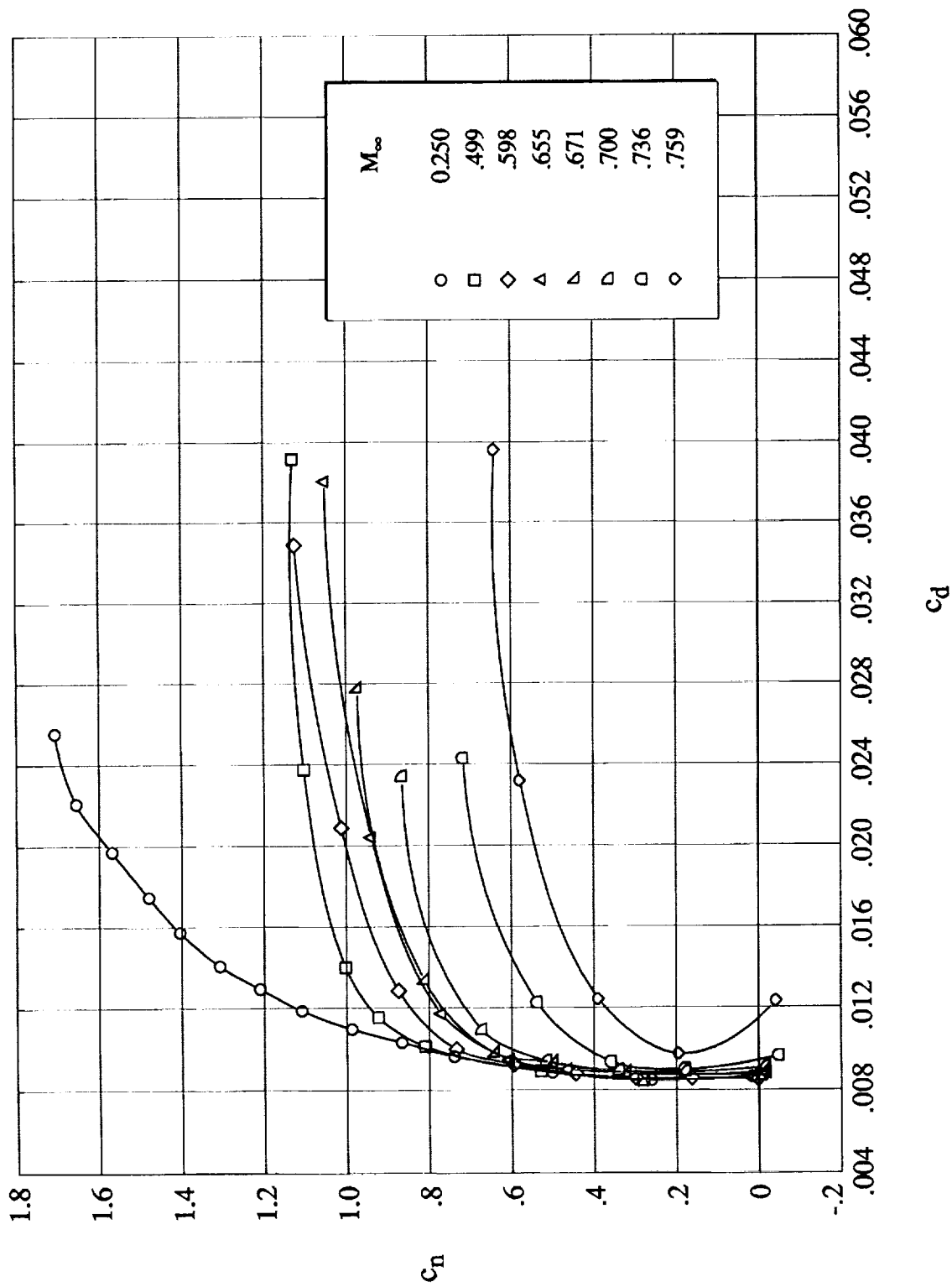
This appendix presents data at high normal-force coefficients (for angles of attack up to 14°) that were made possible by the adaptive tunnel walls at $M_\infty \approx 0.250$ and $R_c = 4.5 \times 10^6$. All normal-force coefficients are less than 1.2 at all other conditions.

The data in this appendix were taken with fixed transition. The force and moment data from figures 13(c) and 13(d) along with the data for $c_n > 1.2$ are presented in figure A1. Pressure distributions for $\alpha = 0^\circ$ and 7.4° from figure 16(a) along with other data selected from points in figure A1 are presented in figure A2. The c_n and C_p scales in figures A1 and A2 are different from those in figures 13 and 16, respectively, to accommodate the additional data.



(a) Normal-force and pitching-moment coefficients.

Figure A1. Effect of free-stream Mach number at $R_c = 4.5 \times 10^6$.



(b) Drag coefficient.

Figure A1. Concluded.

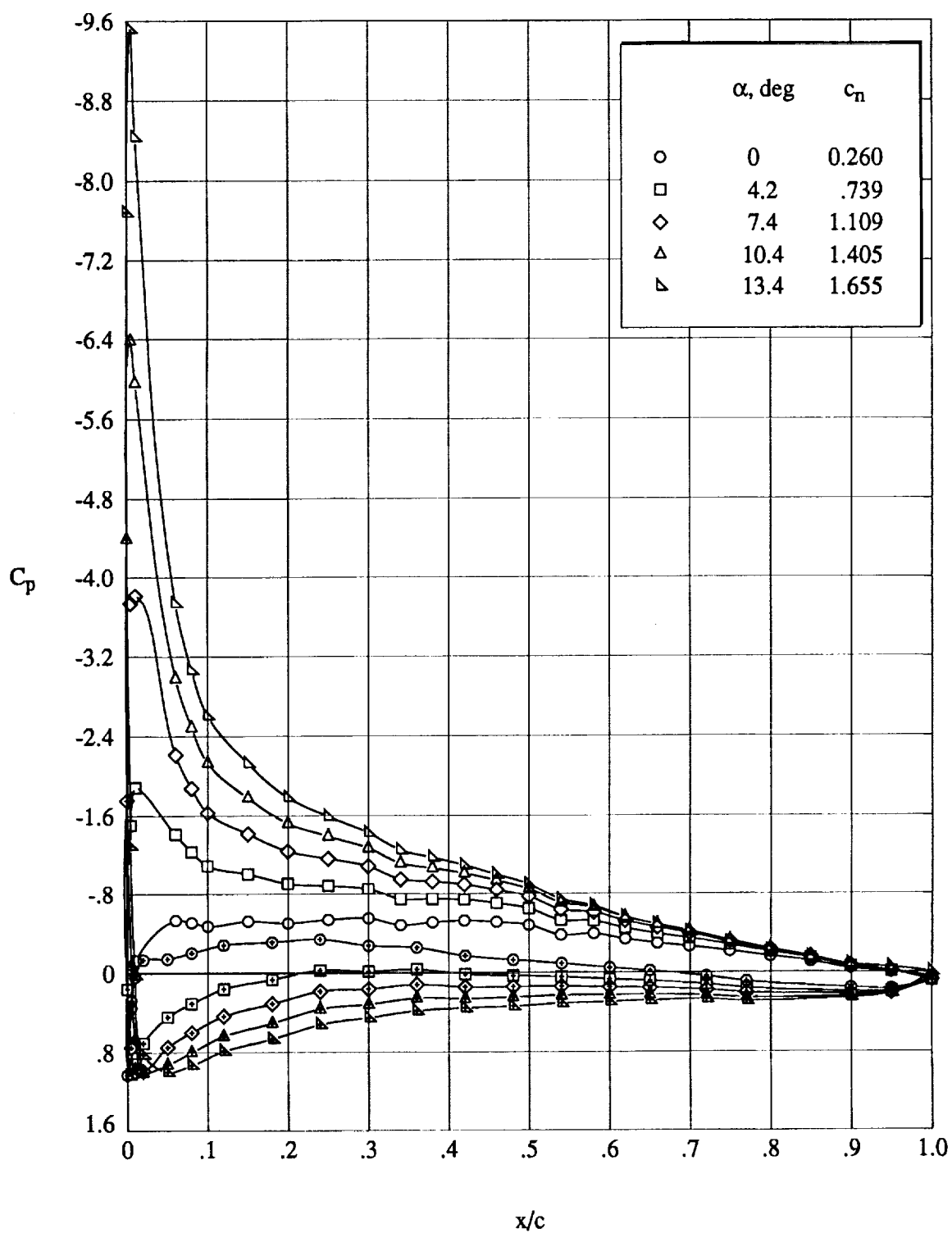


Figure A2. Effect of angle of attack at $M_\infty \approx 0.250$ and $R_c = 4.5 \times 10^6$. Open symbols denote upper surface; “+” within symbol denotes lower surface.

References

1. Campbell, Richard L.: *An Approach to Constrained Aerodynamic Design With Application to Airfoils*. NASA TP-3260, 1992.
2. Ray, Edward J.; Ladson, Charles L.; Adcock, Jerry B.; Lawing, Pierce L.; and Hall, Robert M.: *Review of Design and Operational Characteristics of the 0.3-Meter Transonic Cryogenic Tunnel*. NASA TM-80123, 1979.
3. Judd, M.; Wolf, S. W. D.; and Goodyer, M. J.: *Analytical Work in Support of the Design and Operation of Two Dimensional Self-Streamlining Test Sections*. NASA CR-145019, 1976.
4. Ladson, Charles L.; and Kilgore, Robert A.: *Instrumentation for Calibration and Control of a Continuous-Flow Cryogenic Tunnel*. NASA TM-81825, 1980.
5. Braslow, Albert L.; and Knox, Eugene C.: *Simplified Method for Determination of Critical Height of Distributed Roughness Particles for Boundary-Layer Transition at Mach Numbers From 0 to 5*. NACA TN-4363, 1958.
6. Hall, Robert M.; and Adcock, Jerry B.: *Simulation of Ideal-Gas Flow by Nitrogen and Other Selected Gases at Cryogenic Temperatures*. NASA TP-1901, 1981.
7. Adcock, Jerry B.: *Real-Gas Effects Associated With One-Dimensional Transonic Flow of Cryogenic Nitrogen*. NASA TN D-8274, 1976.
8. Adcock, Jerry B.; and Johnson, Charles B.: *A Theoretical Analysis of Simulated Transonic Boundary Layers in Cryogenic-Nitrogen Wind Tunnels*. NASA TP-1631, 1980.
9. Murthy, A. V.: *Residual Interference Assessment in Adaptive Wall Wind Tunnels*. NASA CR-181896, 1989.
10. Akima, Hiroshi: A New Method of Interpolation and Smooth Curve Fitting Based on Local Procedures. *J. Assoc. Comput. Mach.*, vol. 17, no. 4, Oct. 1970, pp. 589-602.
11. Bauer, Frances; Garabedian, Paul; Korn, David; and Jameson, Antony: Supercritical Wing Sections II. Volume 108 of *Lecture Notes in Economics and Mathematical Systems*, M. Beckmann and H. P. Kuenzi, eds., Springer-Verlag, 1975.
12. Baals, Donald D.; and Mourhess, Mary J.: *Numerical Evaluation of the Wake-Survey Equations for Subsonic Flow Including the Effect of Energy Addition*. NACA WR L-5, 1945. (Formerly NACA ARR L5H27.)

Table 1. Locations of Jacks for Flexible-Wall Positioning
[Jack station locations are referenced to center of turntable]

Jack	Location, in.	Notes
	-31.25	Pressure orifice near test section entrance
	-30.25	Anchor point
1	-26.00	First test section jack
2	-20.25	
3	-15.25	
4	-11.25	
5	-8.25	
6	-6.25	
7	-4.75	
8	-3.25	
9	-1.75	Lower wall jack at this station not operational
10	-.25	
11	1.25	
12	2.75	
13	4.75	
14	6.75	
15	8.75	
16	11.75	
17	15.75	
18	20.75	Last test section jack
19	25.75	Start of transition section
20	30.75	
21	36.75	

Table 2. Design Airfoil Coordinates

Upper surface		Lower surface	
x/c	y/c	x/c	y/c
0.00000	0.00000	0.00000	0.00000
.00099	.00635	.00099	-.00489
.00301	.01117	.00301	-.00821
.00604	.01562	.00604	-.01132
.01005	.01974	.01005	-.01431
.01500	.02362	.01500	-.01702
.02088	.02731	.02088	-.01949
.02764	.03076	.02764	-.02183
.03528	.03395	.03528	-.02407
.04374	.03692	.04374	-.02622
.05302	.03969	.05302	-.02830
.06308	.04230	.06308	-.03035
.07389	.04477	.07389	-.03234
.08543	.04713	.08543	-.03428
.09766	.04937	.09766	-.03617
.11056	.05152	.11056	-.03797
.12411	.05358	.12411	-.03968
.13826	.05554	.13826	-.04126
.15300	.05740	.15300	-.04270
.16830	.05915	.16830	-.04400
.18413	.06078	.18413	-.04512
.20045	.06228	.20045	-.04605
.21725	.06364	.21725	-.04680
.23450	.06484	.23450	-.04735
.25216	.06587	.25216	-.04769
.27021	.06674	.27021	-.04783
.28863	.06743	.28863	-.04777
.30737	.06796	.30737	-.04751
.32642	.06831	.32642	-.04705
.34575	.06851	.34575	-.04642
.36533	.06854	.36533	-.04561
.38513	.06840	.38513	-.04465
.40512	.06809	.40512	-.04355
.42527	.06760	.42527	-.04233

Upper surface		Lower surface	
x/c	y/c	x/c	y/c
0.44557	0.06691	0.44557	-0.04100
.46597	.06601	.46597	-.03958
.48646	.06488	.48646	-.03808
.50699	.06353	.50699	-.03651
.52756	.06197	.52756	-.03487
.54812	.06020	.54812	-.03317
.56865	.05826	.56865	-.03141
.58912	.05617	.58912	-.02961
.60950	.05397	.60950	-.02777
.62977	.05168	.62977	-.02591
.64990	.04933	.64990	-.02403
.66986	.04692	.66986	-.02214
.68962	.04448	.68962	-.02027
.70915	.04200	.70915	-.01842
.72843	.03948	.72843	-.01662
.74742	.03694	.74742	-.01489
.76611	.03438	.76611	-.01324
.78445	.03181	.78445	-.01170
.80243	.02922	.80243	-.01028
.82002	.02665	.82002	-.00897
.83718	.02409	.83718	-.00781
.85389	.02157	.85389	-.00678
.87013	.01910	.87013	-.00591
.88585	.01670	.88585	-.00520
.90105	.01438	.90105	-.00463
.91568	.01217	.91568	-.00423
.92972	.01006	.92972	-.00397
.94314	.00807	.94314	-.00385
.95592	.00621	.95592	-.00386
.96802	.00447	.96802	-.00398
.97942	.00285	.97942	-.00421
.99009	.00136	.99009	-.00453
1.00000	.00000	1.00000	-.00490

Table 3. Measured Airfoil Coordinates

Upper surface		Lower surface	
x/c	y/c	x/c	y/c
0.00000	-0.00018	0.00000	-0.00018
.00013	.00173	.00006	-.00117
.00036	.00324	.00026	-.00235
.00072	.00470	.00059	-.00357
.00121	.00637	.00100	-.00469
.00180	.00795	.00161	-.00592
.00248	.00949	.00226	-.00703
.00332	.01115	.00301	-.00811
.00432	.01283	.00400	-.00929
.00535	.01433	.00504	-.01042
.00661	.01596	.00629	-.01158
.00800	.01753	.00773	-.01276
.00957	.01910	.00929	-.01387
.01134	.02068	.01115	-.01506
.01331	.02225	.01310	-.01616
.01552	.02383	.01525	-.01722
.01793	.02541	.01770	-.01831
.02051	.02694	.02029	-.01936
.02340	.02853	.02322	-.02046
.02646	.03005	.02645	-.02156
.03001	.03168	.02984	-.02263
.03387	.03328	.03363	-.02374
.03785	.03478	.03768	-.02485
.04249	.03639	.04236	-.02605
.04737	.03794	.04724	-.02722
.05266	.03948	.05263	-.02844
.05861	.04108	.05847	-.02968
.06499	.04266	.06482	-.03095
.07202	.04429	.07190	-.03227
.07959	.04588	.07948	-.03359
.08799	.04755	.08788	-.03497
.09712	.04923	.09707	-.03637
.10712	.05094	.10710	-.03779
.11805	.05267	.11797	-.03920
.13004	.05441	.12980	-.04060
.14303	.05616	.14297	-.04201
.15718	.05790	.15721	-.04334
.17255	.05962	.17259	-.04458
.18943	.06129	.18941	-.04569
.20758	.06287	.20758	-.04662
.22739	.06437	.22726	-.04736
.24866	.06571	.24853	-.04783

Upper surface		Lower surface	
x/c	y/c	x/c	y/c
0.27144	0.06684	0.27151	-0.04802
.29567	.06771	.29598	-.04787
.32149	.06831	.32179	-.04736
.34888	.06859	.34911	-.04647
.37755	.06853	.37763	-.04521
.40717	.06810	.40723	-.04360
.43757	.06729	.43767	-.04170
.46866	.06596	.46875	-.03953
.50004	.06411	.50001	-.03718
.53135	.06174	.53139	-.03467
.56238	.05895	.56255	-.03204
.59290	.05586	.59296	-.02933
.62243	.05264	.62258	-.02658
.65093	.04935	.65111	-.02399
.67834	.04604	.67821	-.02156
.70403	.04281	.70422	-.01914
.72850	.03962	.72834	-.01680
.75113	.03661	.75125	-.01463
.77245	.03370	.77260	-.01272
.79225	.03092	.79211	-.01111
.81047	.02829	.81036	-.00969
.82727	.02577	.82722	-.00849
.84258	.02343	.84278	-.00747
.85698	.02121	.85686	-.00663
.86995	.01919	.86994	-.00595
.88194	.01732	.88184	-.00539
.89269	.01566	.89284	-.00495
.90269	.01412	.90286	-.00461
.91195	.01270	.91192	-.00437
.92033	.01144	.92029	-.00418
.93496	.00929	.93496	-.00397
.94729	.00753	.94717	-.00391
.95755	.00609	.95736	-.00397
.96608	.00492	.96596	-.00407
.97349	.00389	.97317	-.00419
.97944	.00307	.97932	-.00433
.98446	.00235	.98439	-.00446
.98879	.00174	.98847	-.00457
.99218	.00123	.99182	-.00468
.99592	.00062	.99573	-.00480
1.00000	-.00017	1.00000	-.00473

Table 4. Orifice Locations

Upper surface		Lower surface	
x/c	y/c	x/c	y/c
0.00000	0.00000	0.00484	-0.01033
.00482	.01350	.00973	-.01427
.01072	.02006	.01983	-.01928
.06040	.04145	.04998	-.02794
.08032	.04595	.08002	-.03376
.10018	.04968	.11985	-.03951
.15031	.05700	.18013	-.04518
.19999	.06217	.23973	-.04774
.25008	.06574	.30012	-.04786
.30009	.06779	.36012	-.04606
.34008	.06850	.42040	-.04284
.37985	.06847	.48012	-.03870
.41952	.06779	.54025	-.03394
.45951	.06638	.60018	-.02866
.49968	.06412	.65006	-.02407
.53960	.06103	.72036	-.01754
.58038	.05716	.77005	-.01291
.61948	.05297	.89966	-.00465
.65947	.04834	.94999	-.00385
.69920	.04344	1.00000	-.00245
.74927	.03689		
.79948	.02992		
.84950	.02241		
.89919	.01471		
.94951	.00728		
1.00000	-.00245		

Table 5. Program of Test Conditions

[Dashed underlines indicate M_∞ - R_c combinations for two design points]

R_c	Figures for pressure distributions at values of M_∞ of—								
	0.250	0.500	0.600	0.655	0.670	0.700	0.735	0.760	0.780
18.0×10^6						21(f)			
13.5						21(e)	22(d)		
9.0	16(b)	17(b)	18(b)	19(d)		21(d)	<u>22(c)</u>	23(c)	24
6.5				19(c)		21(c)	22(b)	23(b)	
5.0					20(b)				
4.5	16(a)	17(a)	18(a)	<u>19(b)</u>	20(a)	21(b)	22(a)	23(a)	
3.0				19(a)		21(a)			

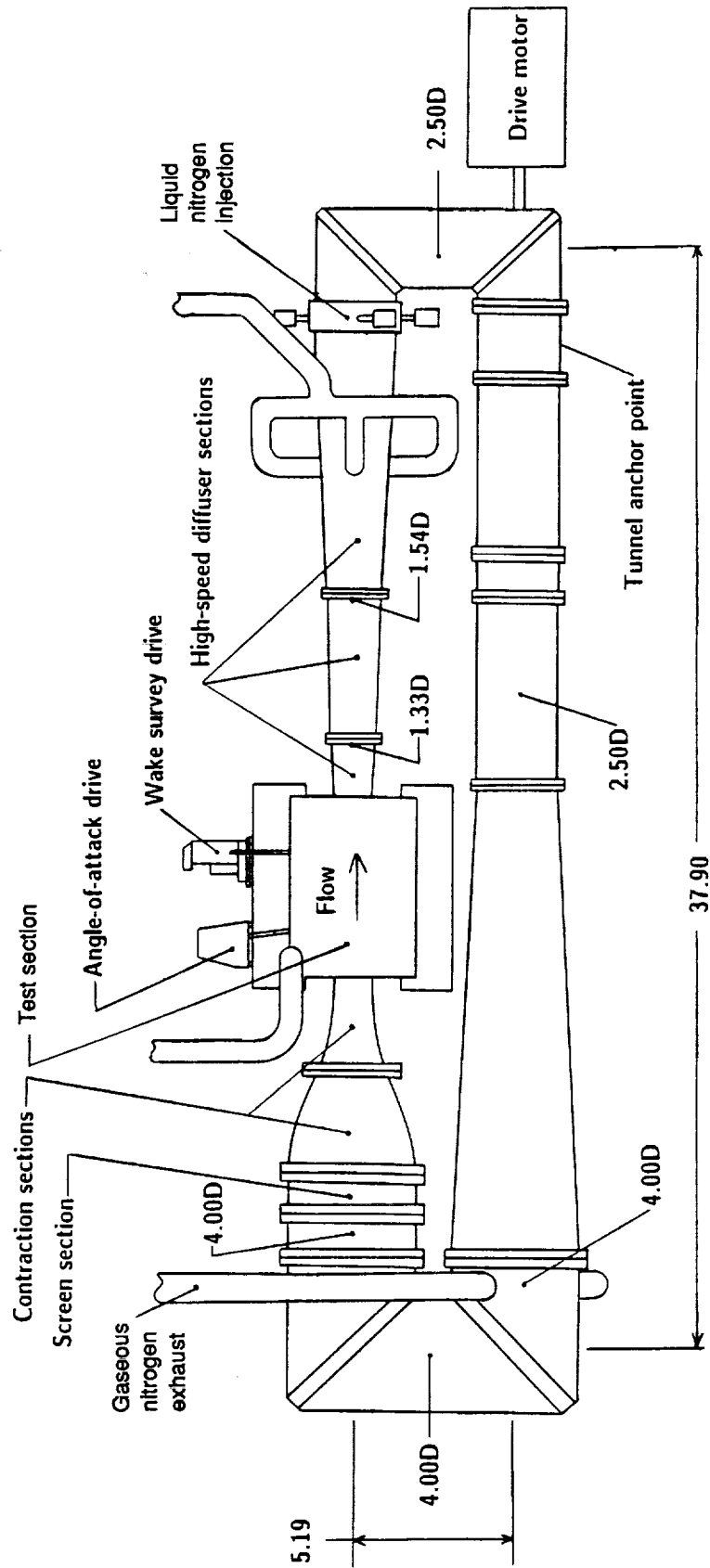
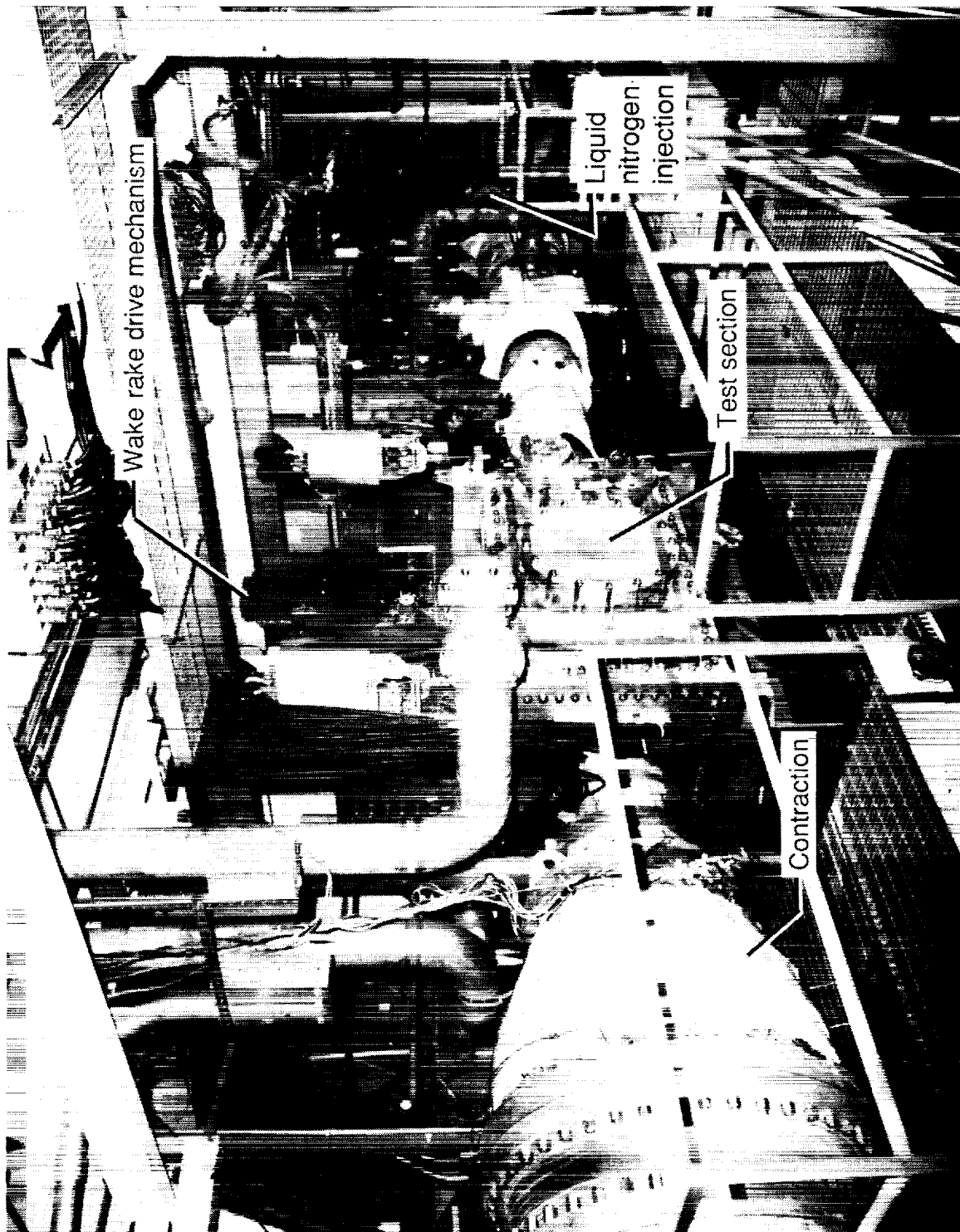
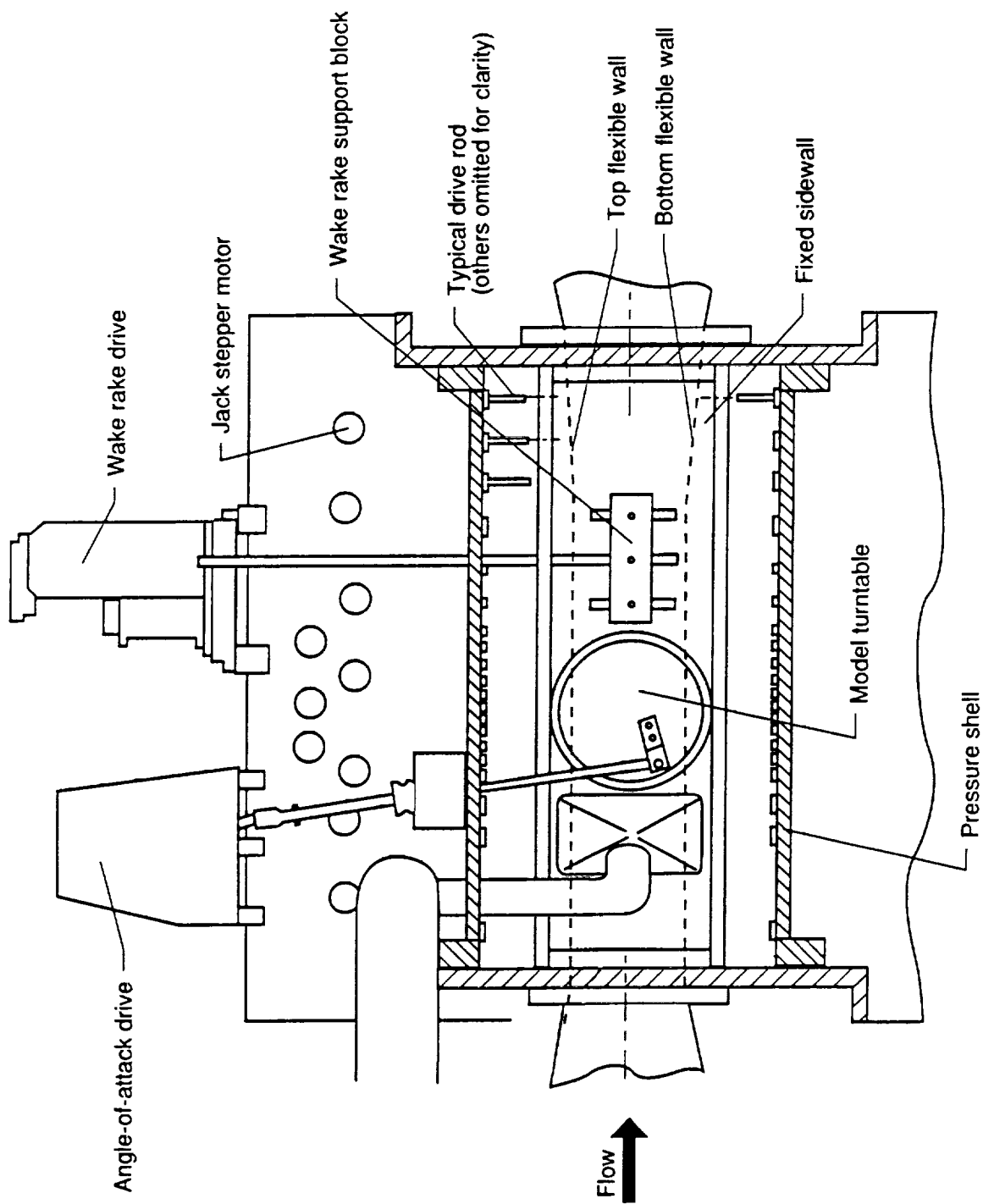


Figure 1. Sketch of the Langley 0.3-Meter Transonic Cryogenic Tunnel with 13- by 13-in. adaptive-wall test section. All dimensions are given in feet. Diameters are for tunnel interior.



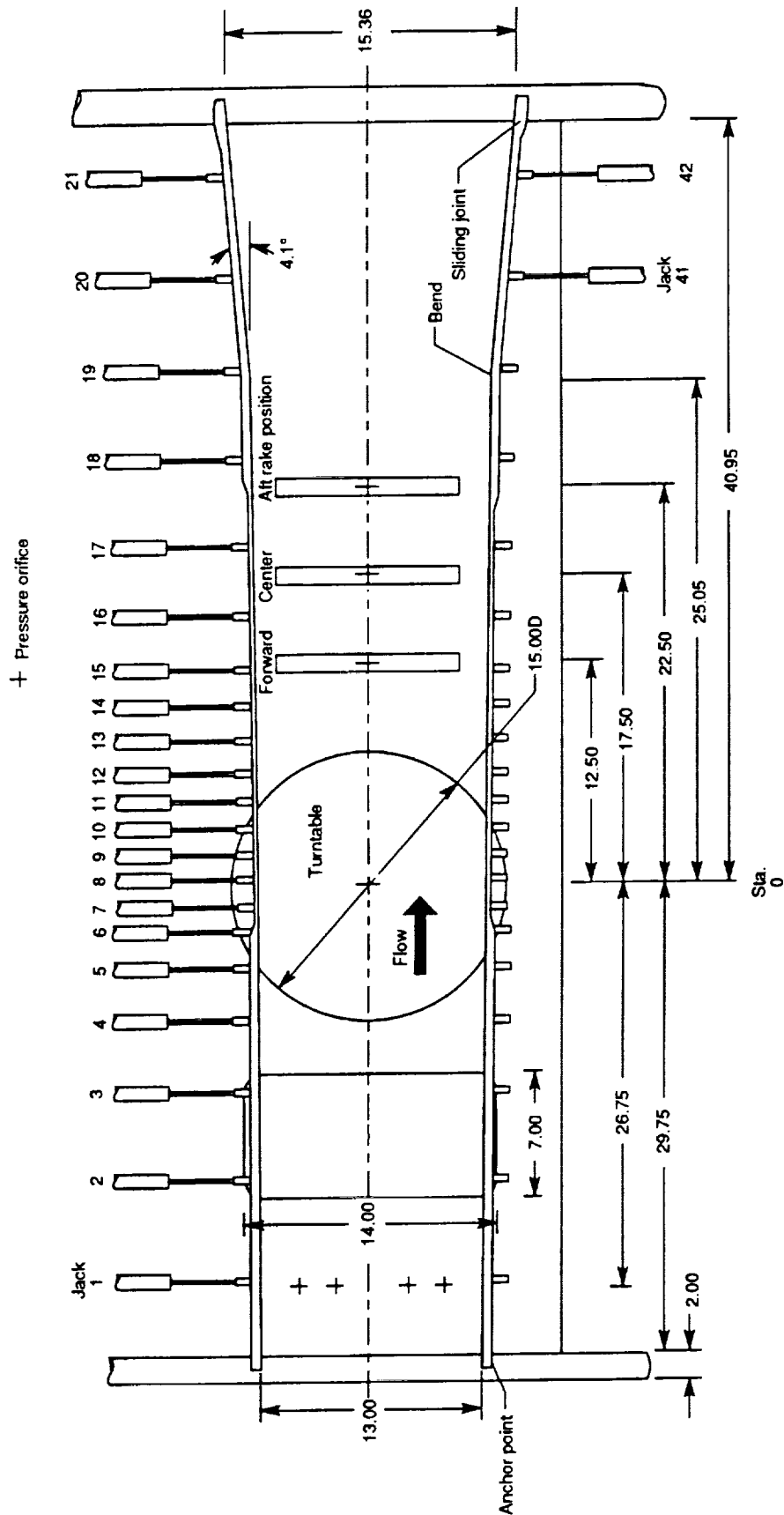
L-85-9893

Figure 2. Photograph of upper leg of the Langley 0.3-Meter Transonic Cryogenic Tunnel with 13- by 13-in. adaptive-wall test section.



(a) Plenum sidewall removed.

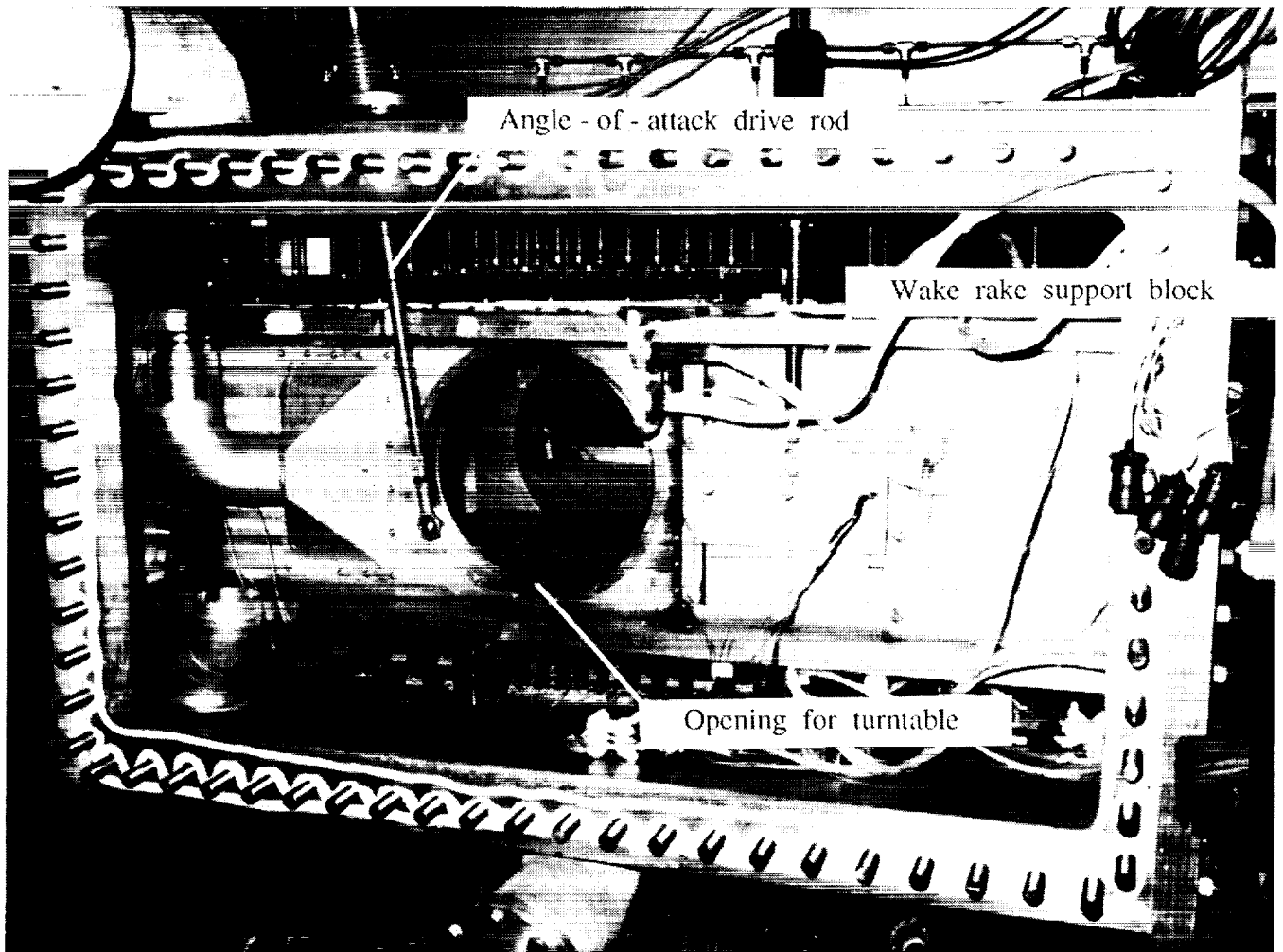
Figure 3. Sketches of 13- by 13-in. adaptive-wall test section.



(b) Details of flow region. Some lower wall jacks are omitted for clarity. All dimensions are given in inches.

Figure 3. Concluded.

ORIGINAL PAGE
BLACK AND WHITE PHOTOGRAPH



L-87-8385

Figure 4. Photograph of flow region of adaptive-wall test section with plenum sidewall removed.

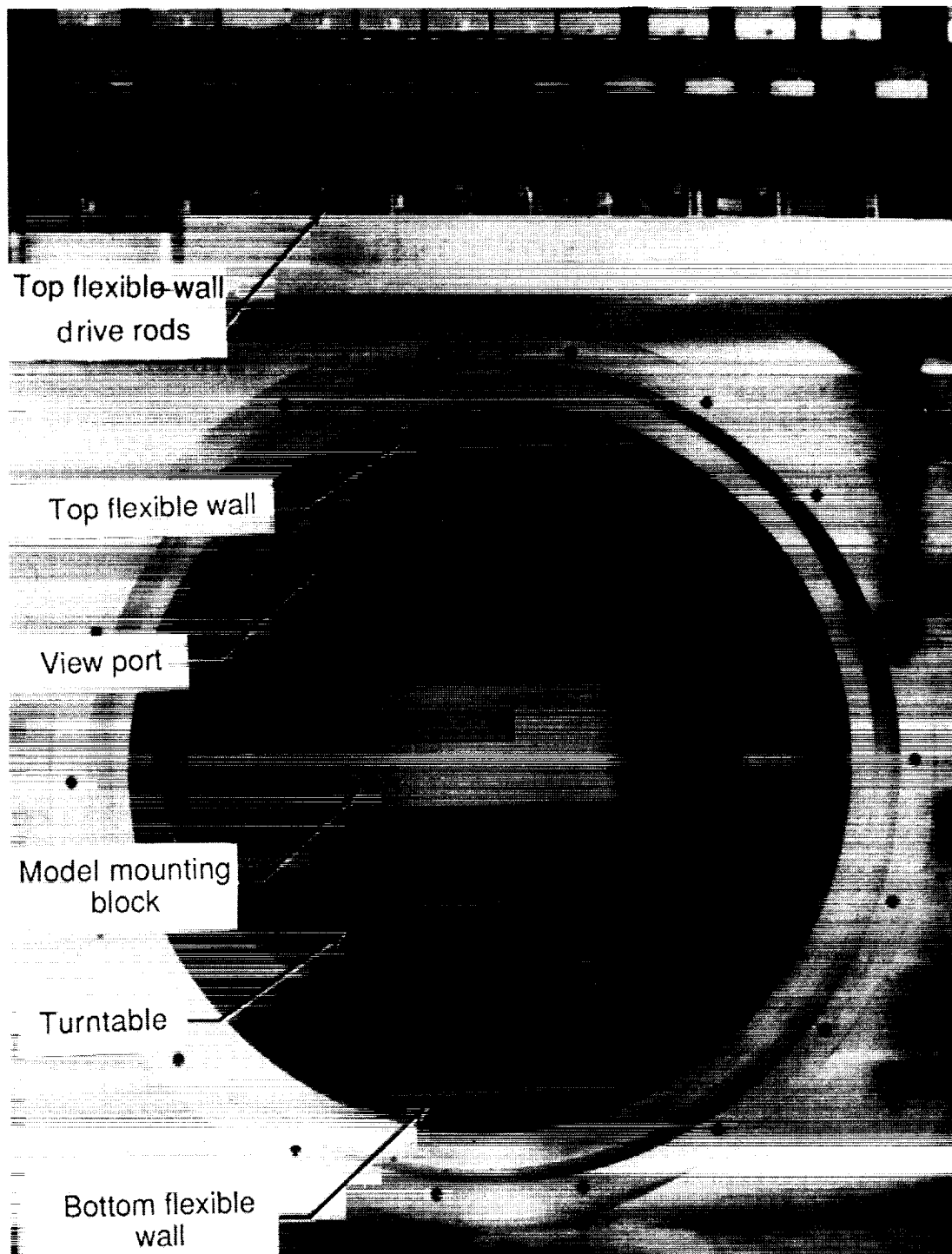


Figure 5. Photograph of region where model is installed.

L-87-659

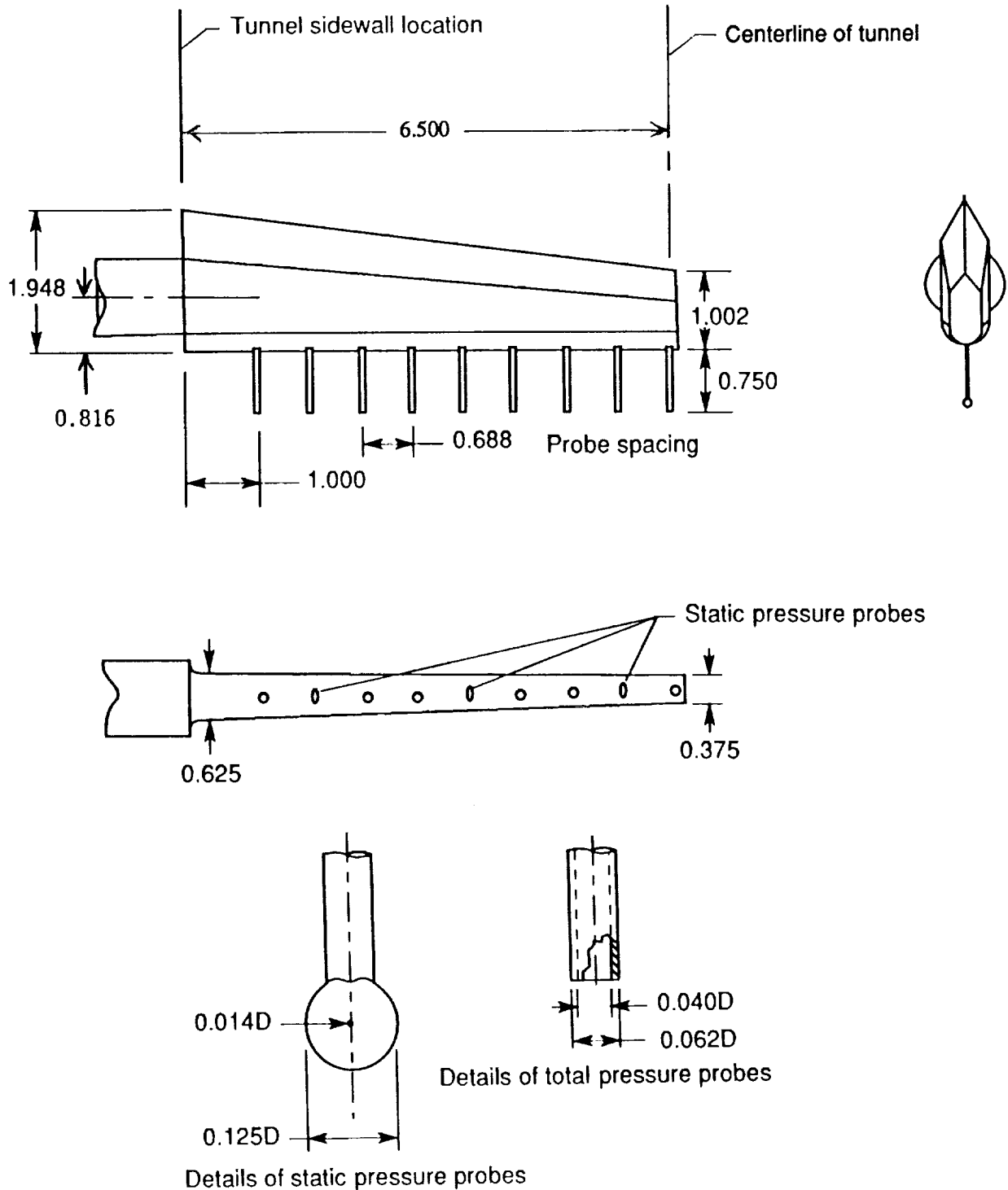
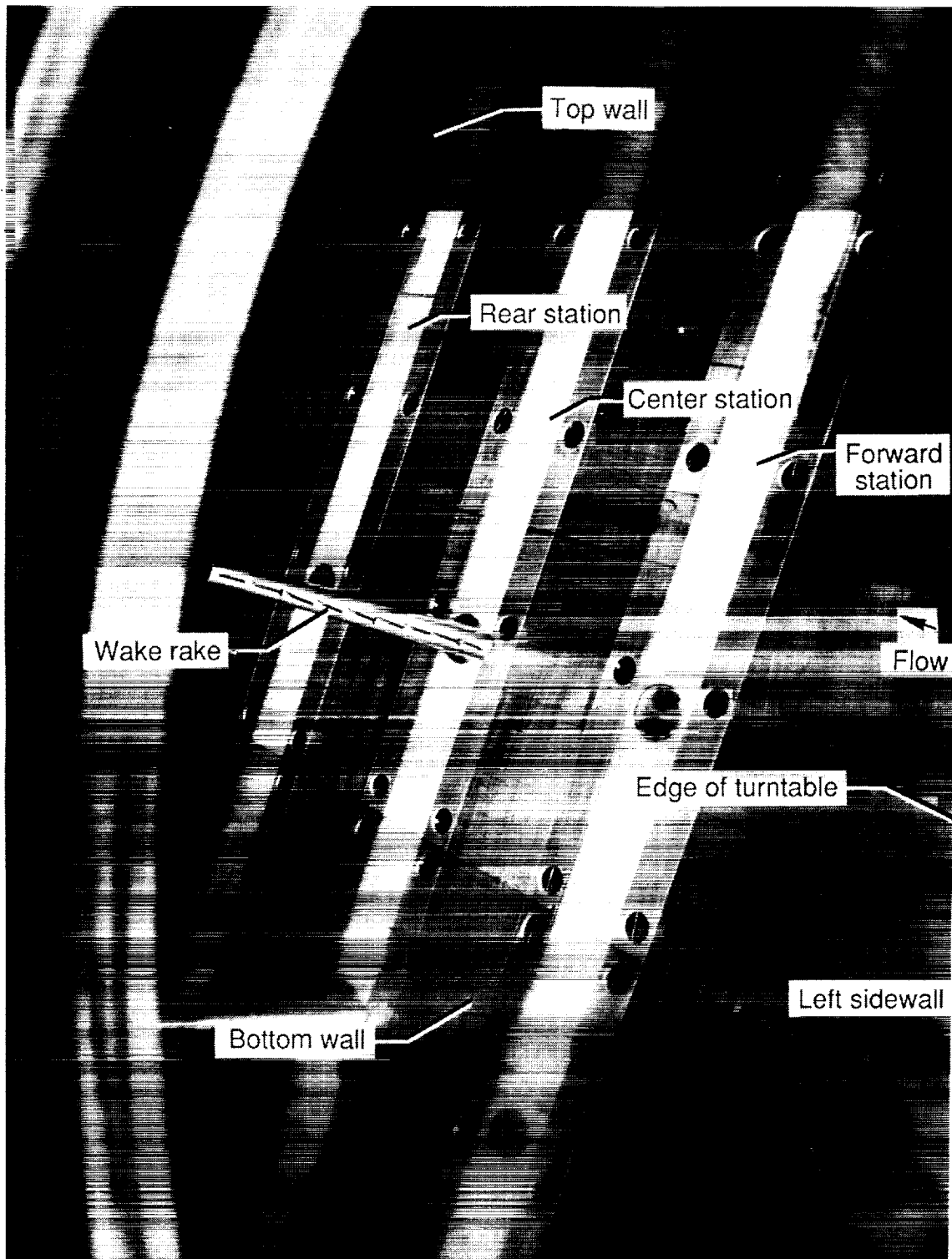


Figure 6. Sketches of wake survey probe. All dimensions are given in inches.

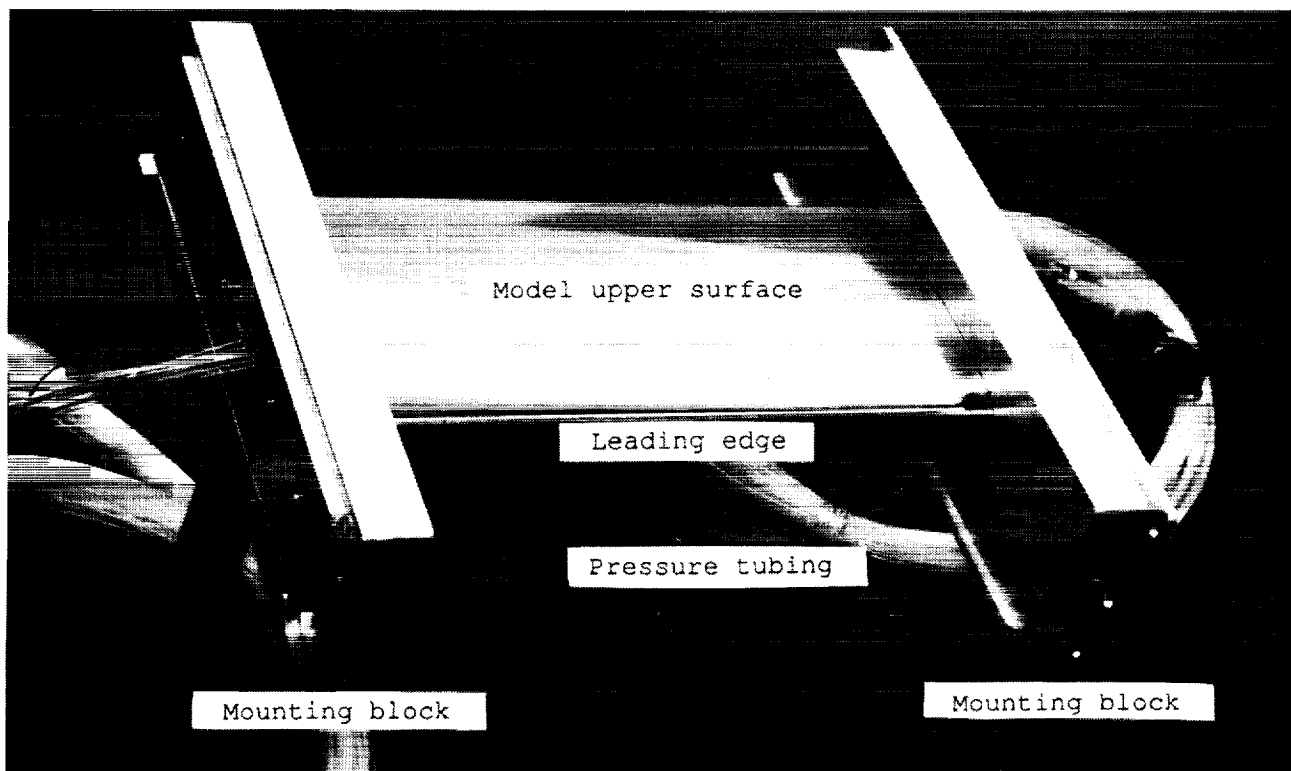
ORIGINAL PAGE
BLACK AND WHITE PHOTOGRAPH



L-89-49

Figure 7. Photograph of wake survey probe mounted in center survey station. Edge of turntable is just upstream of photograph.

ORIGINAL PAGE
BLACK AND WHITE PHOTOGRAPH



L-91-16195

Figure 8. Airfoil model in mounting blocks that fit into turntable.

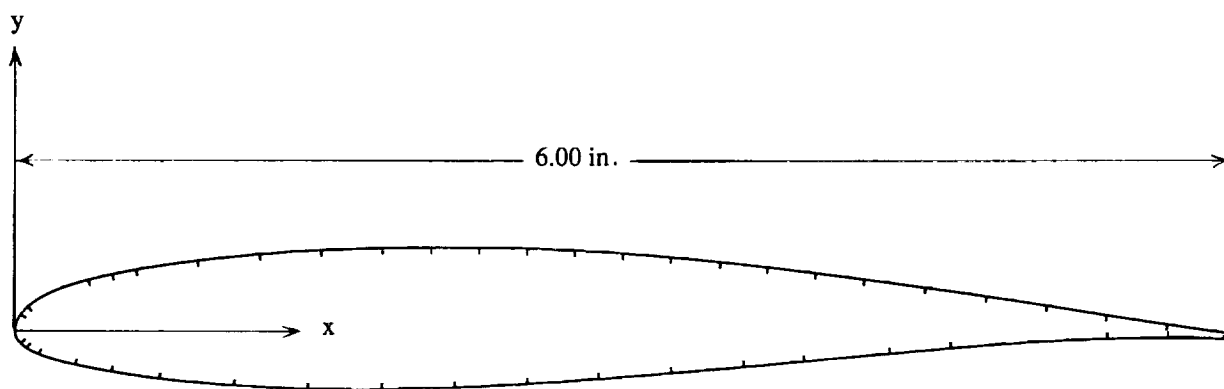


Figure 9. Airfoil section showing pressure orifice locations.

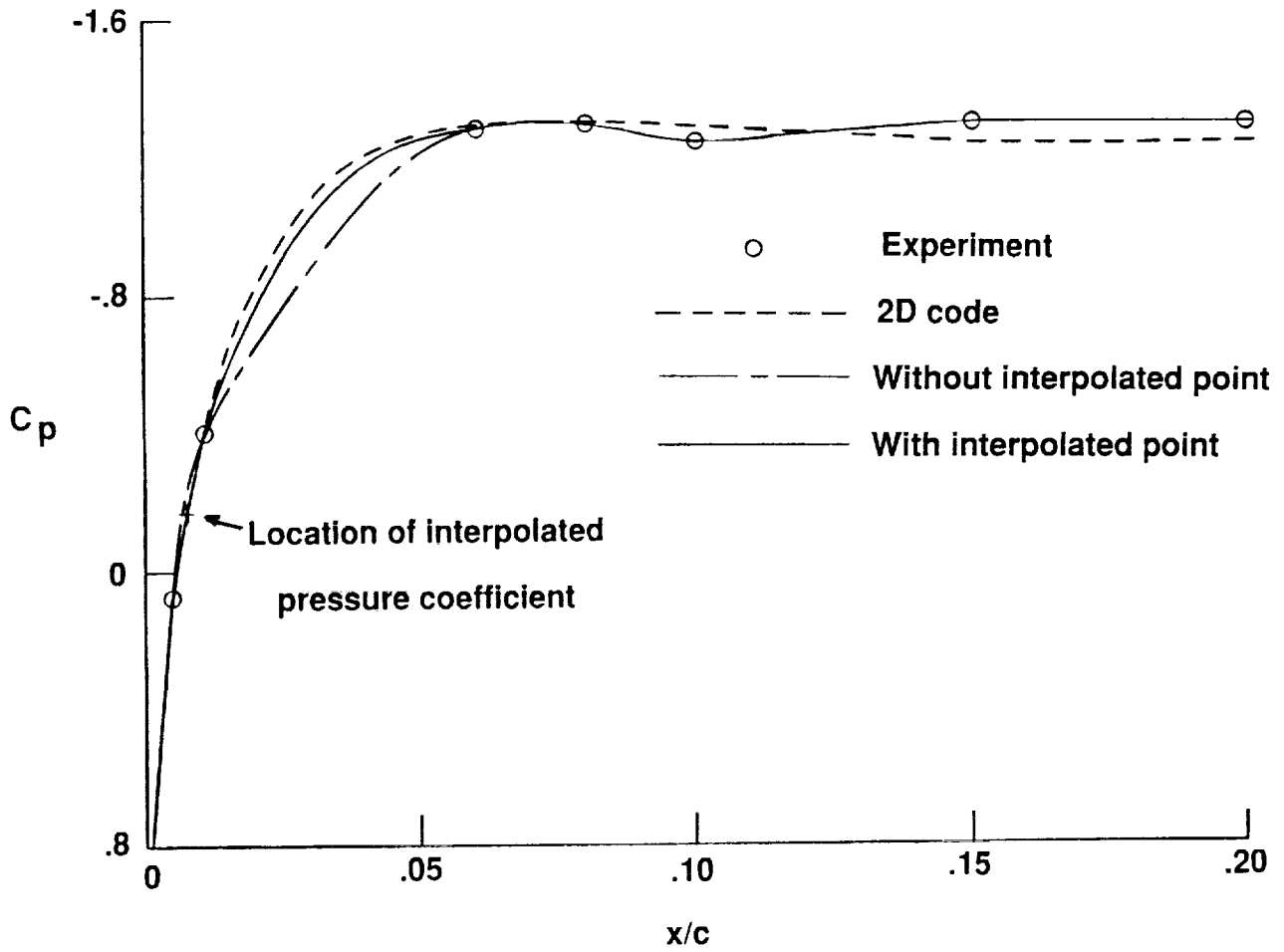
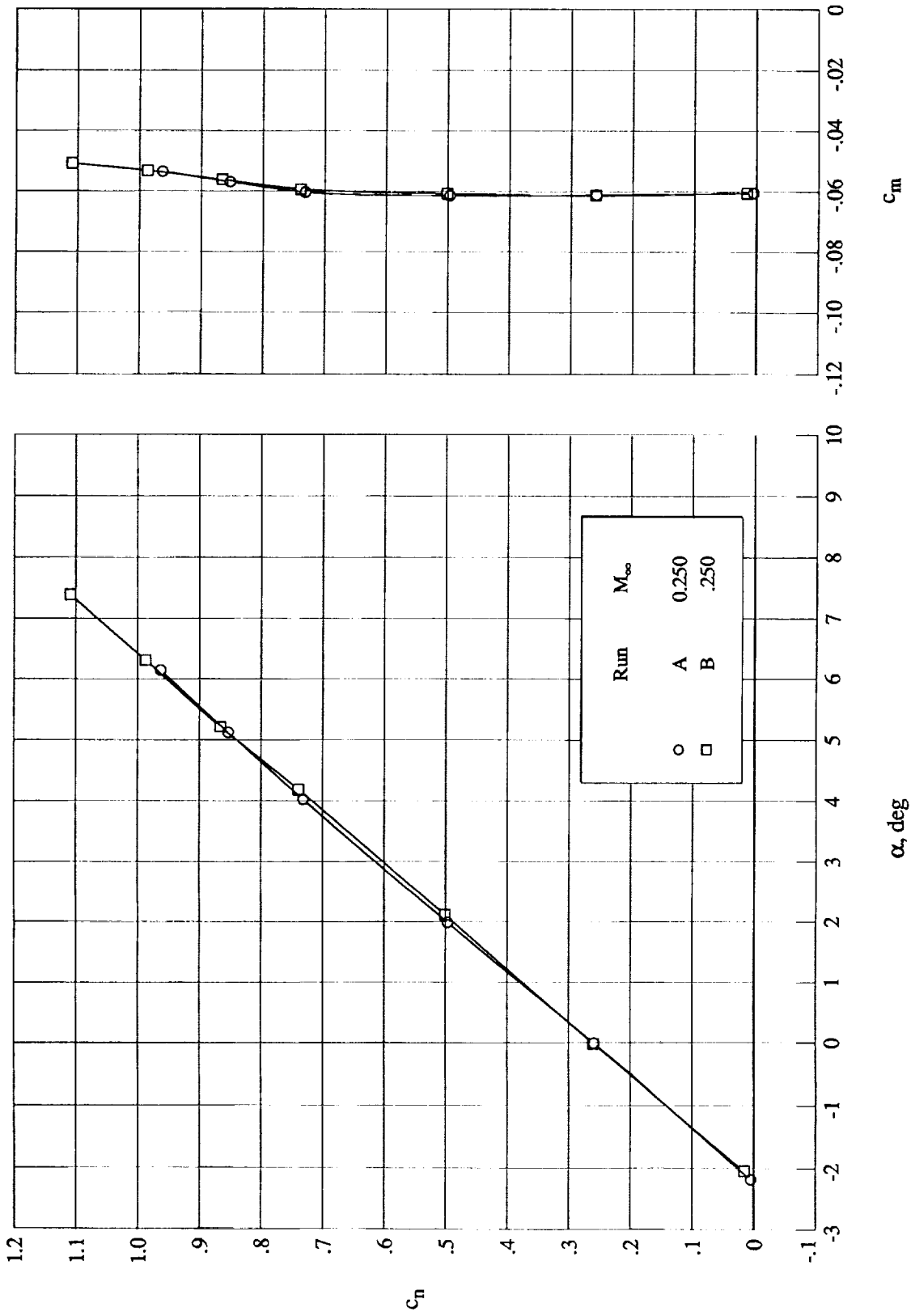
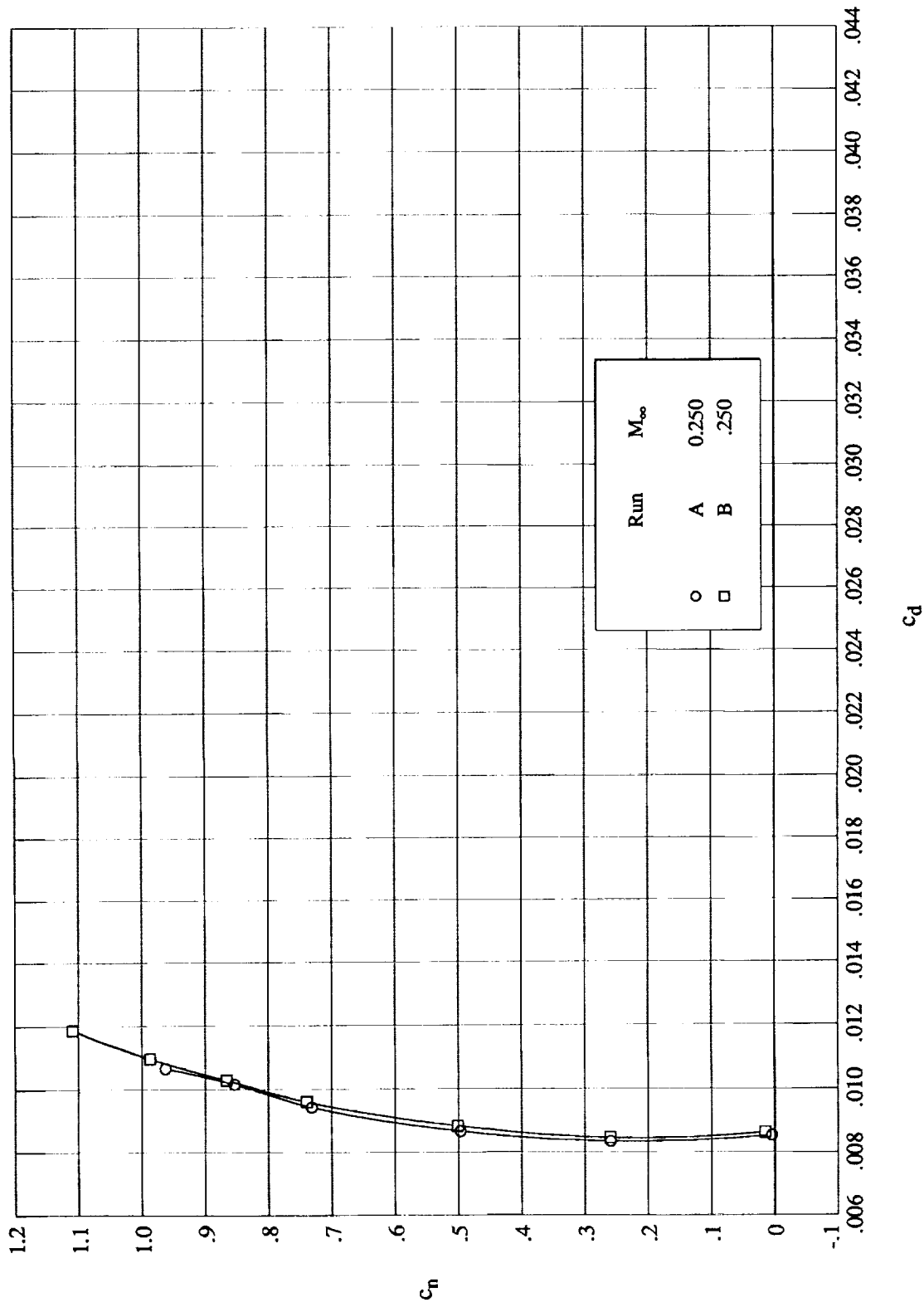


Figure 10. Effect of adding interpolated pressure coefficient point on curve fit. $M_\infty \approx 0.700$; $R_c = 6.5 \times 10^6$; $c_n = 0.69$.



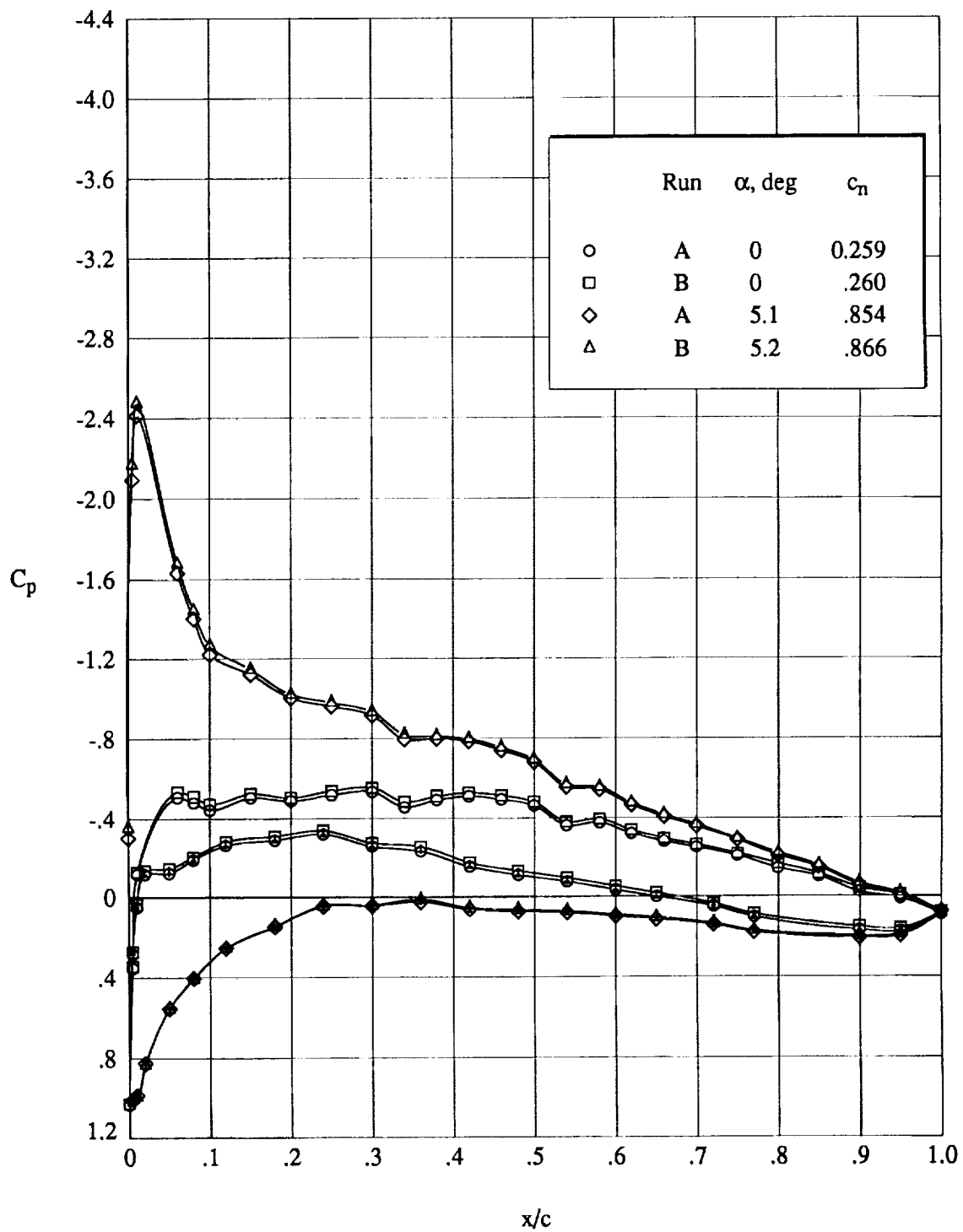
(a) Normal-force and pitching-moment coefficients.

Figure 11. Subsonic repeat runs. $M_\infty \approx 0.250$; $R_c = 4.5 \times 10^6$.



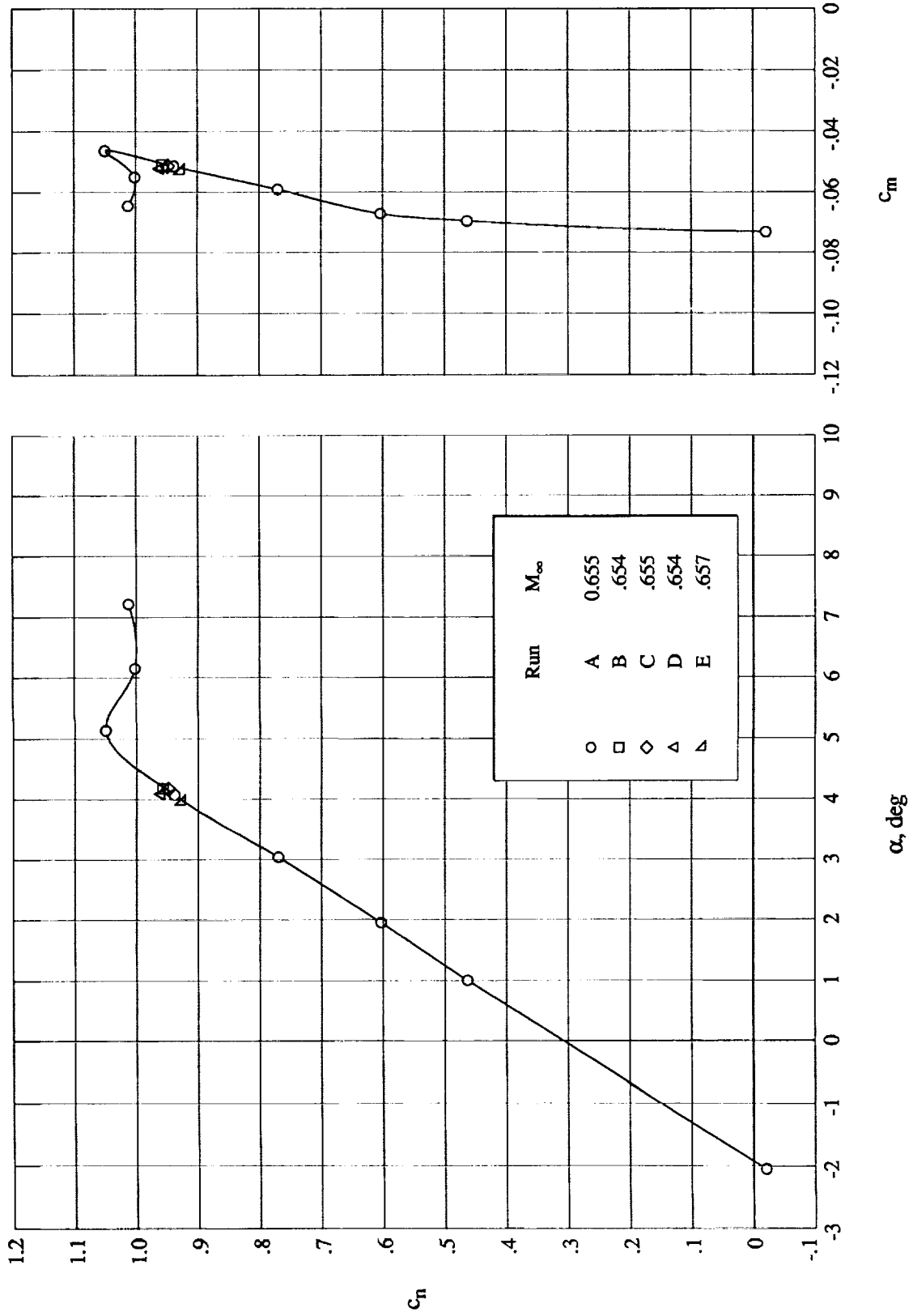
(b) Drag coefficient.

Figure 11. Continued.



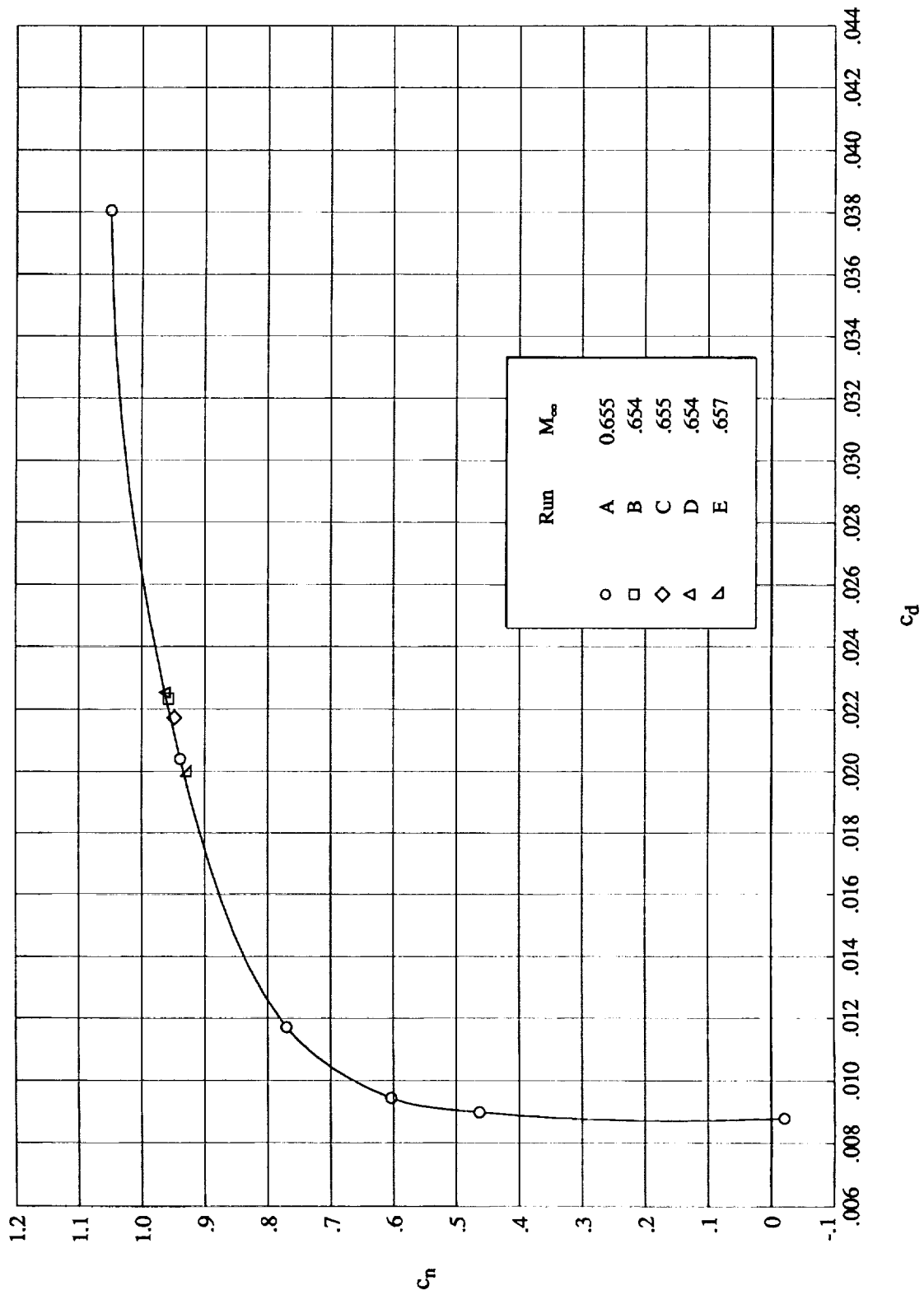
(c) Pressure distributions. Open symbols denote upper surface; "+" within symbol denotes lower surface.

Figure 11. Concluded.



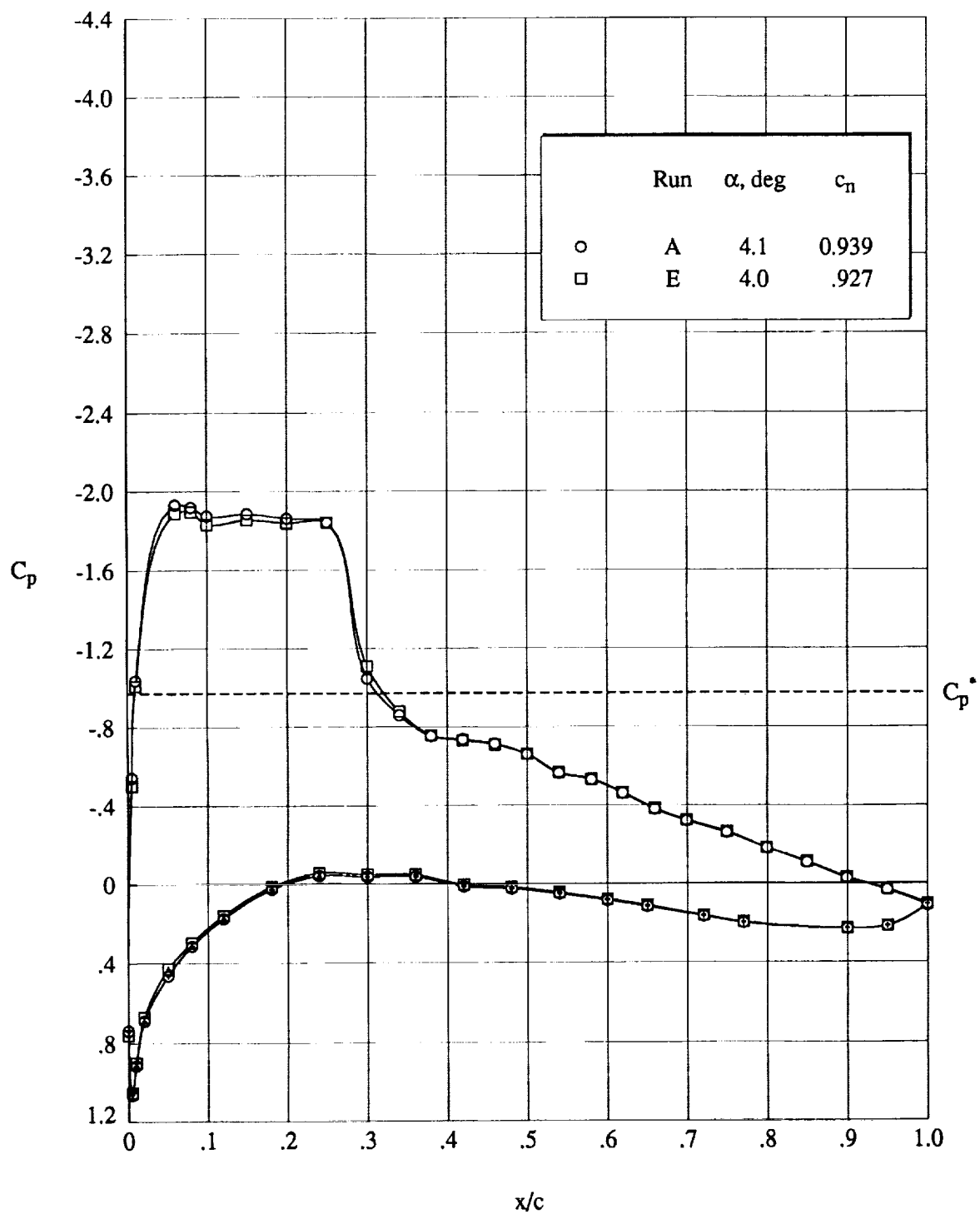
(a) Normal-force and pitching-moment coefficients.

Figure 12. Transonic repeat runs. $M_\infty \approx 0.655$; $R_c = 4.5 \times 10^6$.



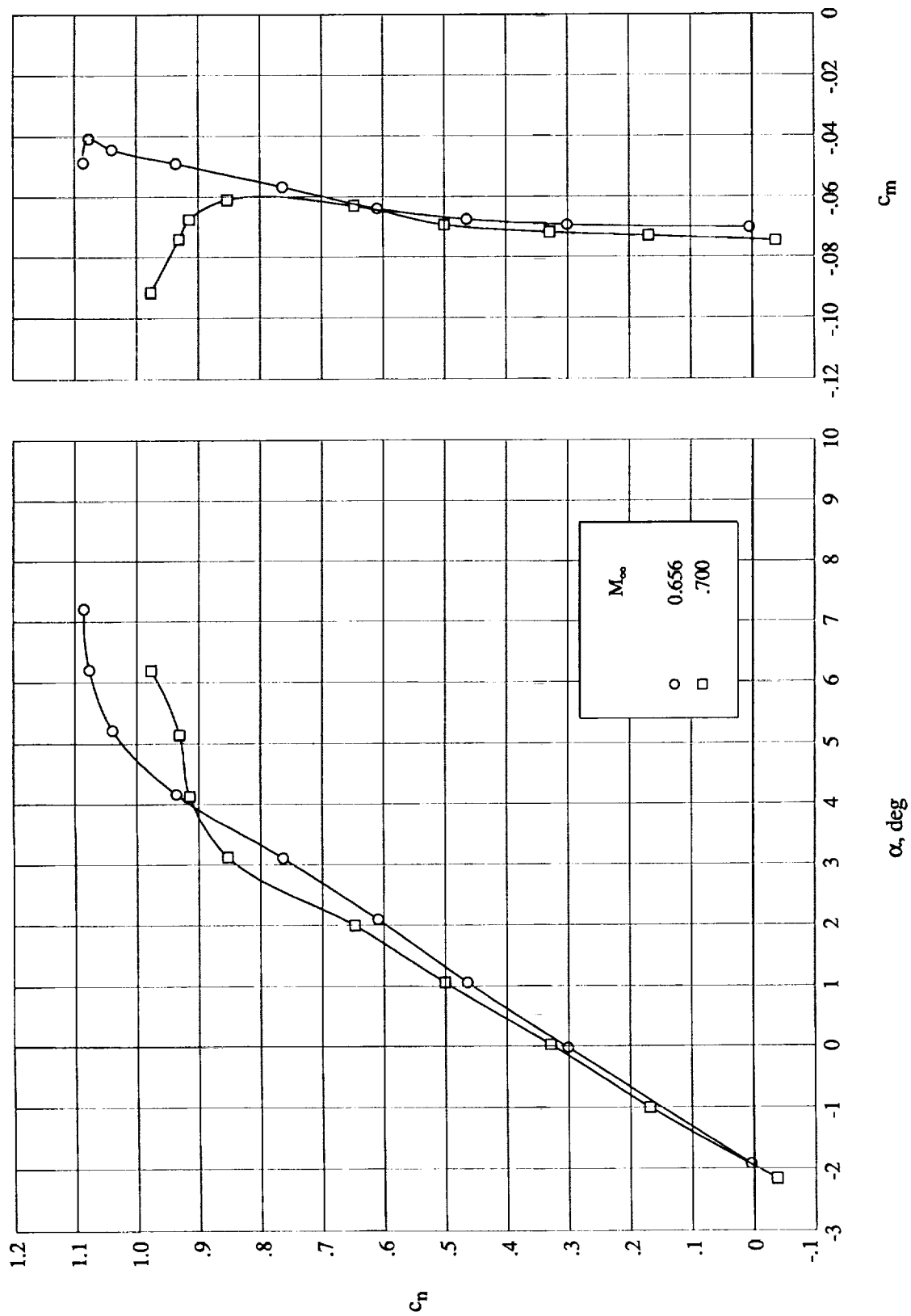
(b) Drag coefficient.

Figure 12. Continued.



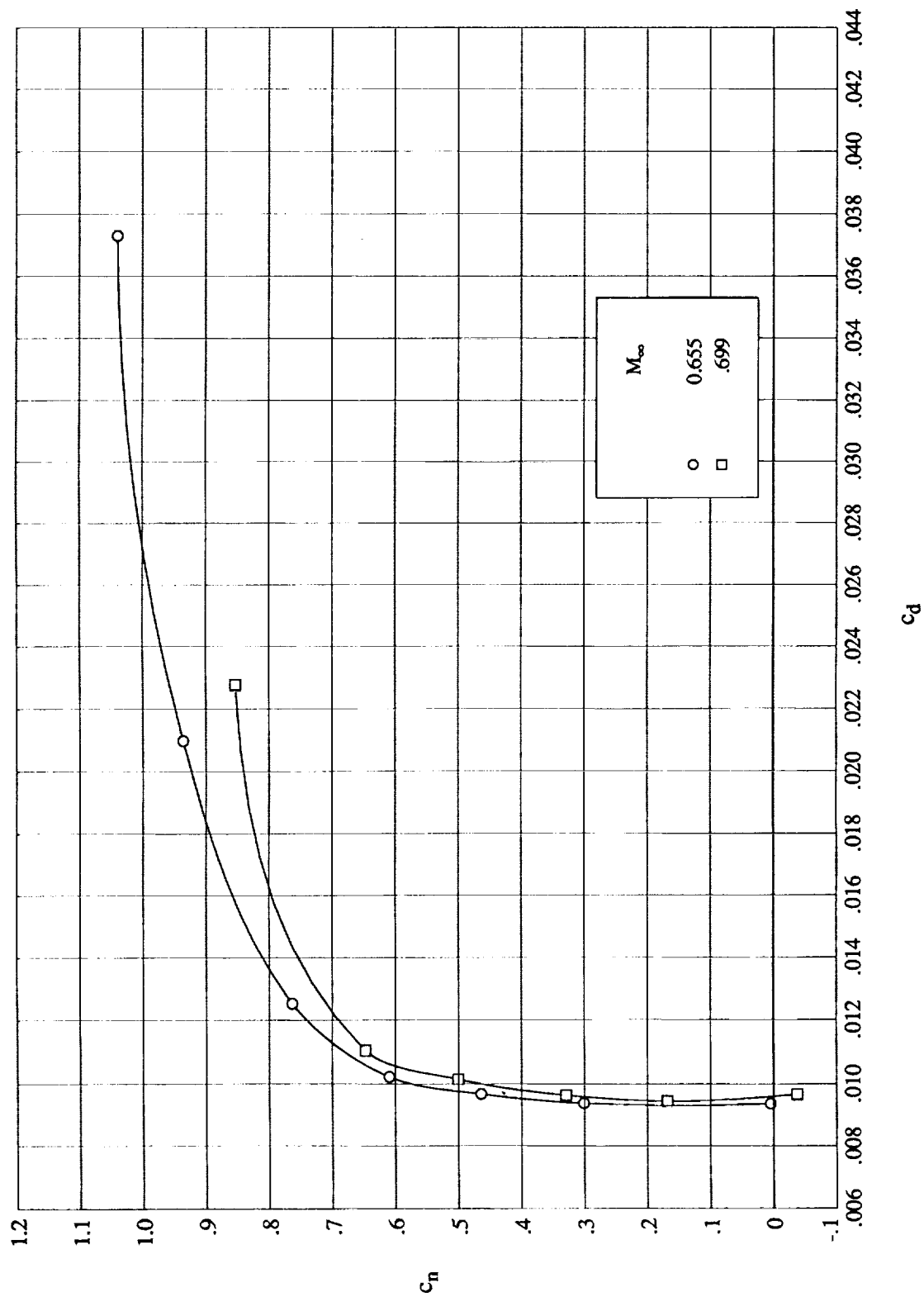
(c) Pressure distributions. Open symbols denote upper surface; "+" within symbol denotes lower surface.

Figure 12. Concluded.



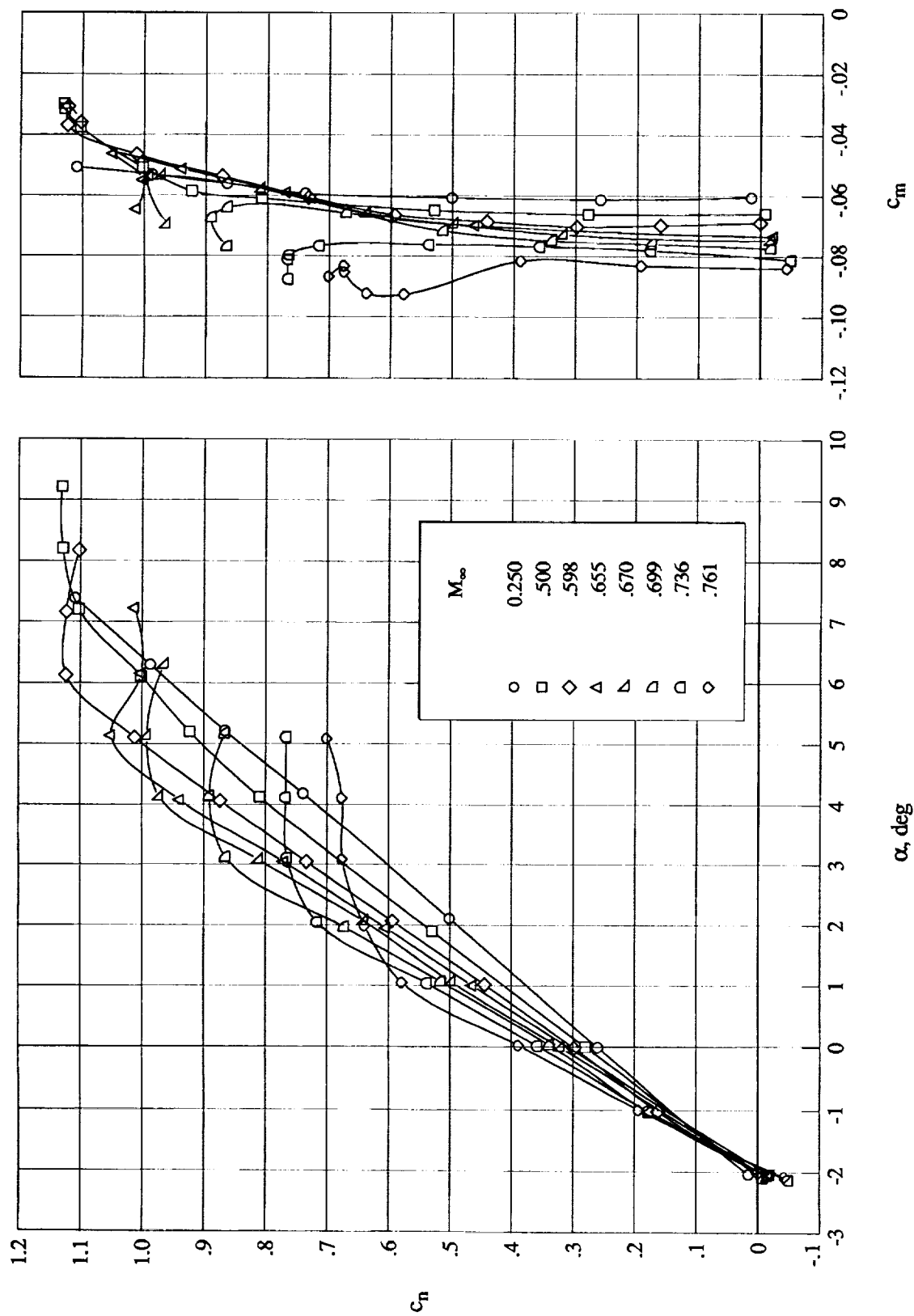
(a) Normal-force and pitching-moment coefficients. $R_c = 3.0 \times 10^6$.

Figure 13. Effect of free-stream Mach number at constant Reynolds number.



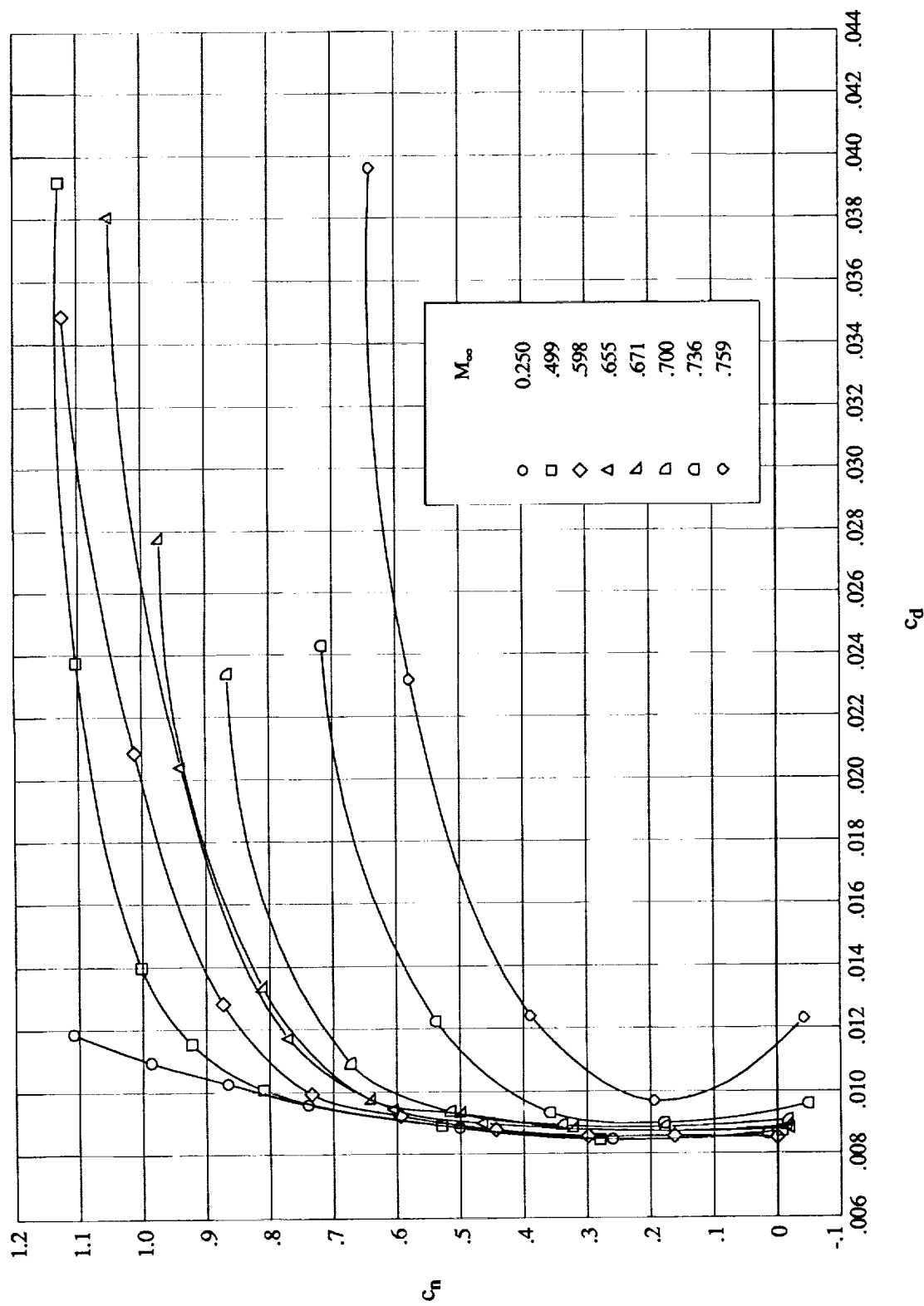
(b) Drag coefficient. $R_e = 3.0 \times 10^6$.

Figure 13. Continued.



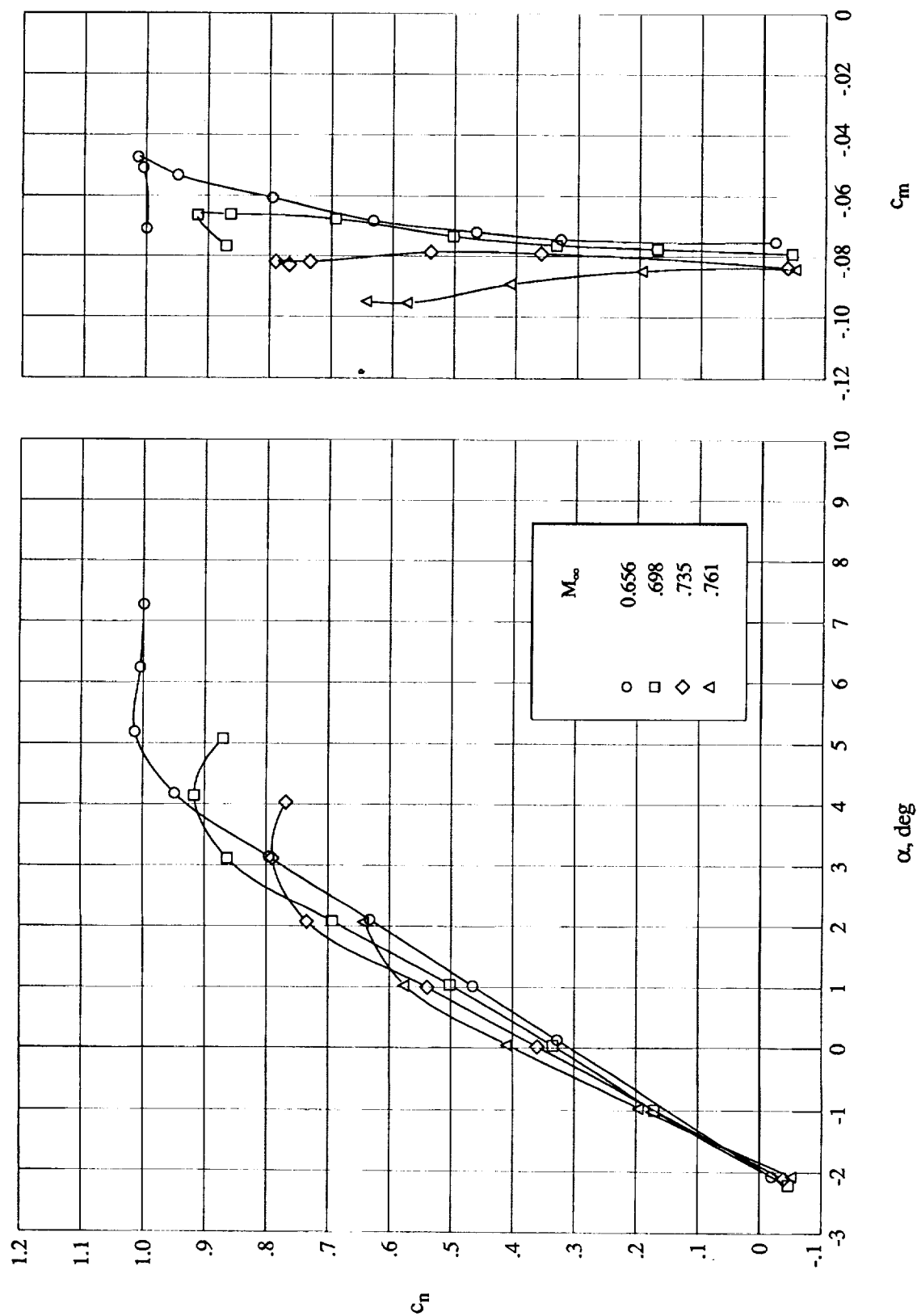
(c) Normal-force and pitching-moment coefficients. $R_c = 4.5 \times 10^6$.

Figure 13. Continued.



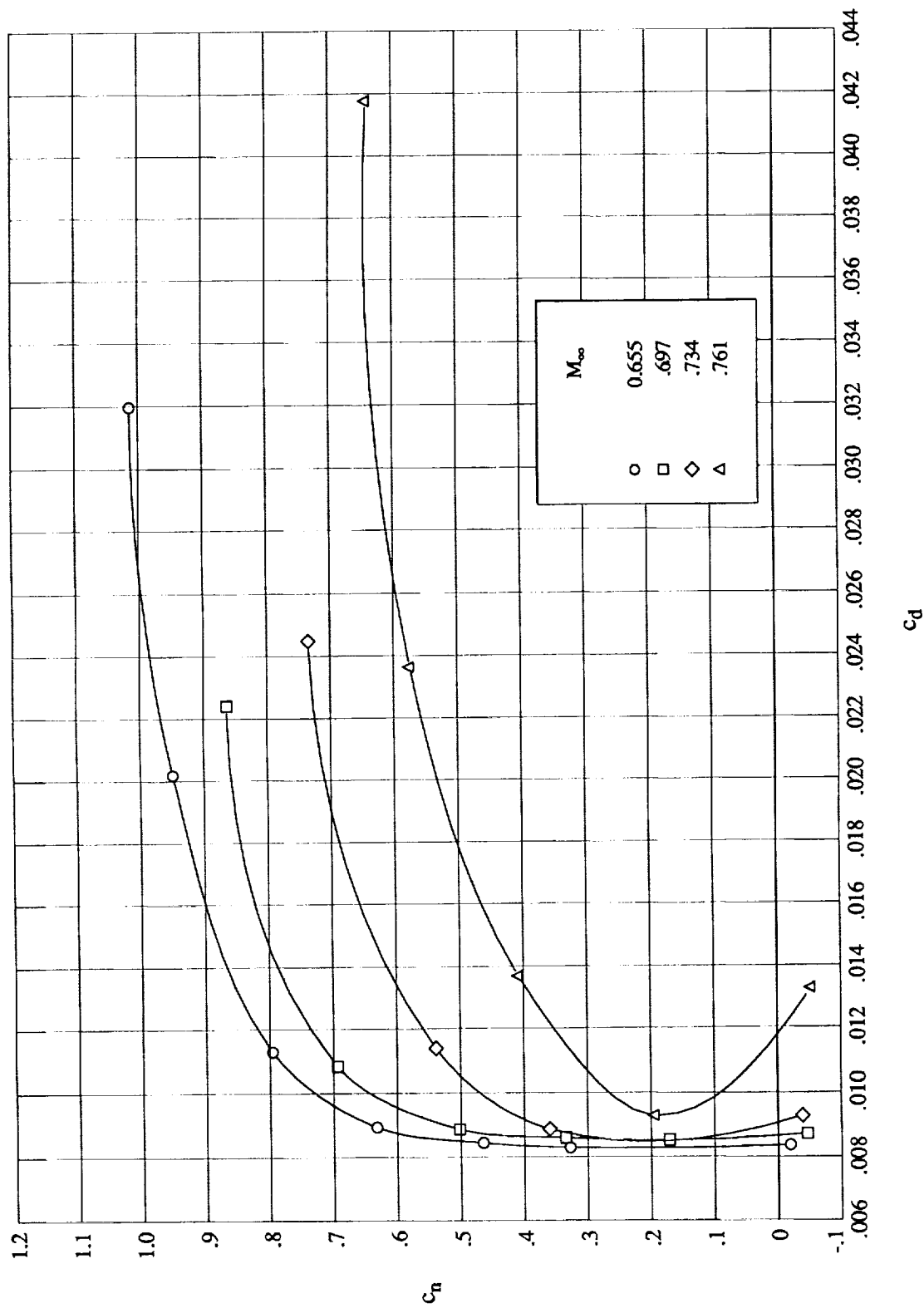
(d) Drag coefficient. $R_c = 4.5 \times 10^6$.

Figure 13. Continued.



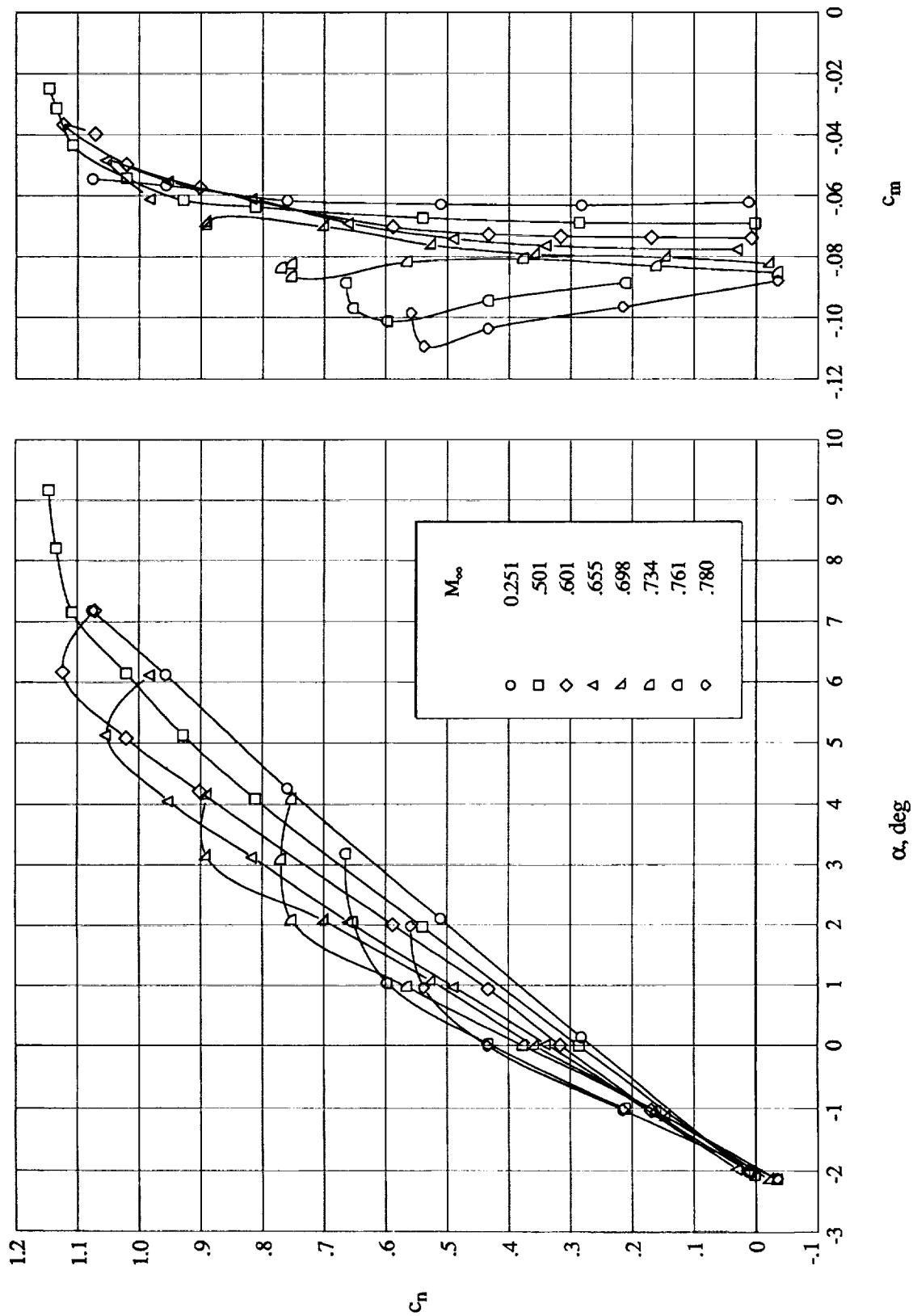
(e) Normal-force and pitching-moment coefficients. $R_c = 6.5 \times 10^6$.

Figure 13. Continued.



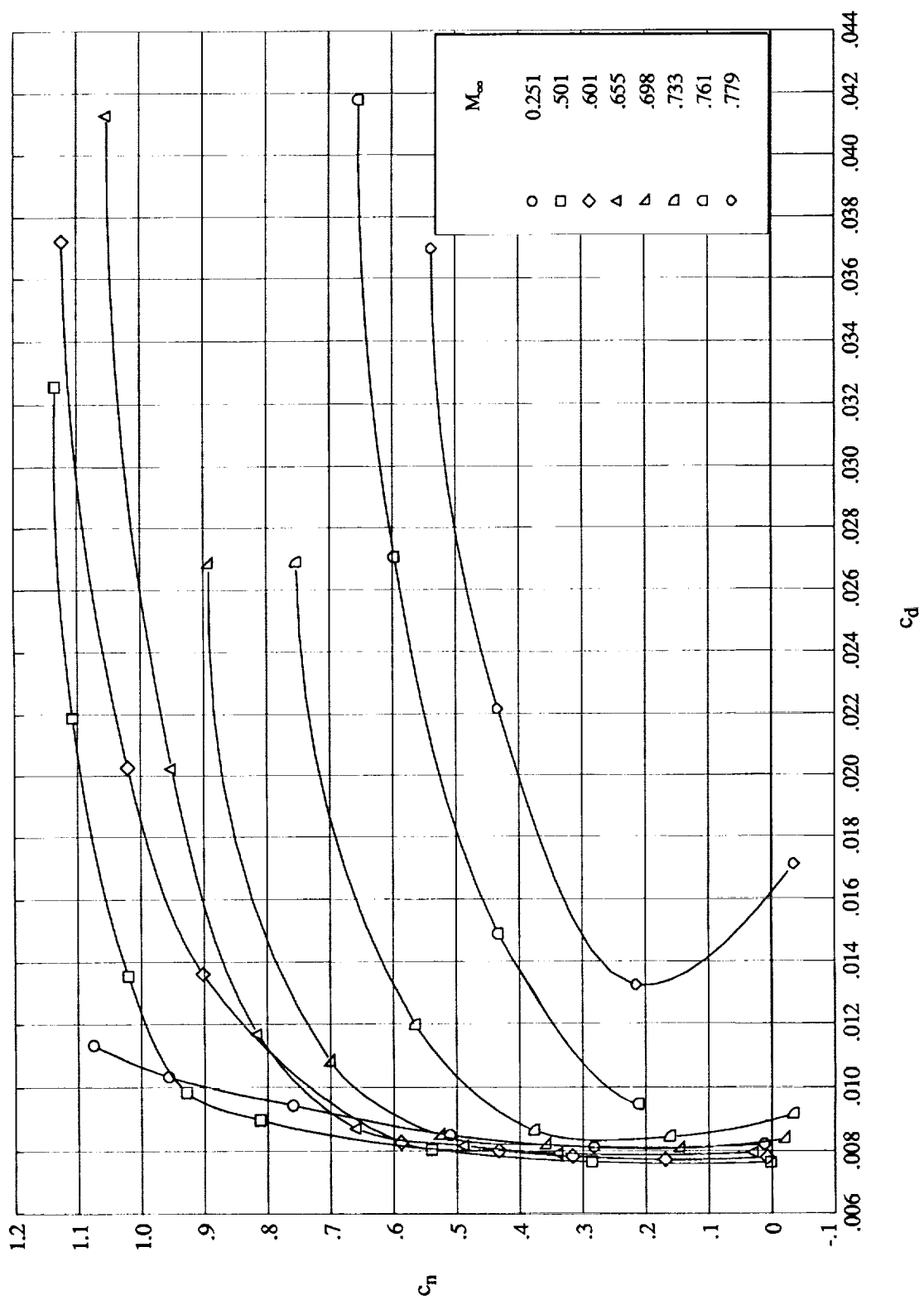
(f) Drag coefficient. $R_c = 6.5 \times 10^6$.

Figure 13. Continued.



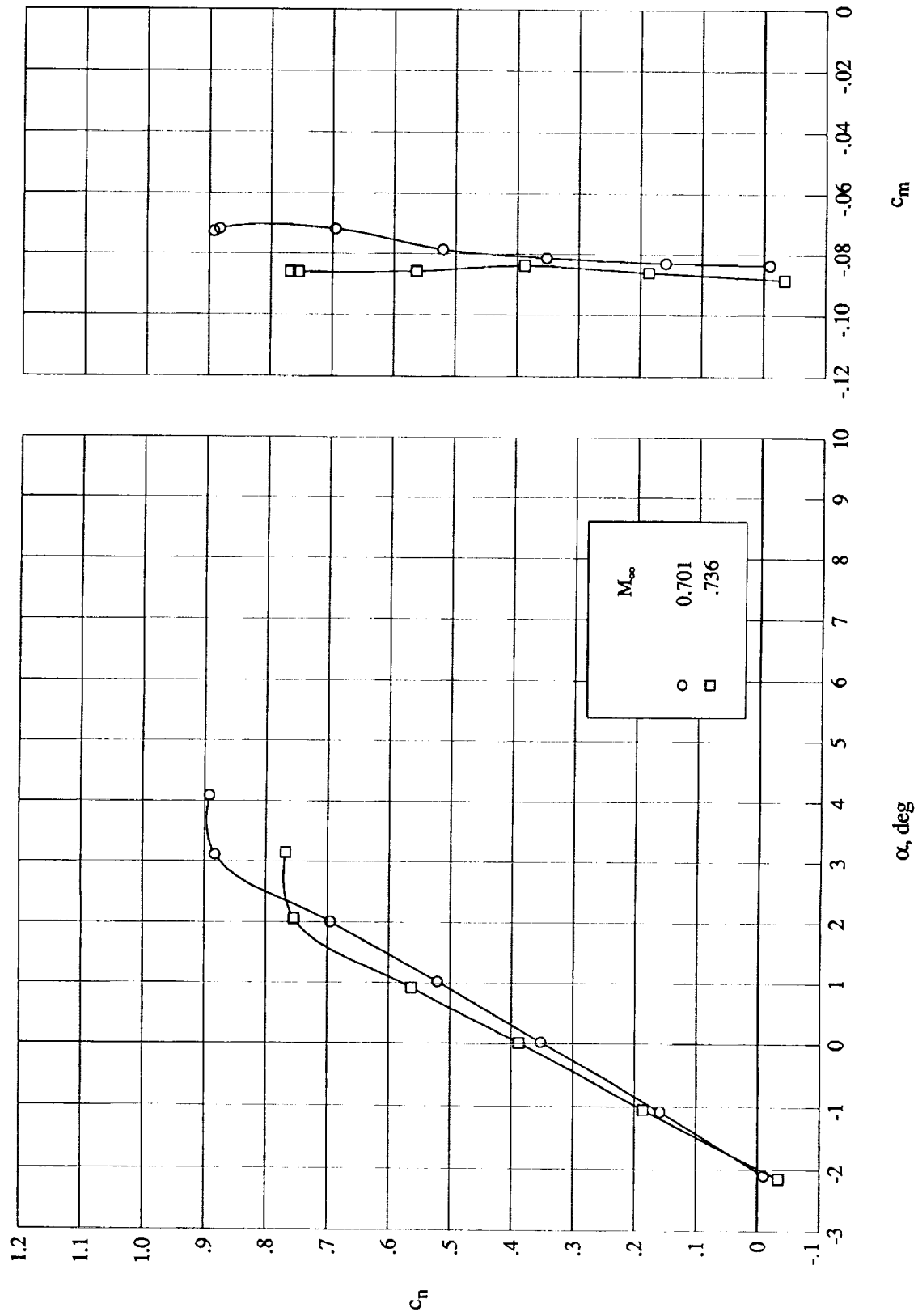
(g) Normal-force and pitching-moment coefficients. $R_c = 9.0 \times 10^6$.

Figure 13. Continued.



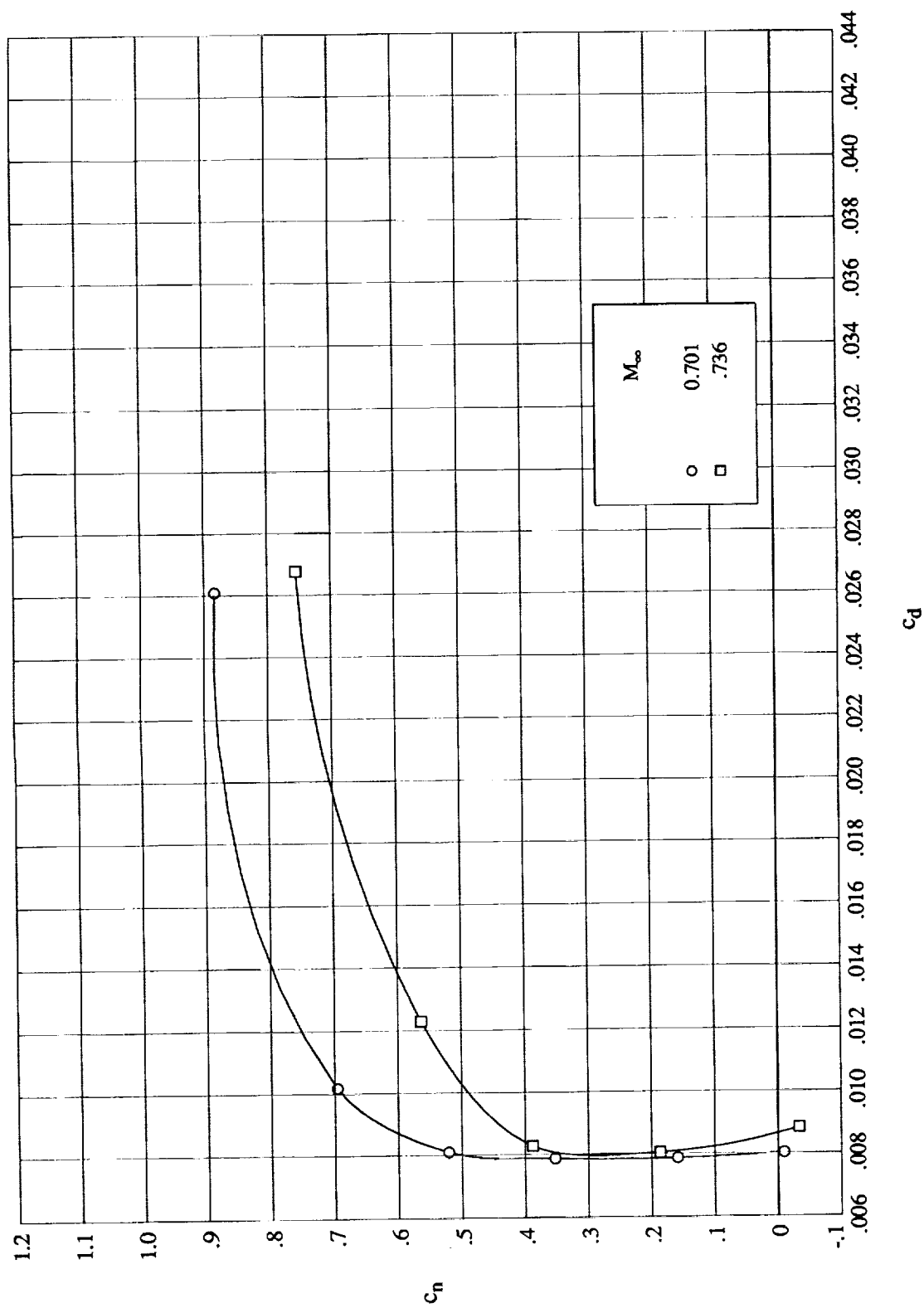
(h) Drag coefficient. $R_c = 9.0 \times 10^6$.

Figure 13. Continued.



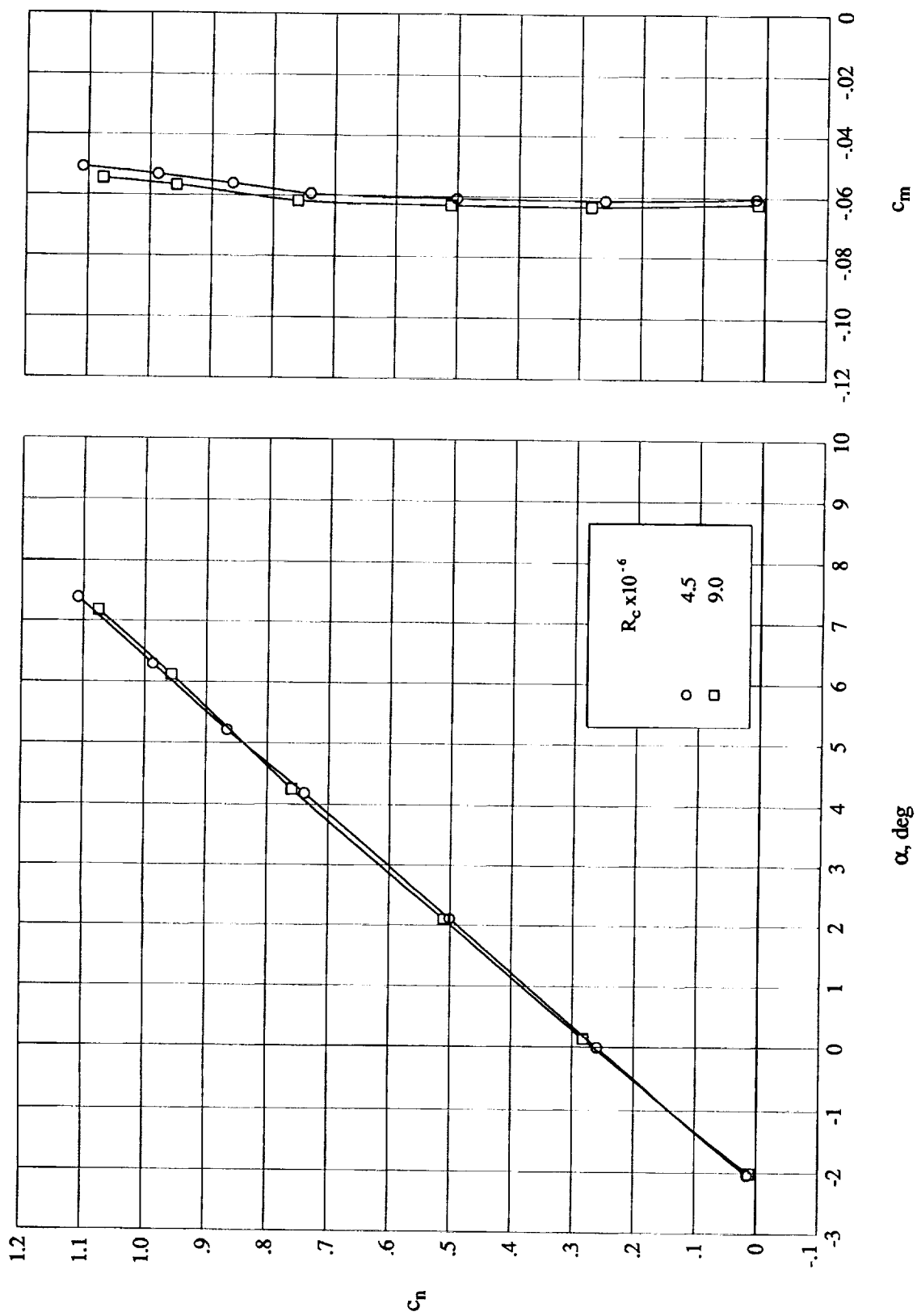
(i) Normal-force and pitching-moment coefficients. $R_c = 13.5 \times 10^6$.

Figure 13. Continued.



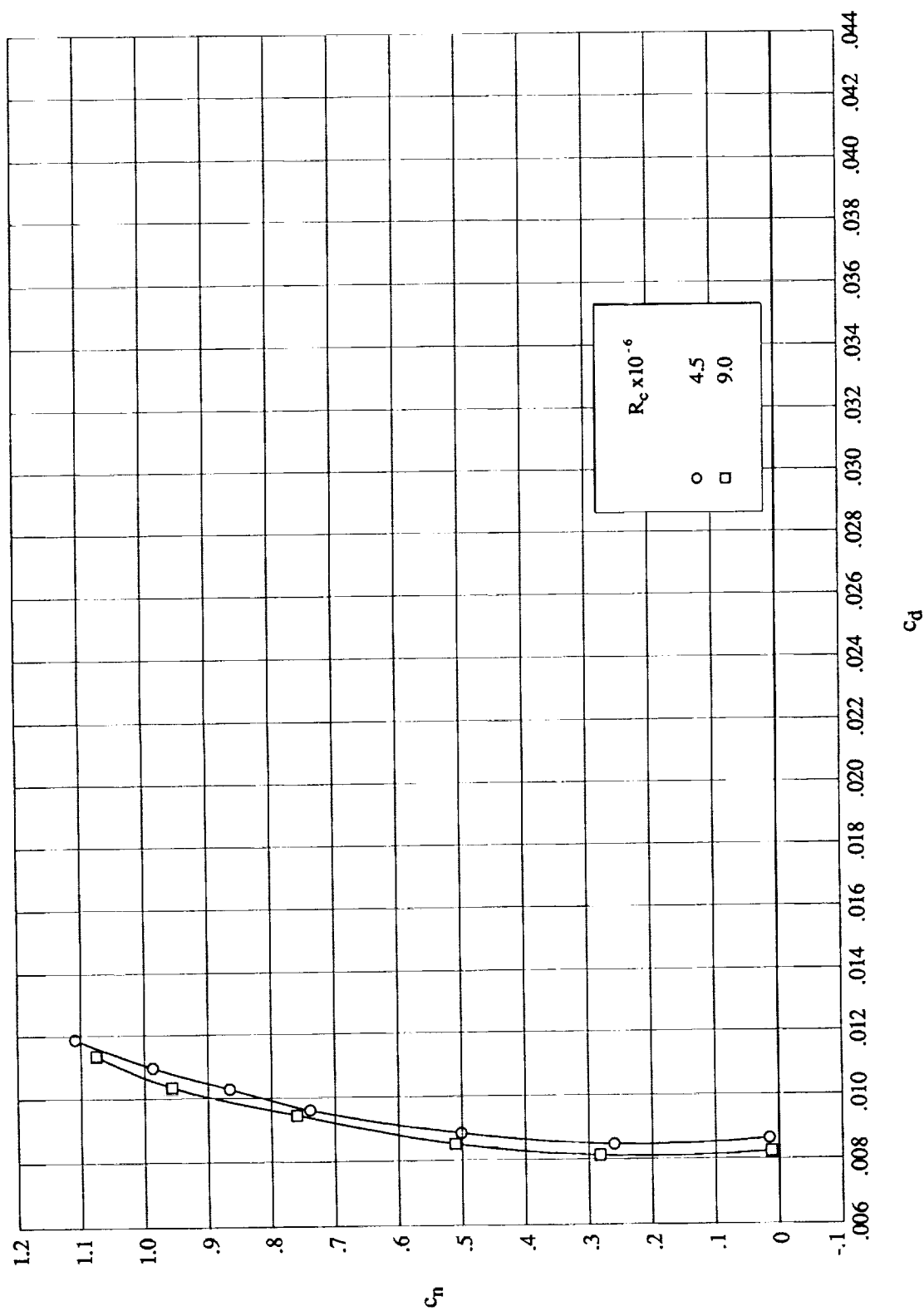
(j) Drag coefficient. $R_c = 13.5 \times 10^6$.

Figure 13. Concluded.



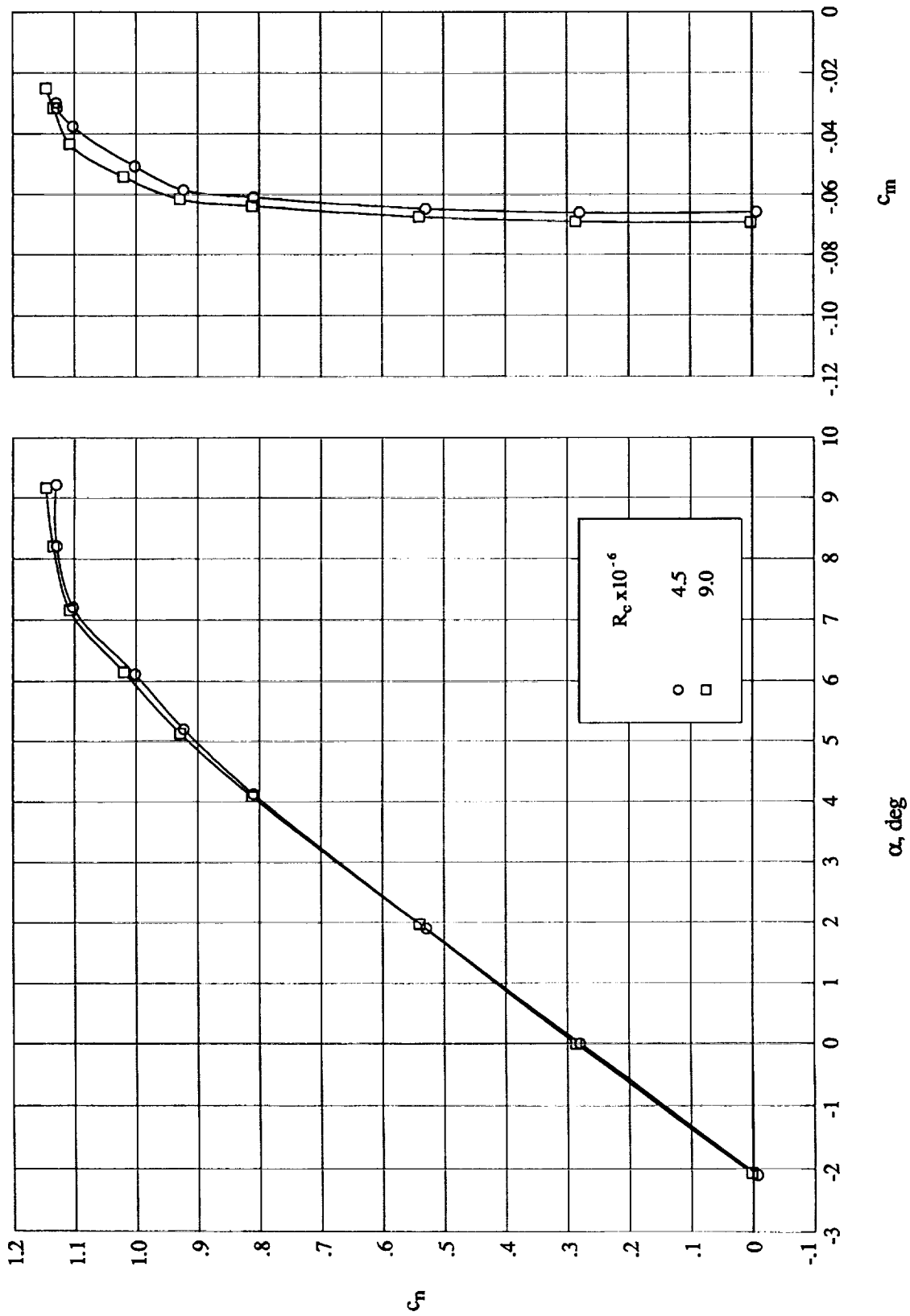
(a) Normal-force and pitching-moment coefficients. $M_\infty \approx 0.250$.

Figure 14. Effect of free-stream Reynolds number at constant Mach number.



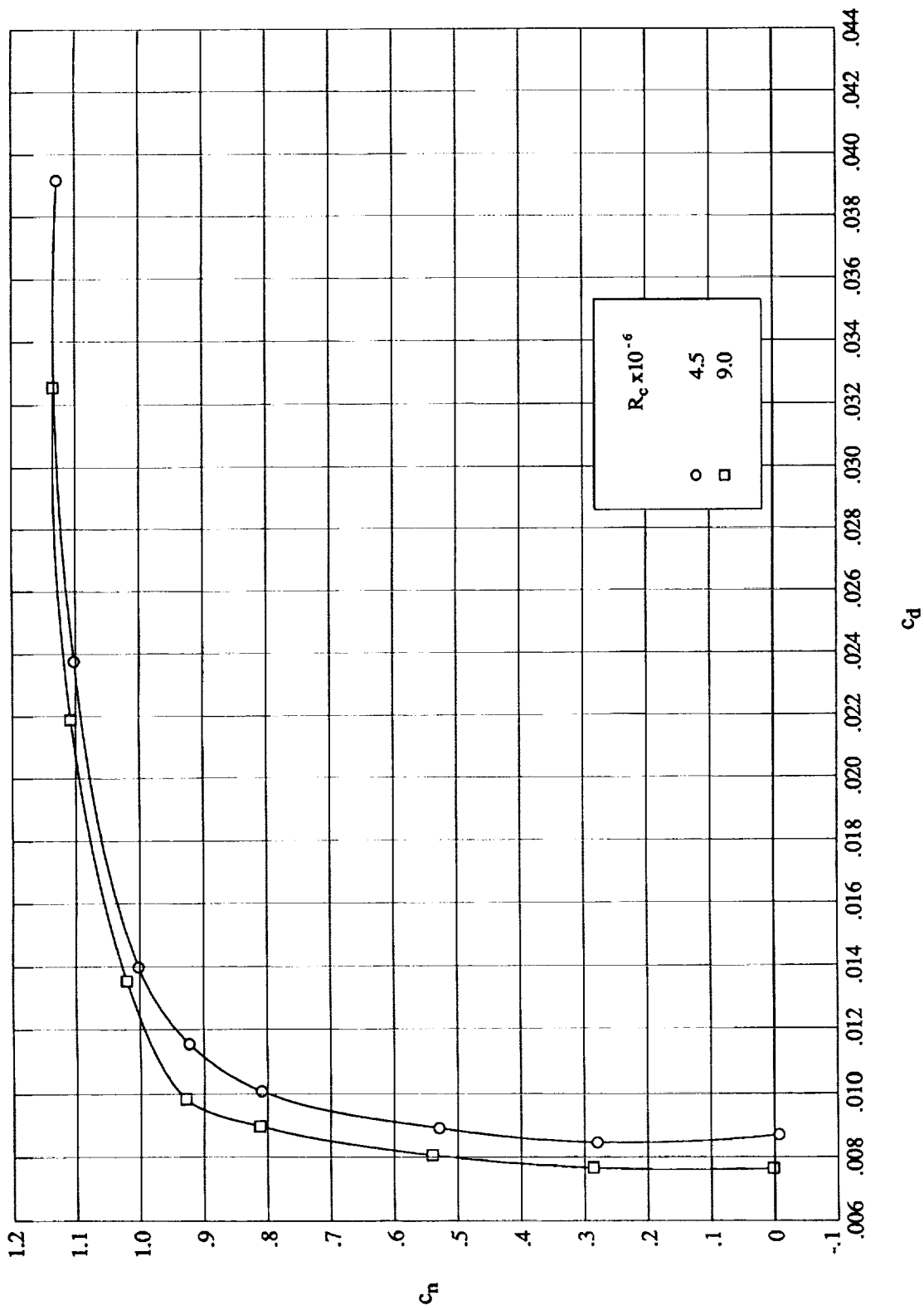
(b) Drag coefficient. $M_\infty \approx 0.250$.

Figure 14. Continued.



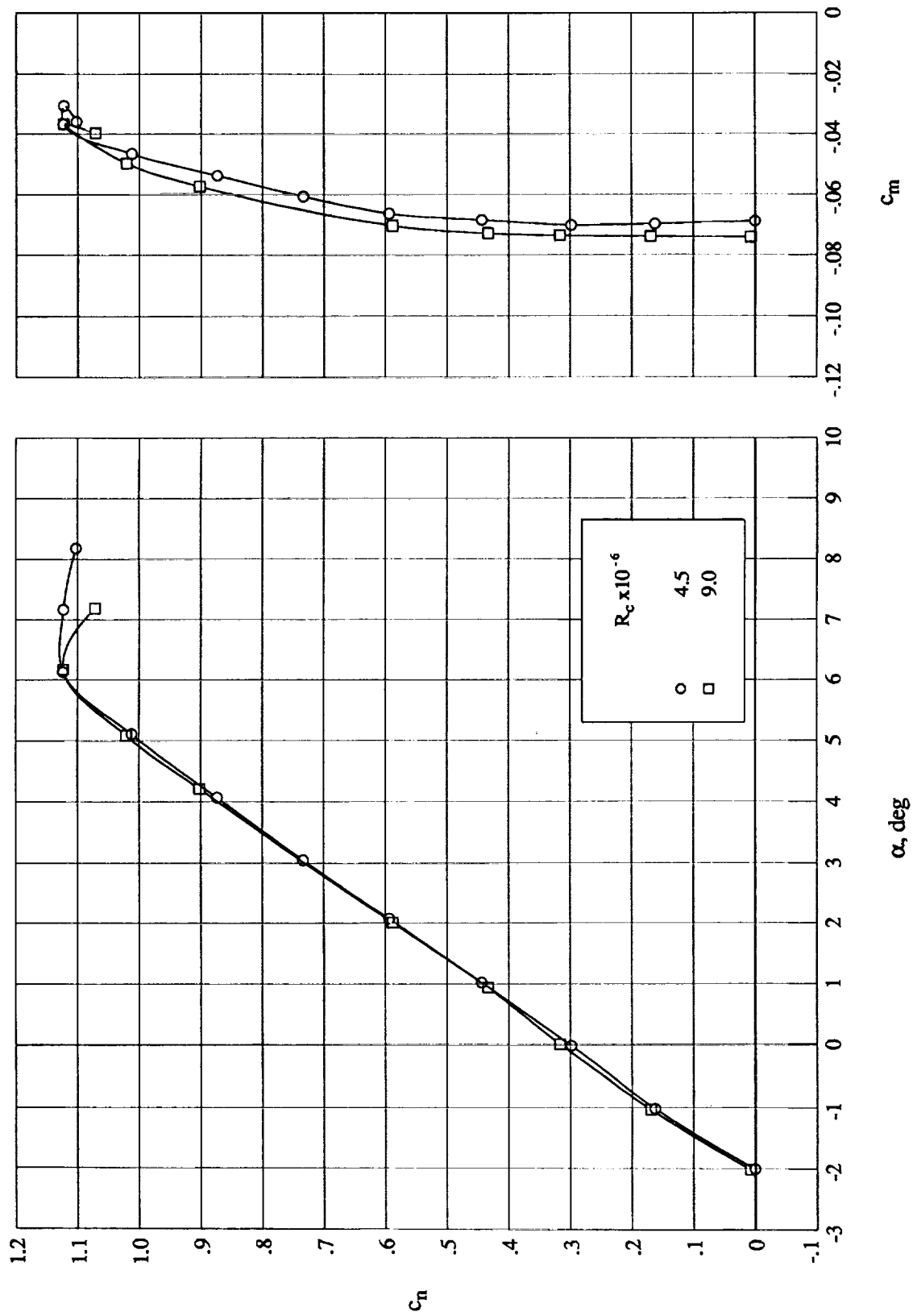
(c) Normal-force and pitching-moment coefficients. $M_\infty \approx 0.500$.

Figure 14. Continued.



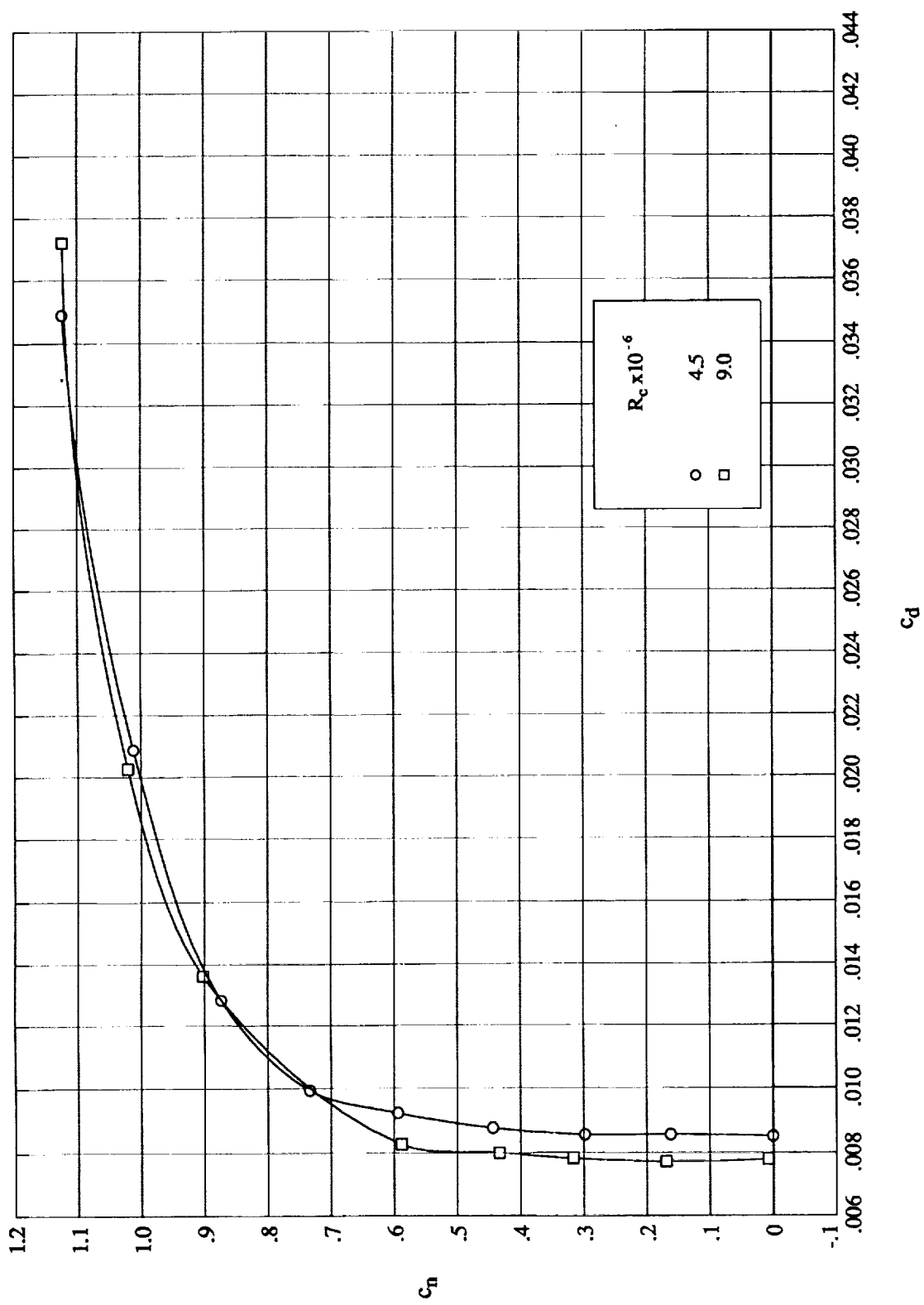
(d) Drag coefficient. $M_\infty \approx 0.500$.

Figure 14. Continued.



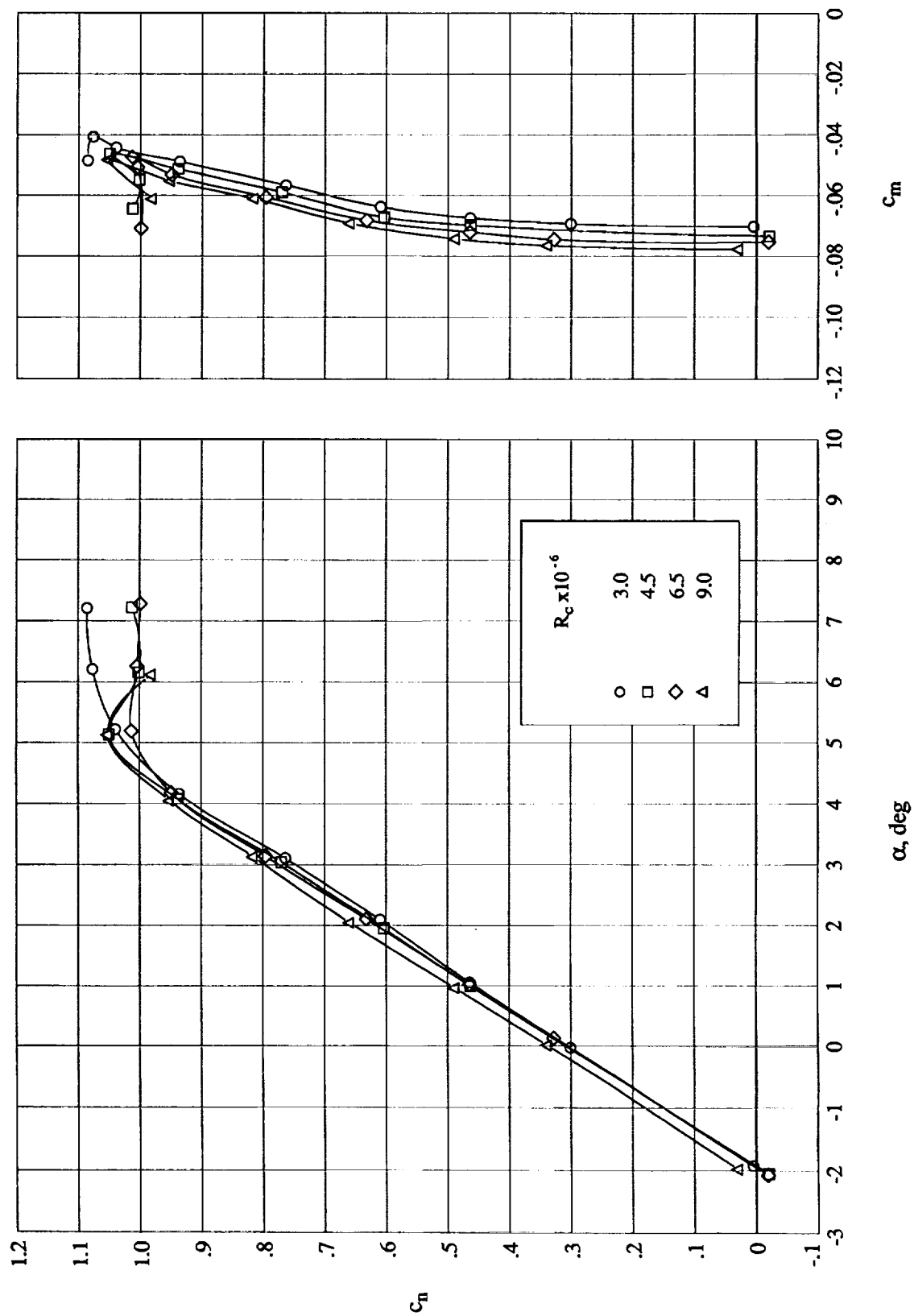
(e) Normal-force and pitching-moment coefficients. $M_\infty \approx 0.600$.

Figure 14. Continued.



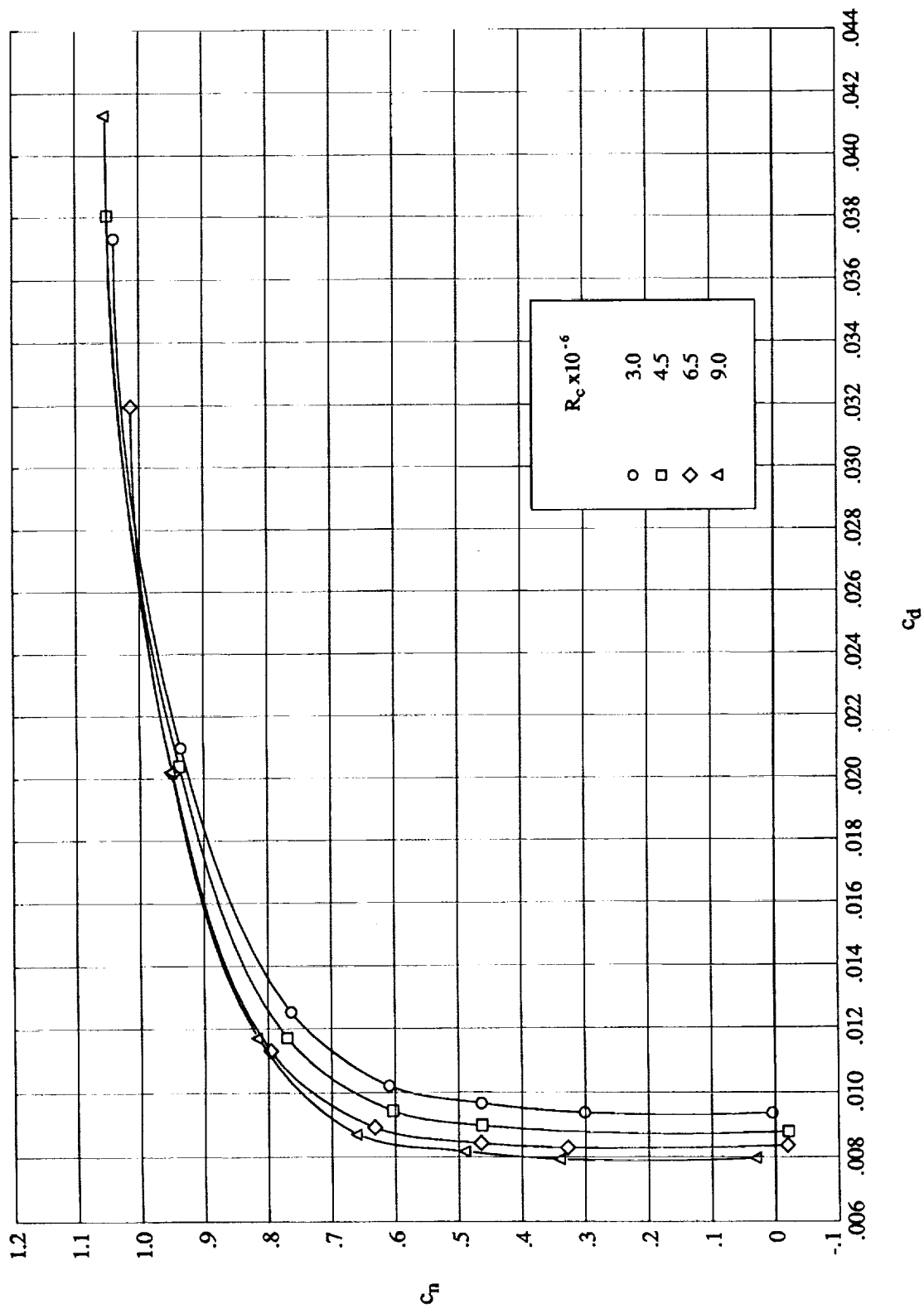
(f) Drag coefficient. $M_\infty \approx 0.600$.

Figure 14. Continued.



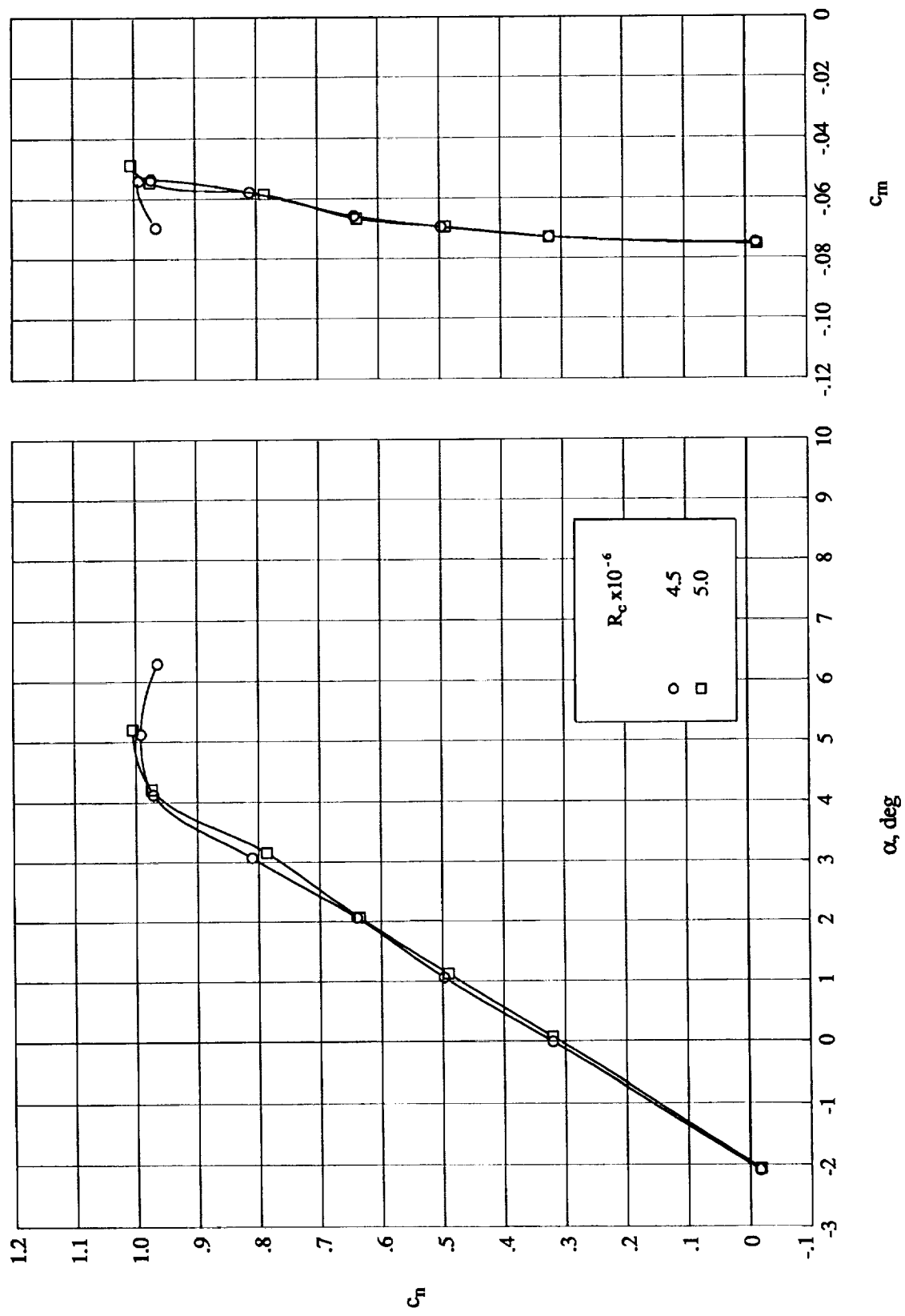
(g) Normal-force and pitching-moment coefficients. $M_\infty \approx 0.655$.

Figure 14. Continued.



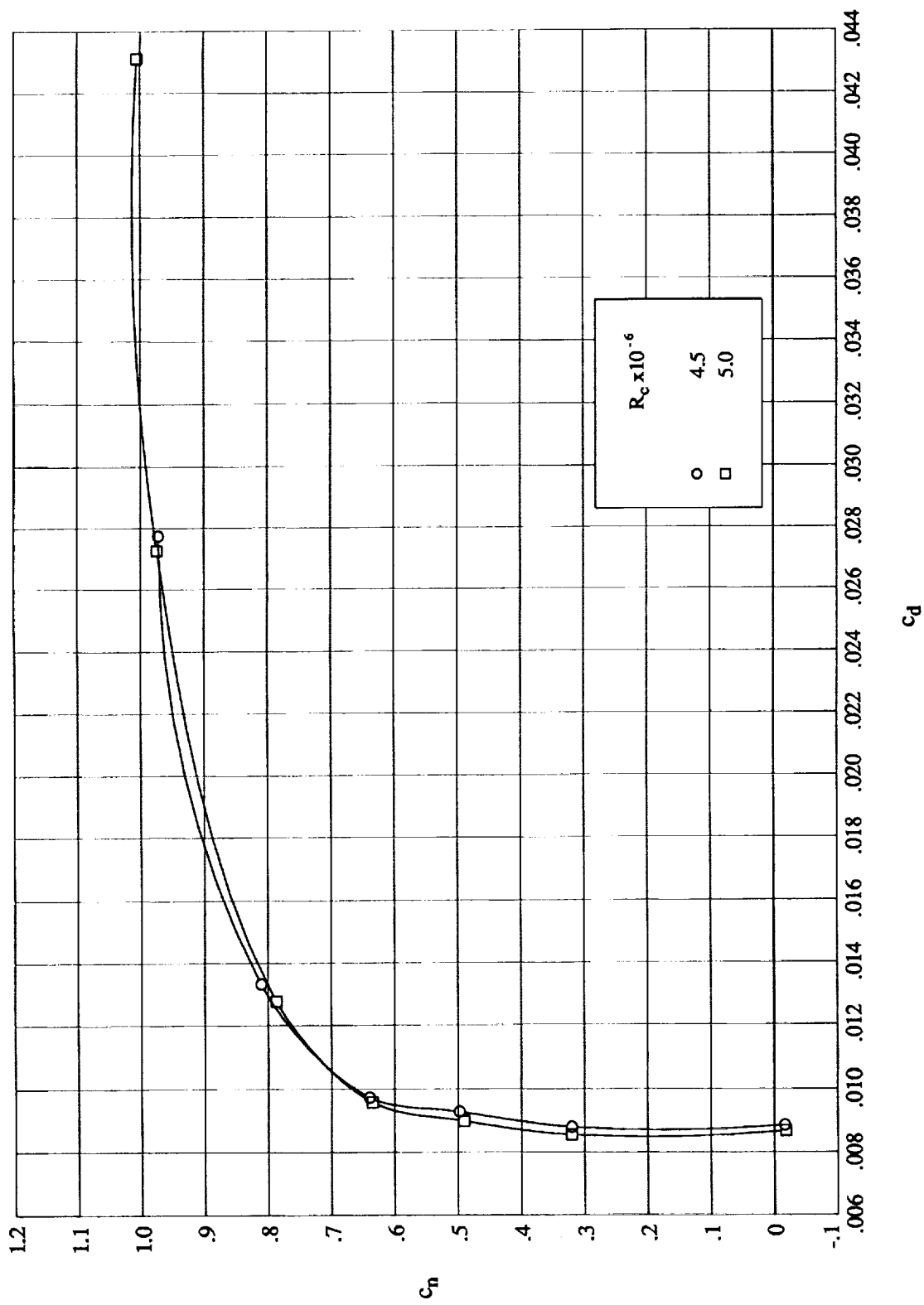
(h) Drag coefficient. $M_\infty \approx 0.655$.

Figure 14. Continued.



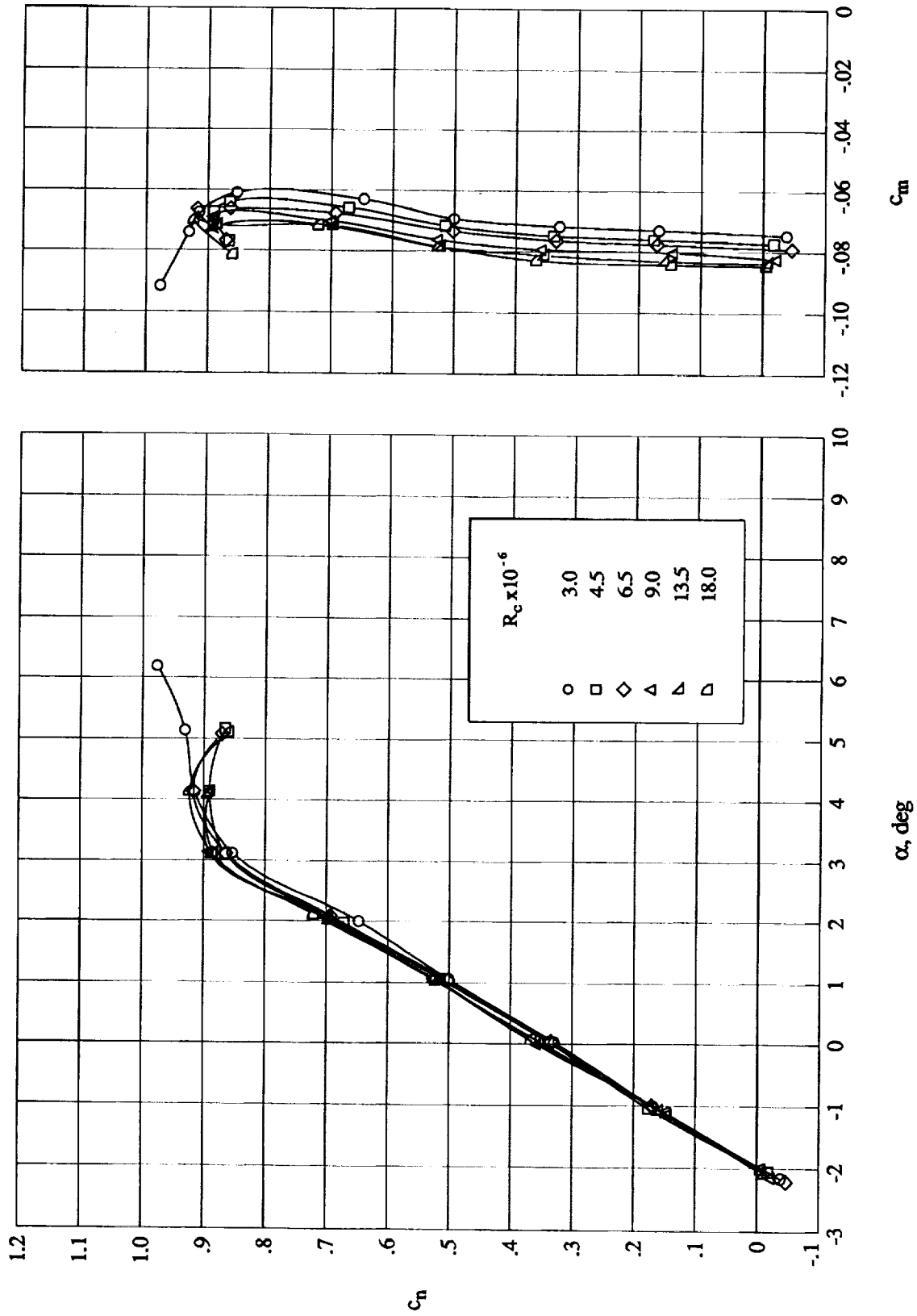
(i) Normal-force and pitching-moment coefficients. $M_\infty \approx 0.670$.

Figure 14. Continued.



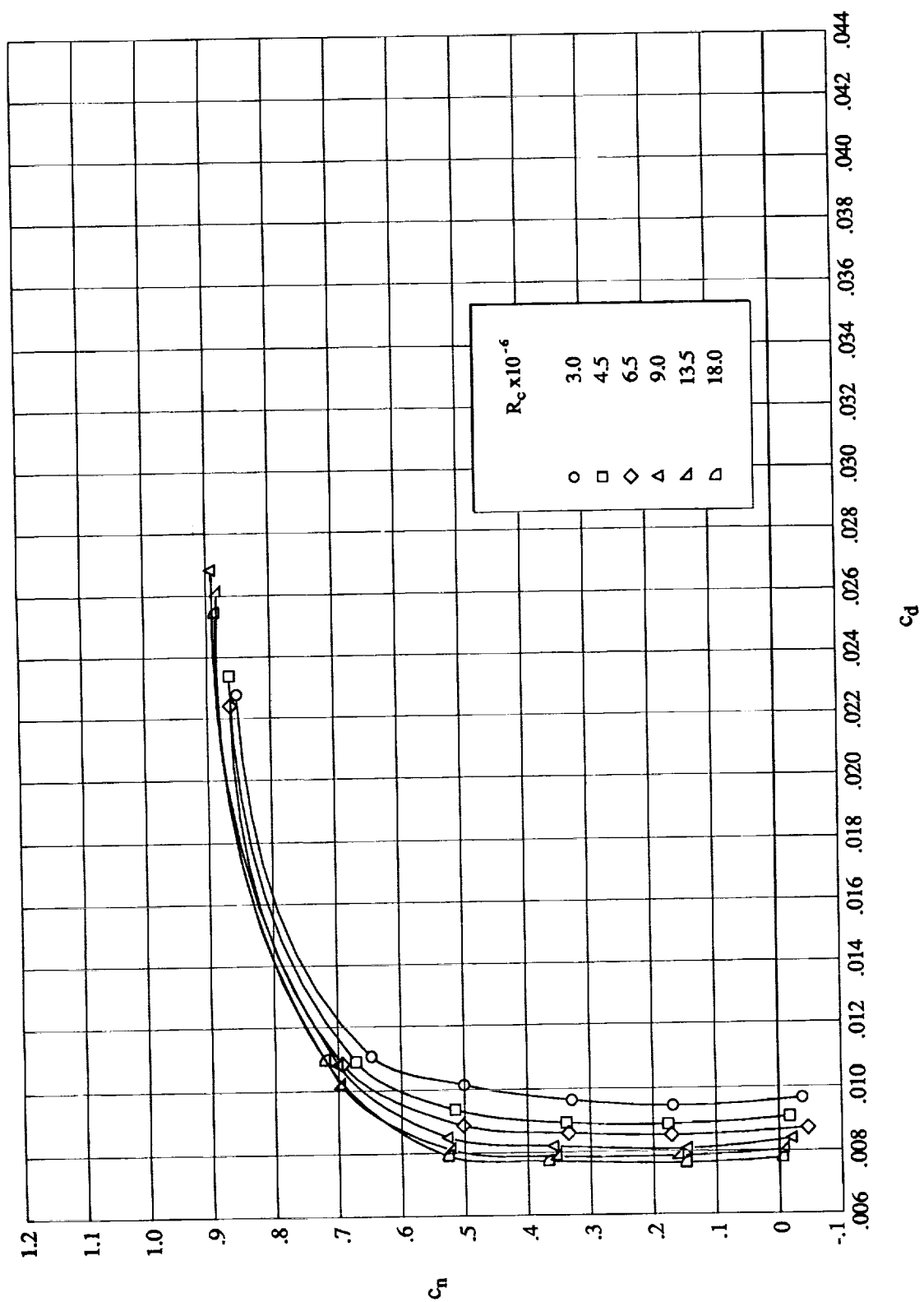
(j) Drag coefficient. $M_\infty \approx 0.670$.

Figure 14. Continued.



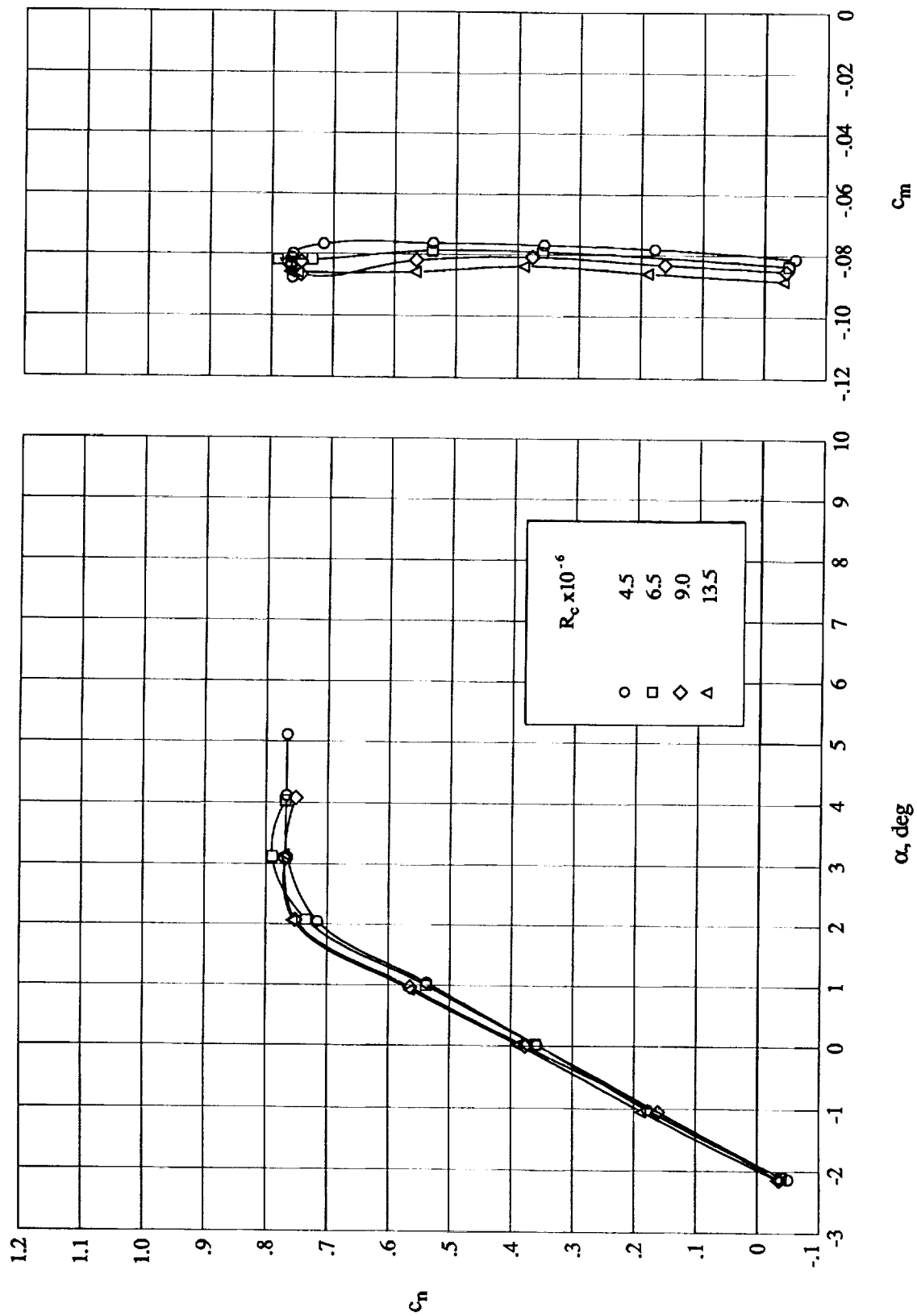
(k) Normal-force and pitching-moment coefficients. $M_\infty \approx 0.700$.

Figure 14. Continued.



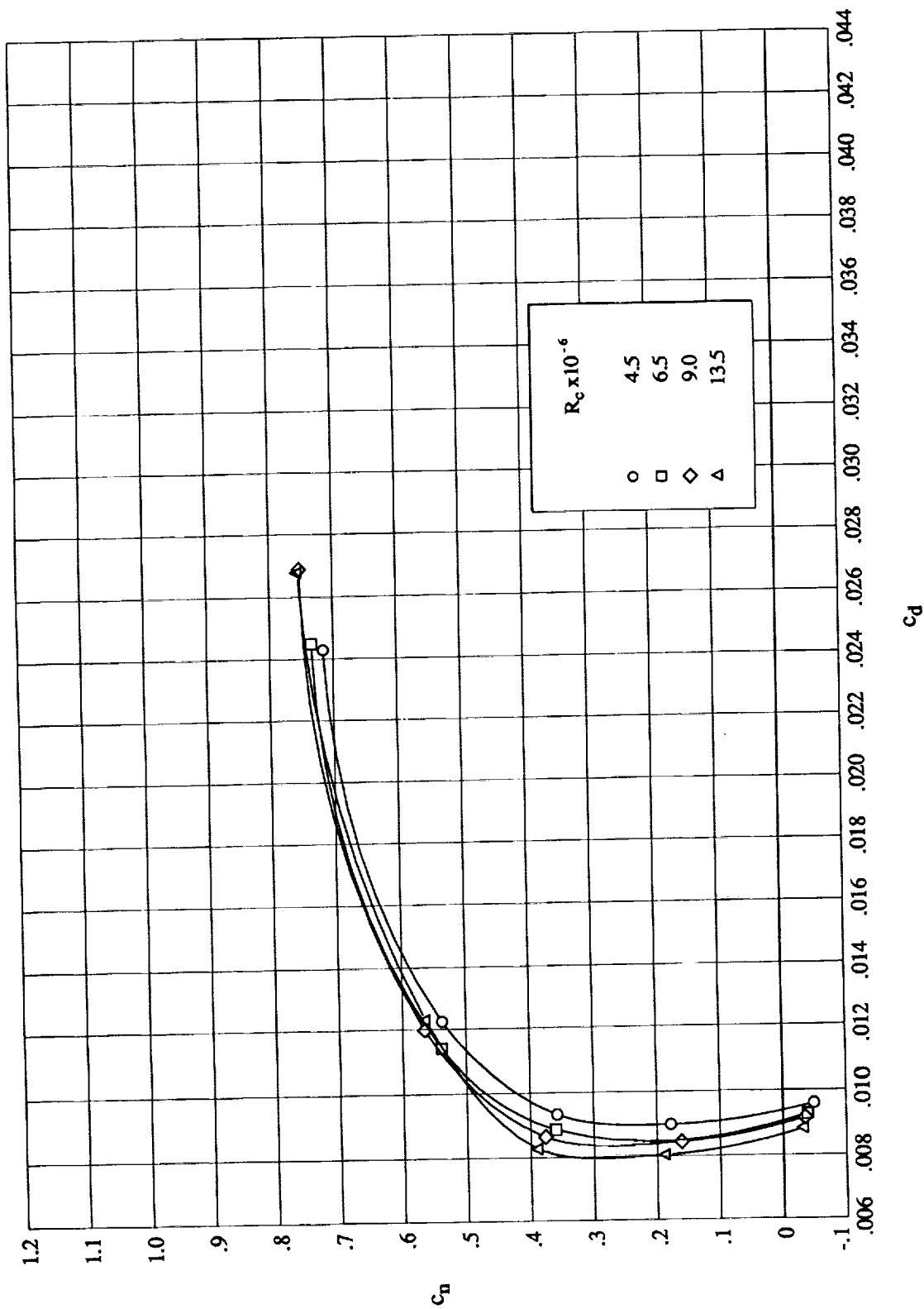
(1) Drag coefficient. $M_\infty \approx 0.700$.

Figure 14. Continued.



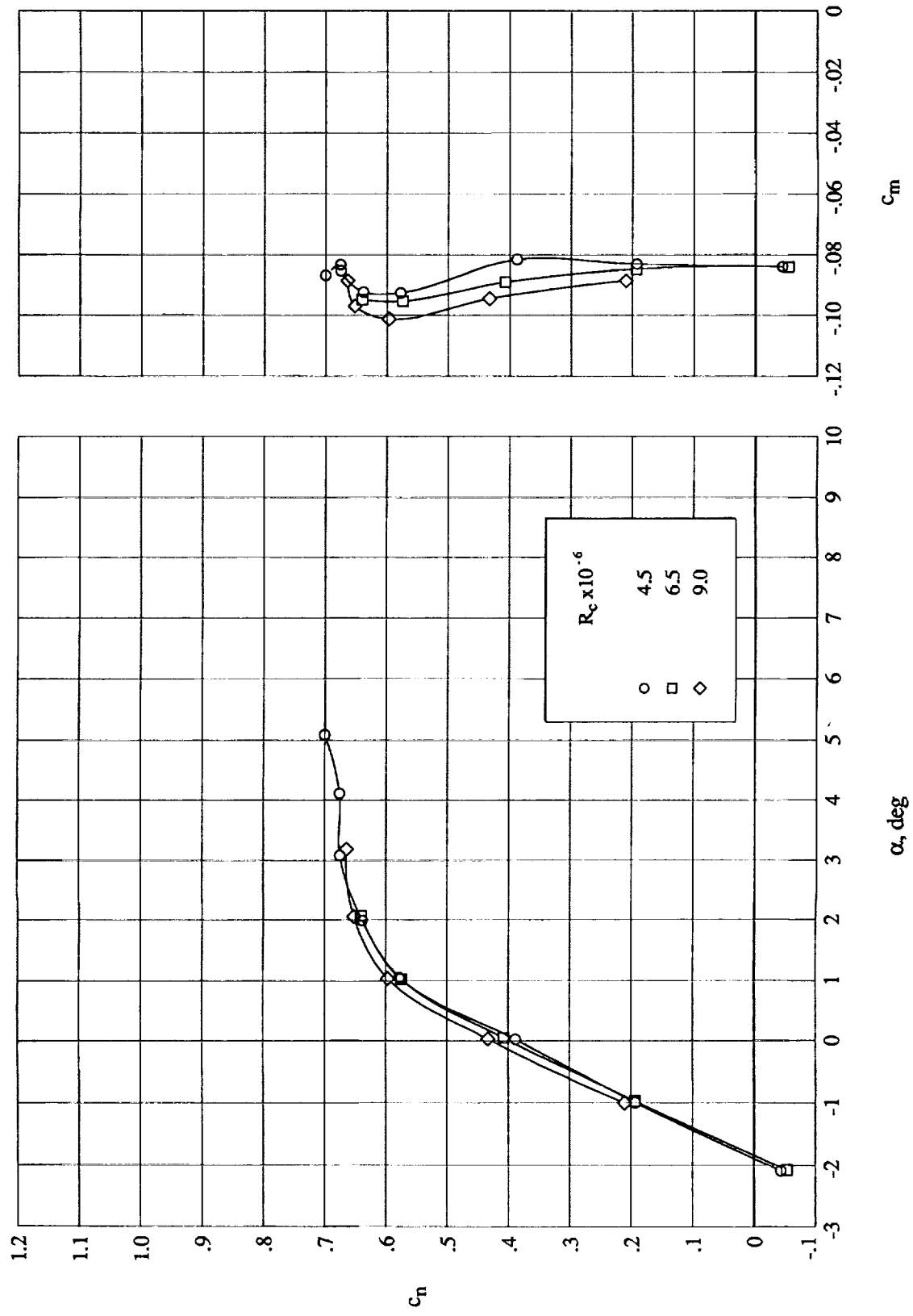
(m) Normal-force and pitching-moment coefficients. $M_\infty \approx 0.735$.

Figure 14. Continued.



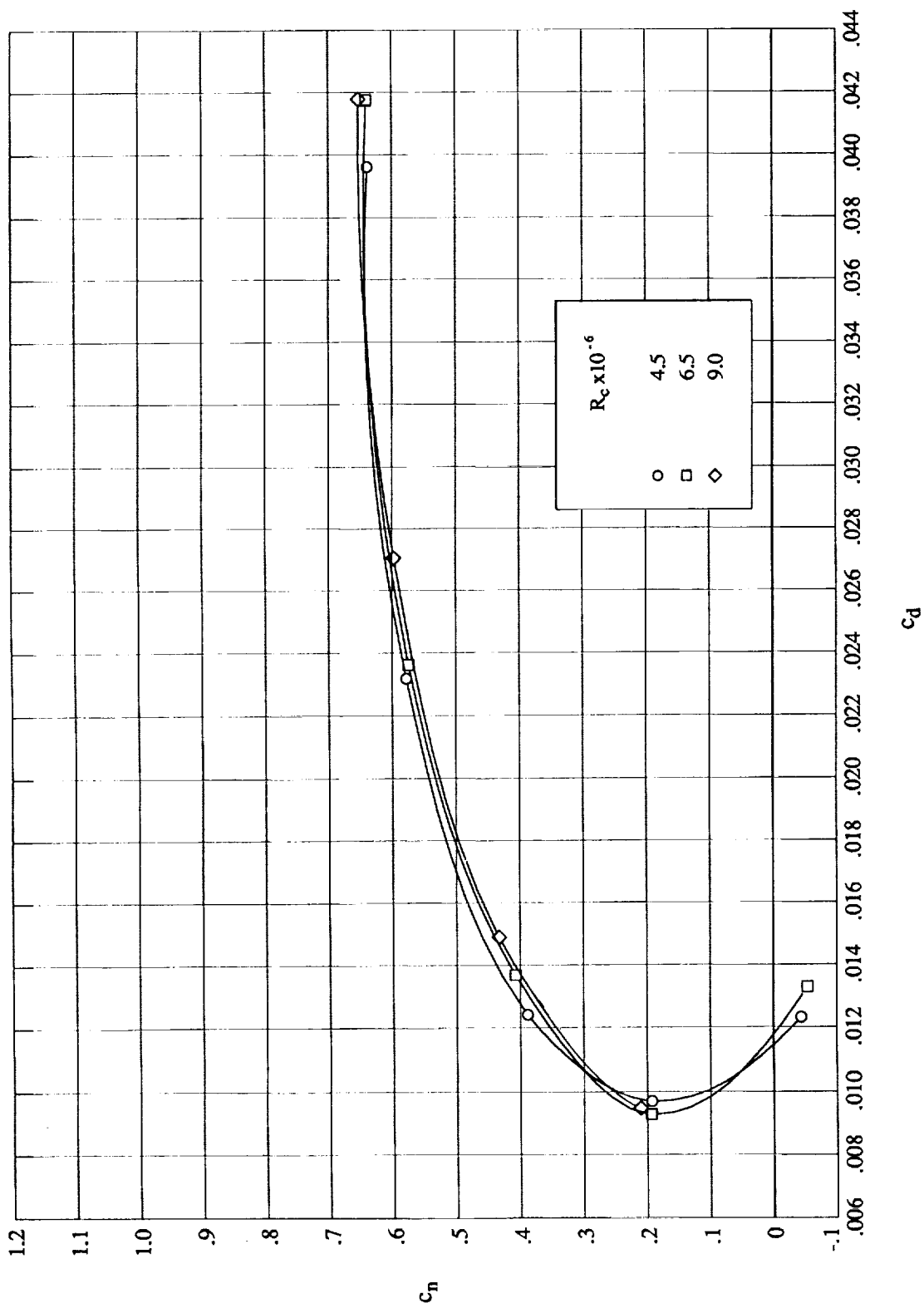
(n) Drag coefficient. $M_\infty \approx 0.735$.

Figure 14. Continued.



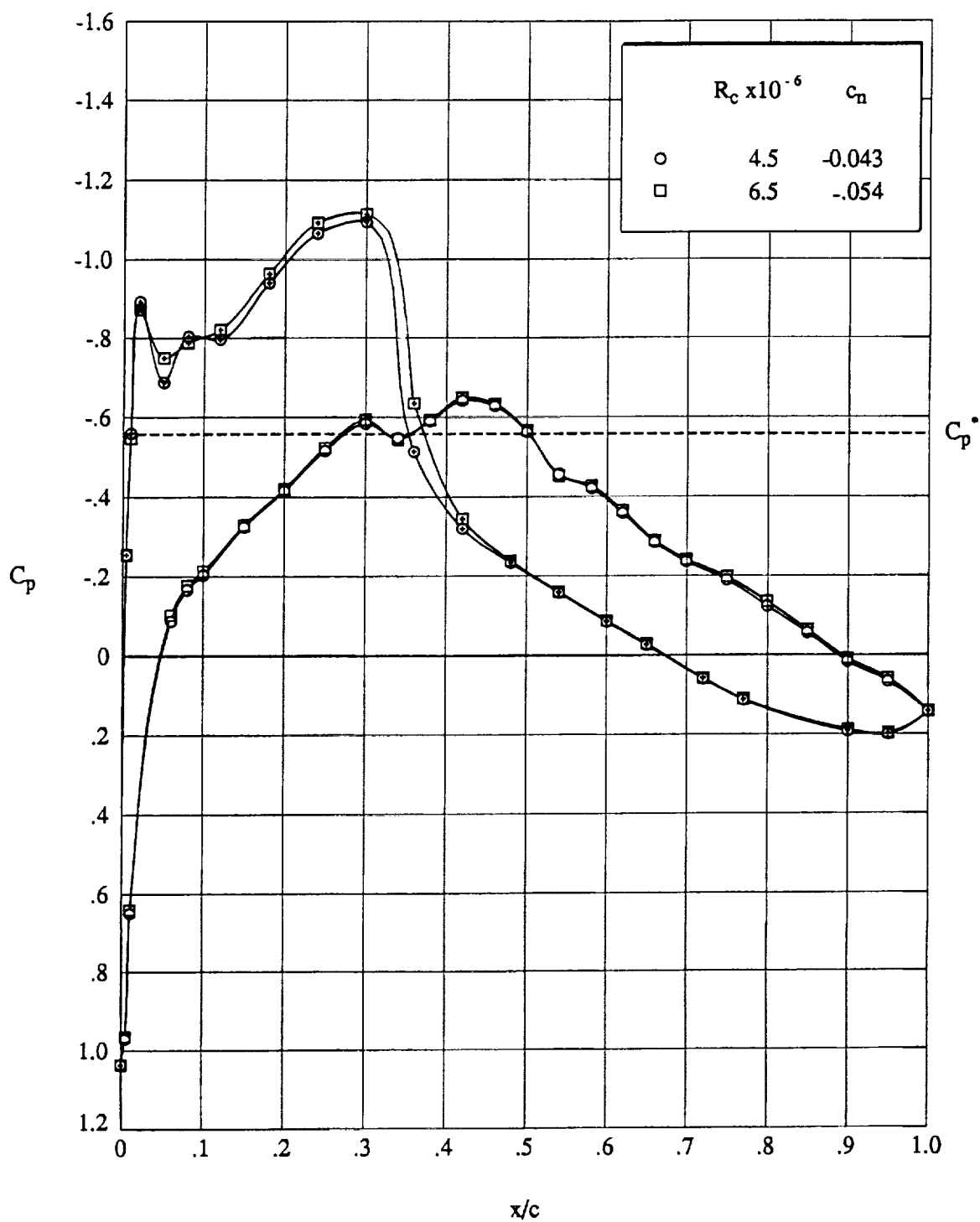
(o) Normal-force and pitching-moment coefficients. $M_\infty \approx 0.760$.

Figure 14. Continued.



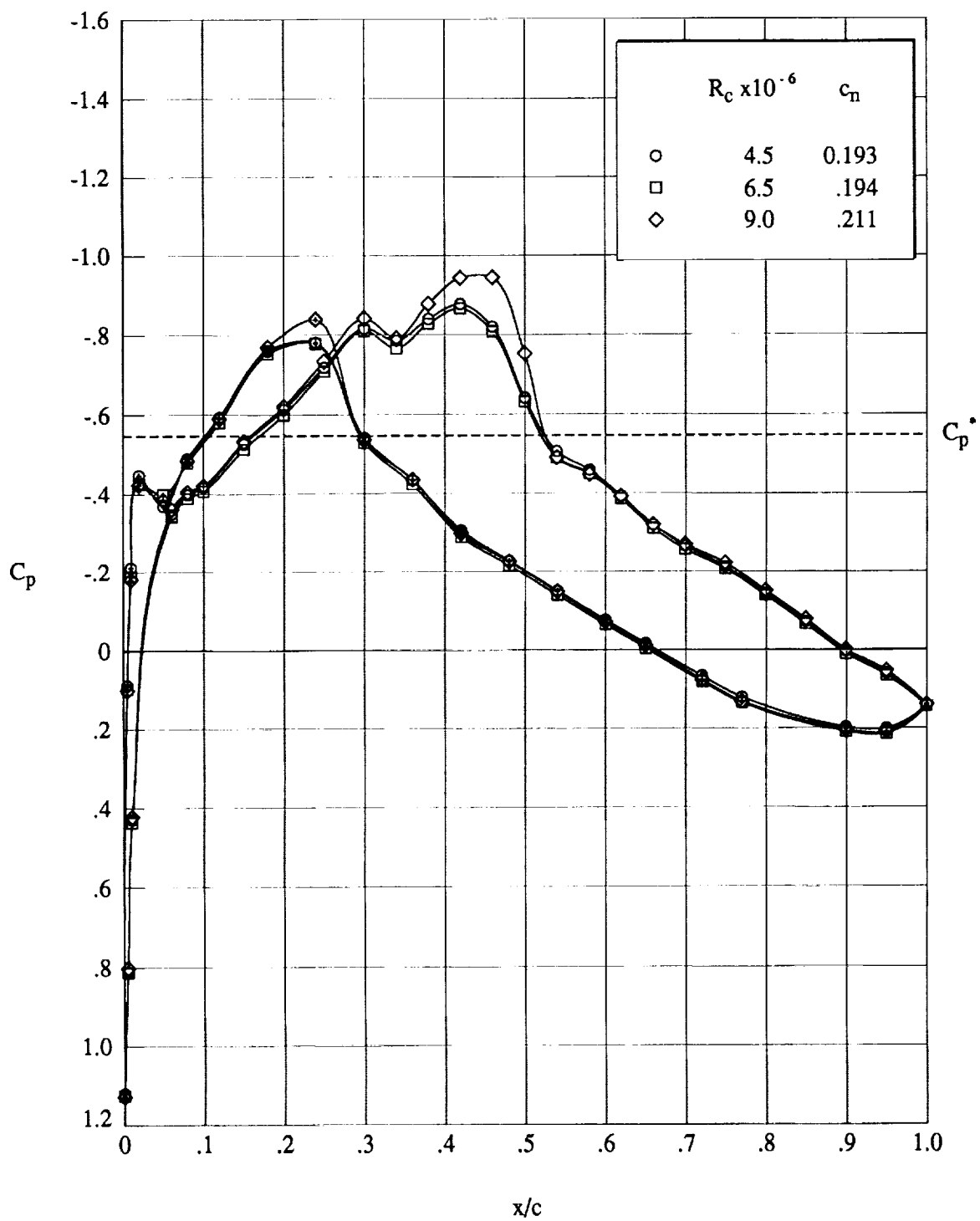
(p) Drag coefficient. $M_\infty \approx 0.760$.

Figure 14. Concluded.



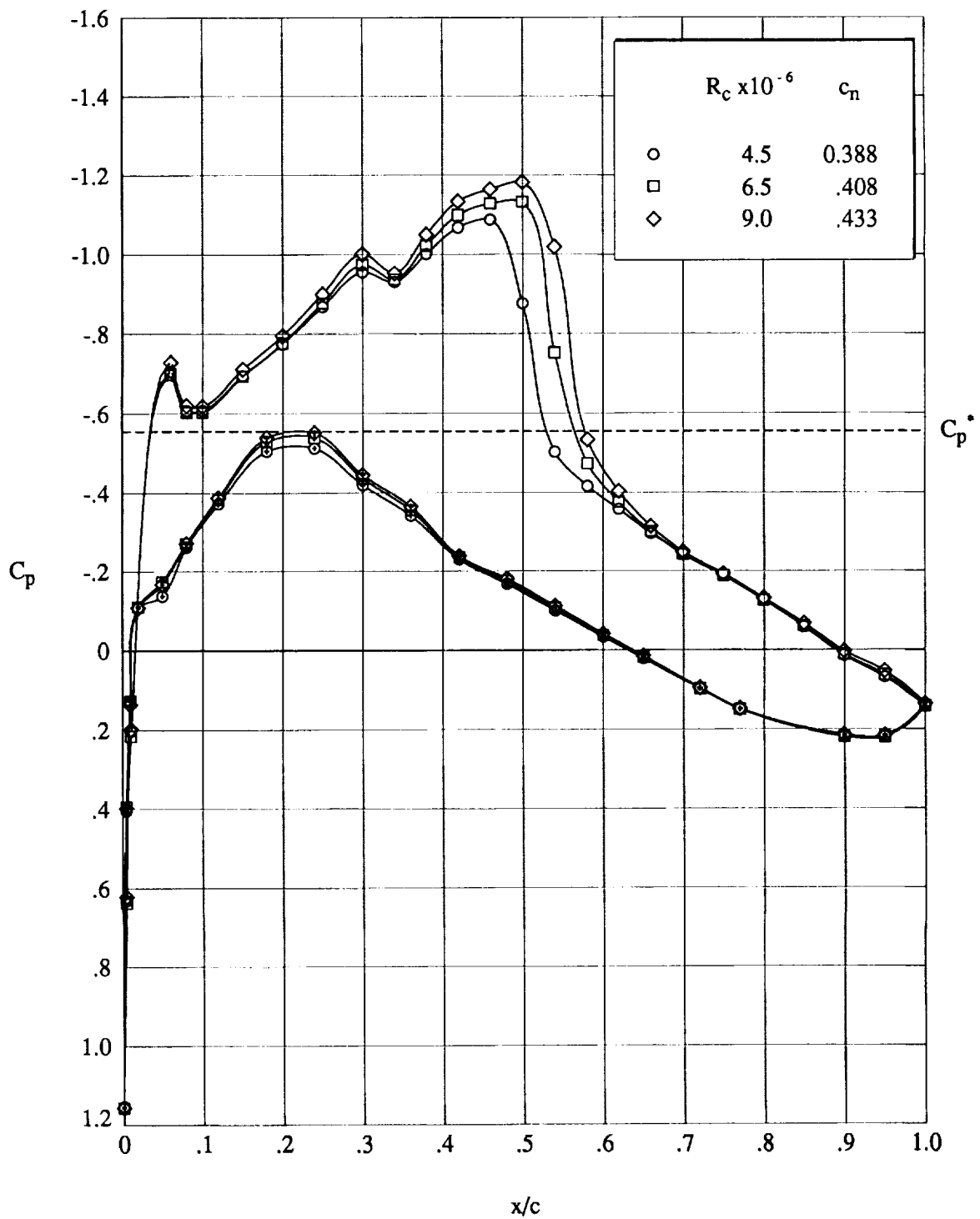
(a) $\alpha = -2.1^\circ$; $c_n \approx 0.05$.

Figure 15. Effect of Reynolds number at $M_\infty \approx 0.760$. Open symbols denote upper surface; "+" within symbol denotes lower surface.



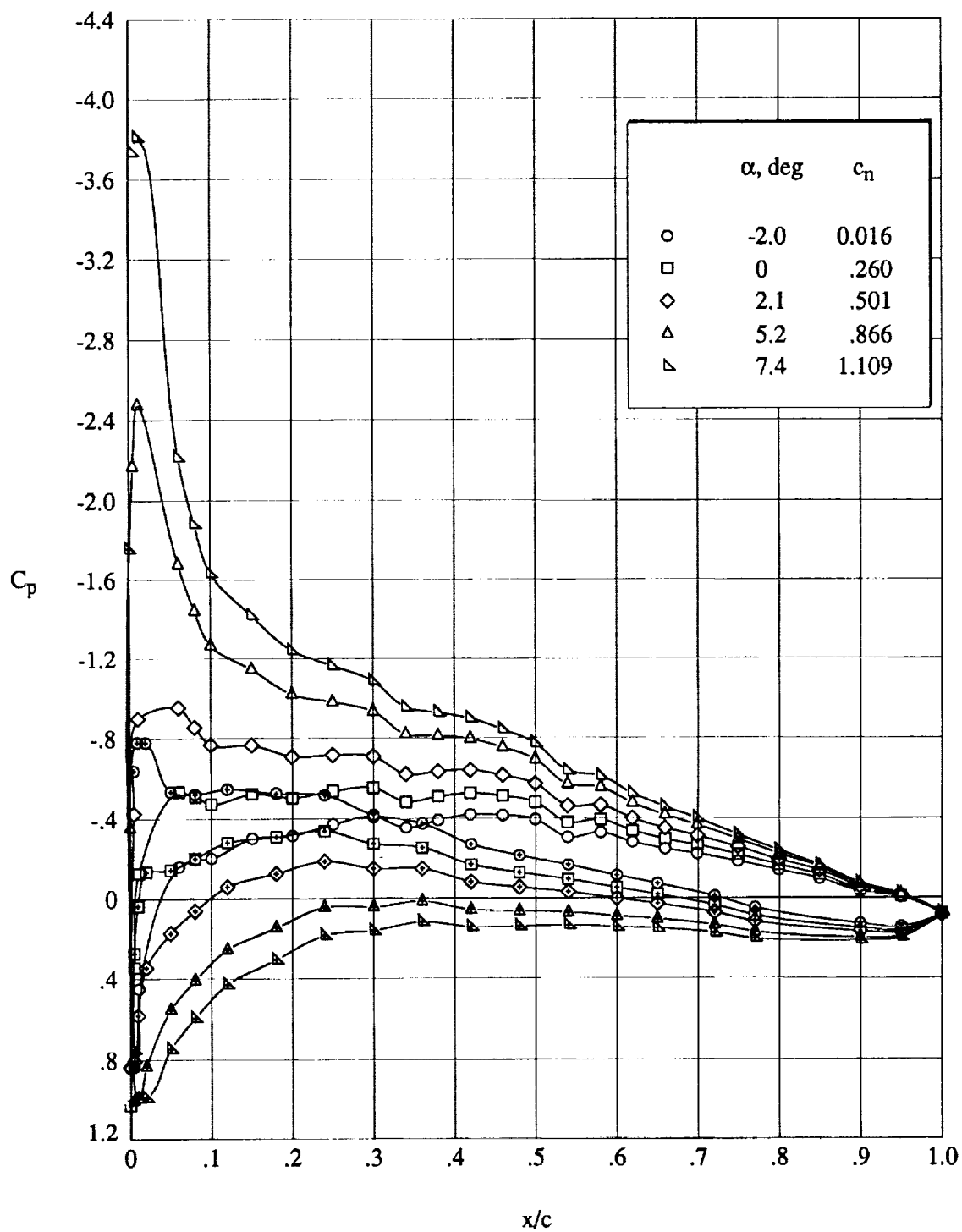
(b) $\alpha = -1.0^\circ$; $c_n \approx 0.2$.

Figure 15. Continued.



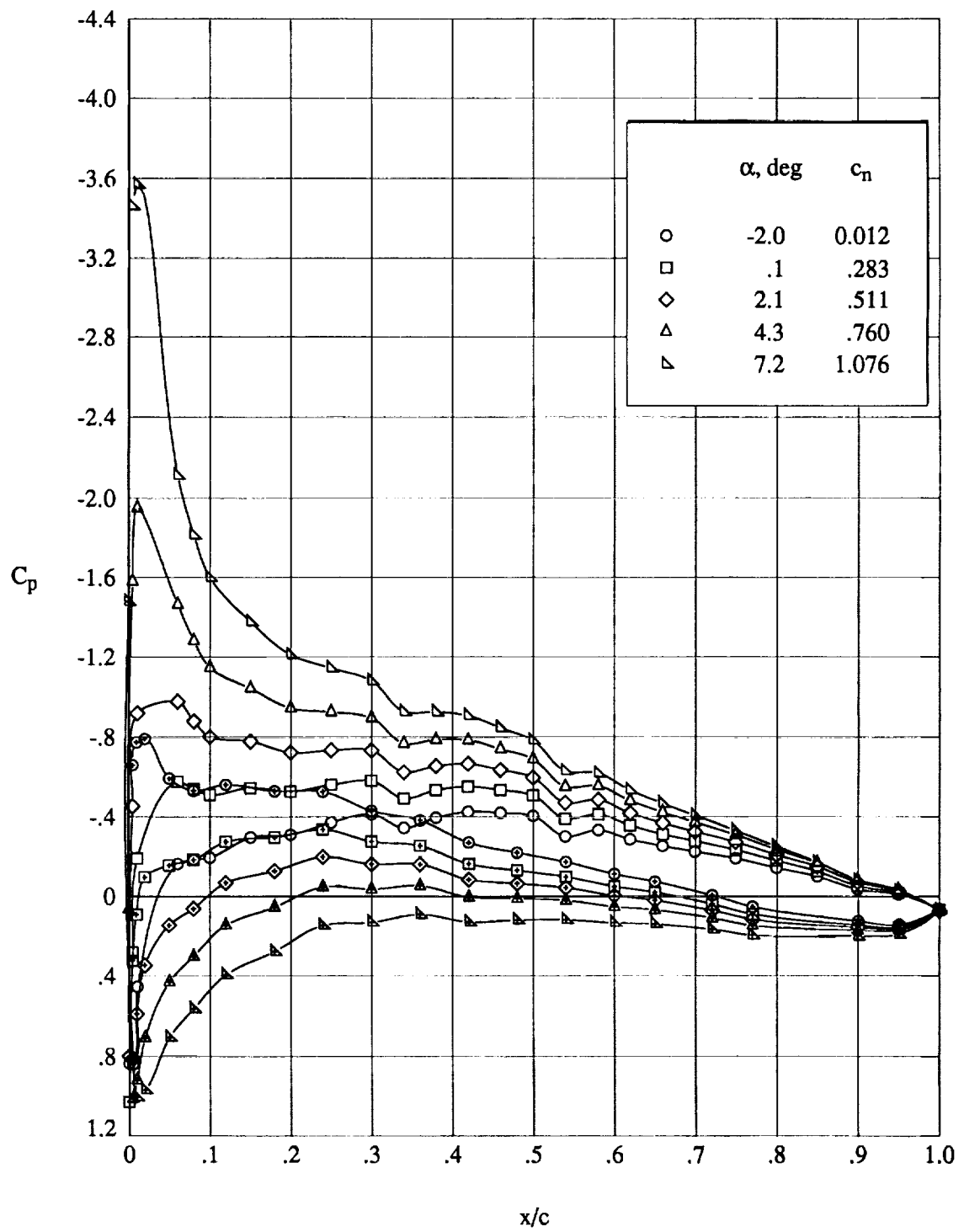
(c) $\alpha = 0^\circ$; $C_n \approx 0.4$.

Figure 15. Concluded.



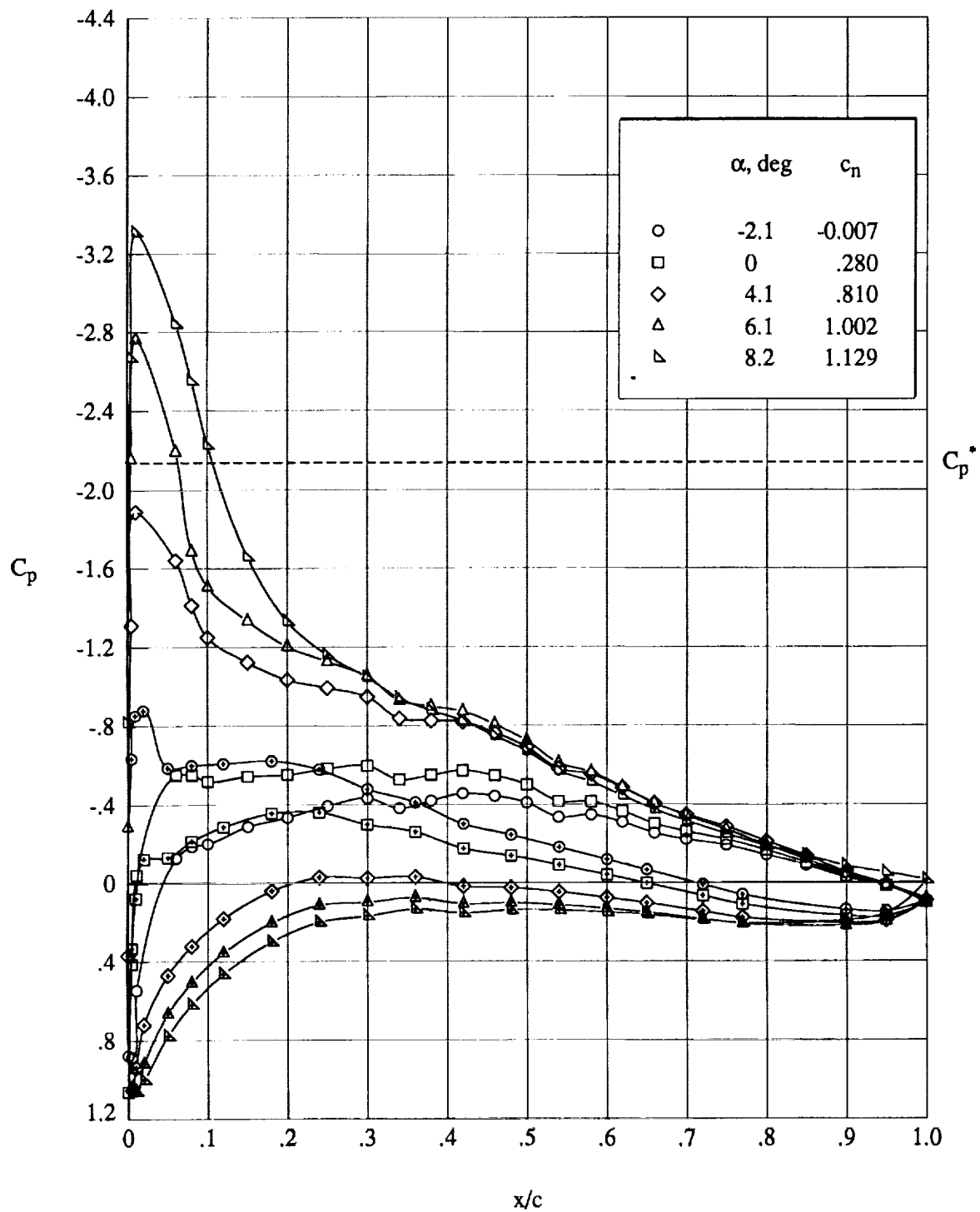
(a) $R_c = 4.5 \times 10^6$.

Figure 16. Effect of angle of attack at $M_\infty \approx 0.250$. Open symbols denote upper surface; “+” within symbol denotes lower surface.



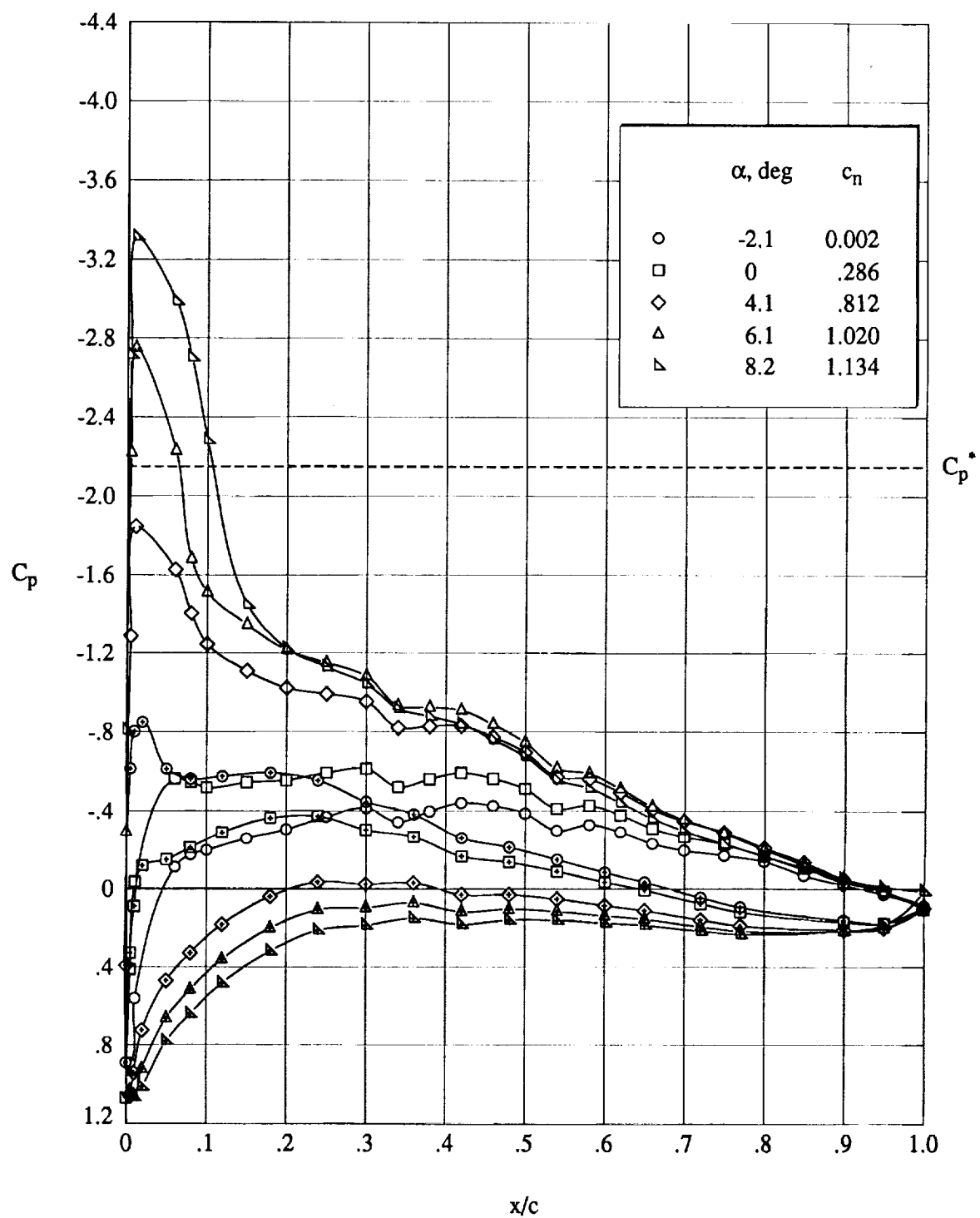
(b) $R_c = 9.0 \times 10^6$.

Figure 16. Concluded.



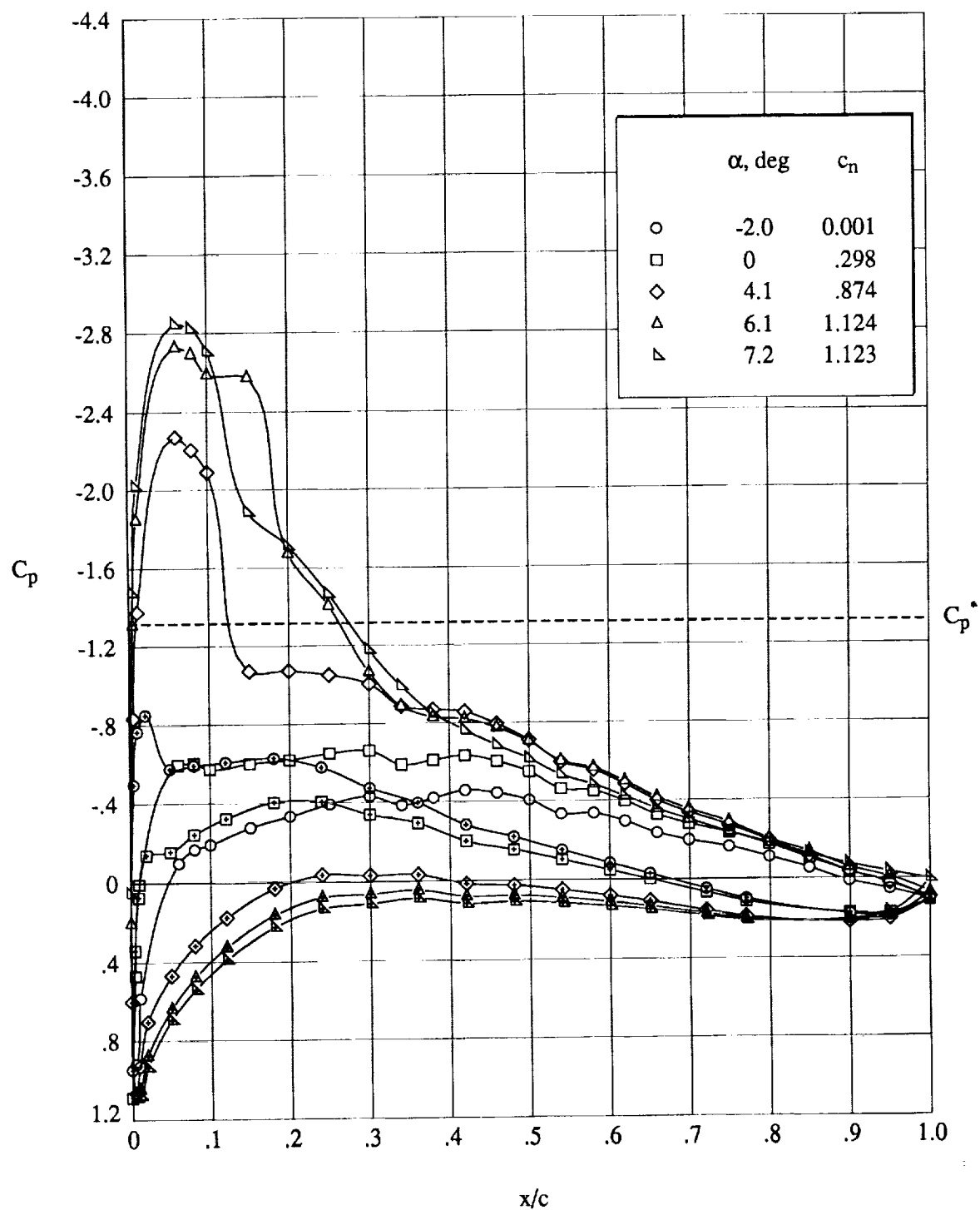
(a) $R_c = 4.5 \times 10^6$.

Figure 17. Effect of angle of attack at $M_\infty \approx 0.500$. Open symbols denote upper surface; "+" within symbol denotes lower surface.



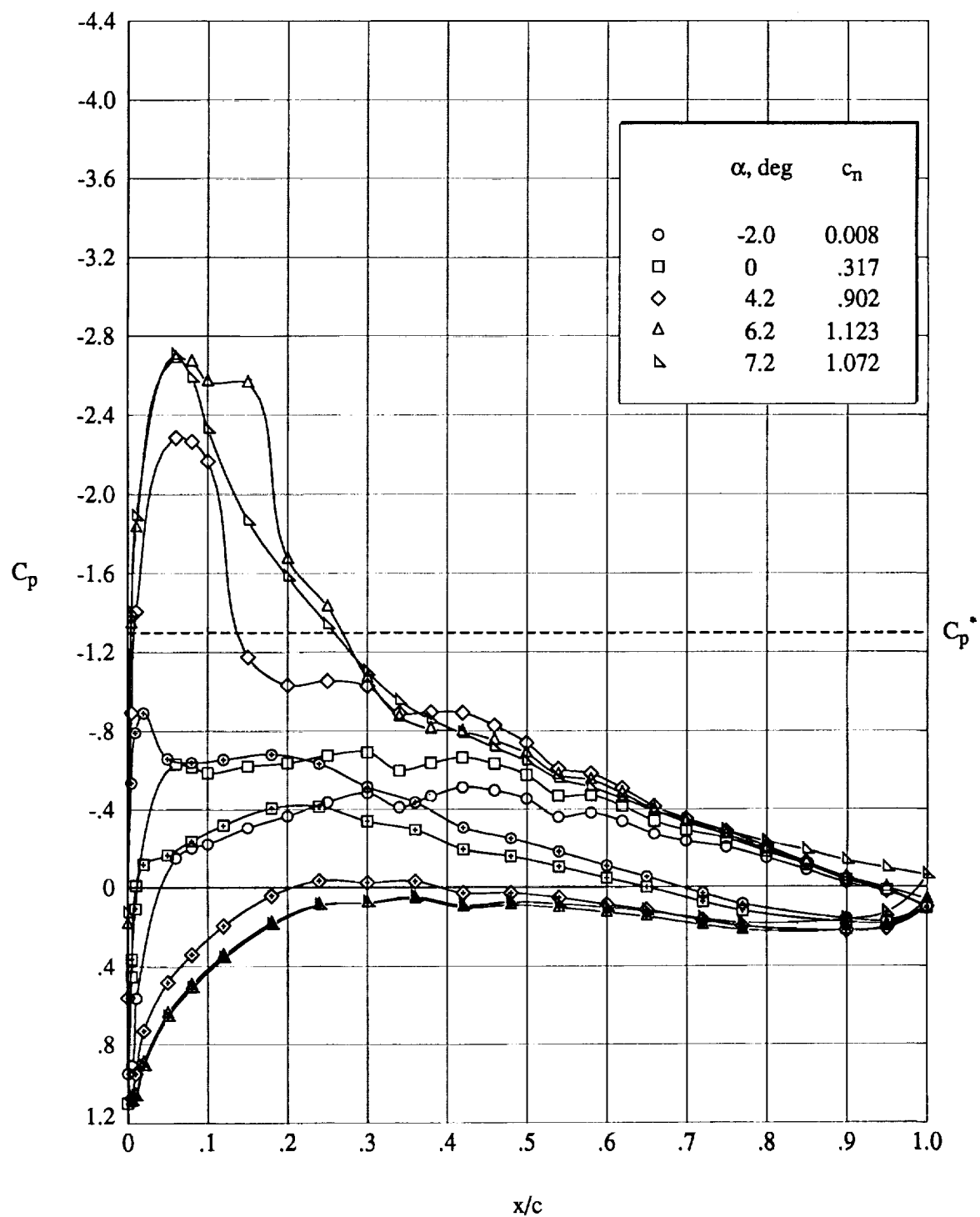
(b) $R_c = 9.0 \times 10^6$.

Figure 17. Concluded.



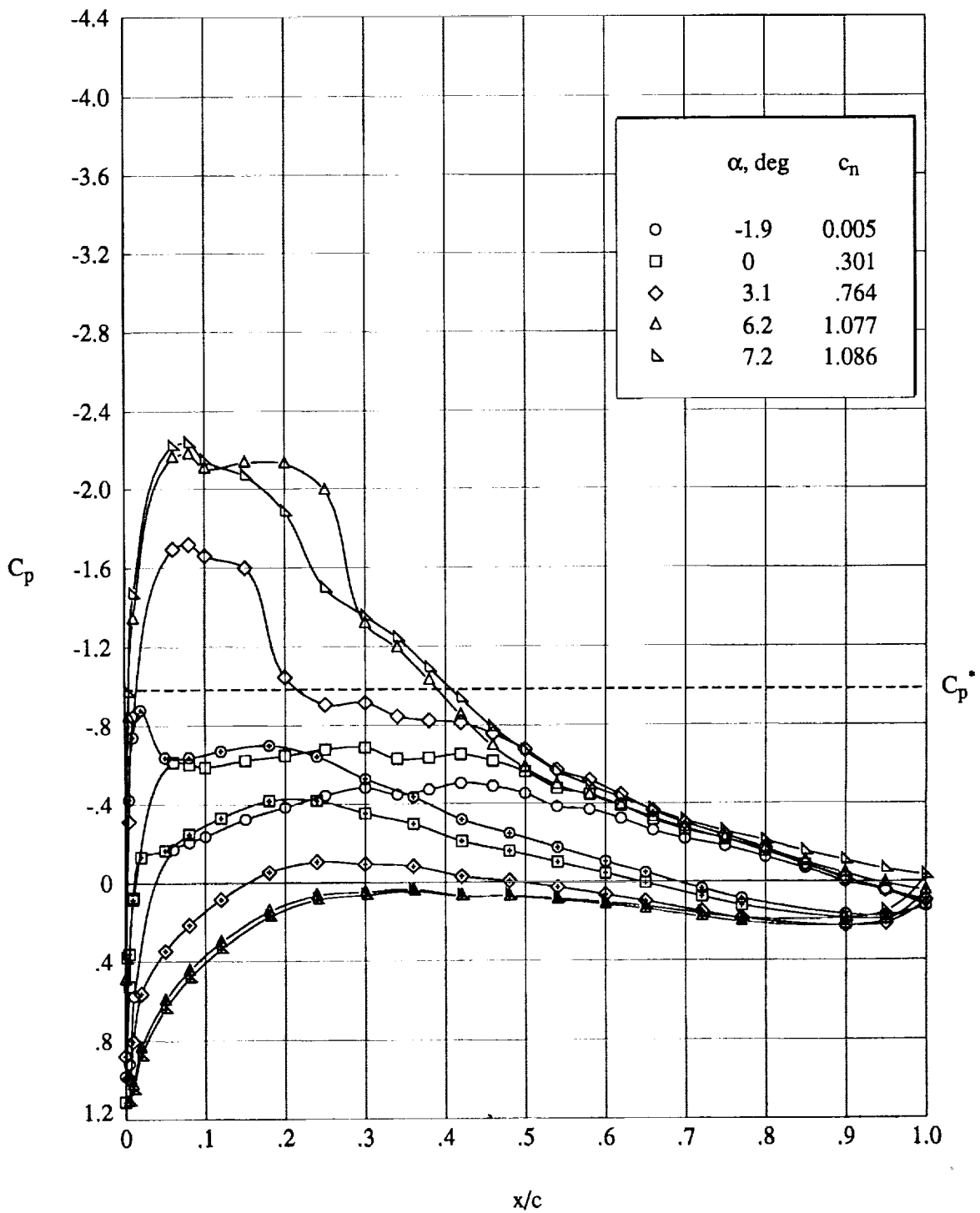
(a) $R_c = 4.5 \times 10^6$.

Figure 18. Effect of angle of attack at $M_\infty \approx 0.600$. Open symbols denote upper surface; "+" within symbol denotes lower surface.



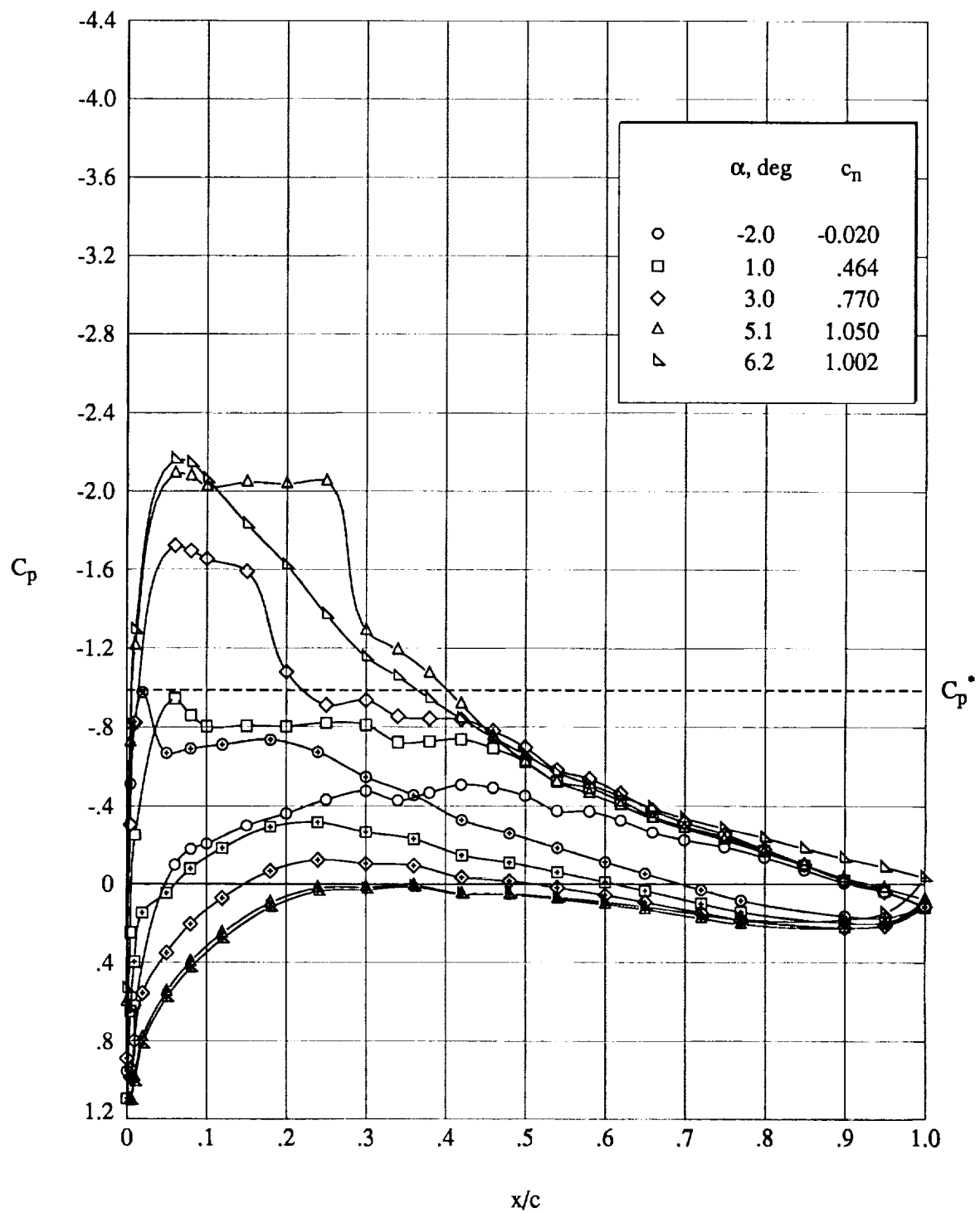
(b) $R_c = 9.0 \times 10^6$.

Figure 18. Concluded.



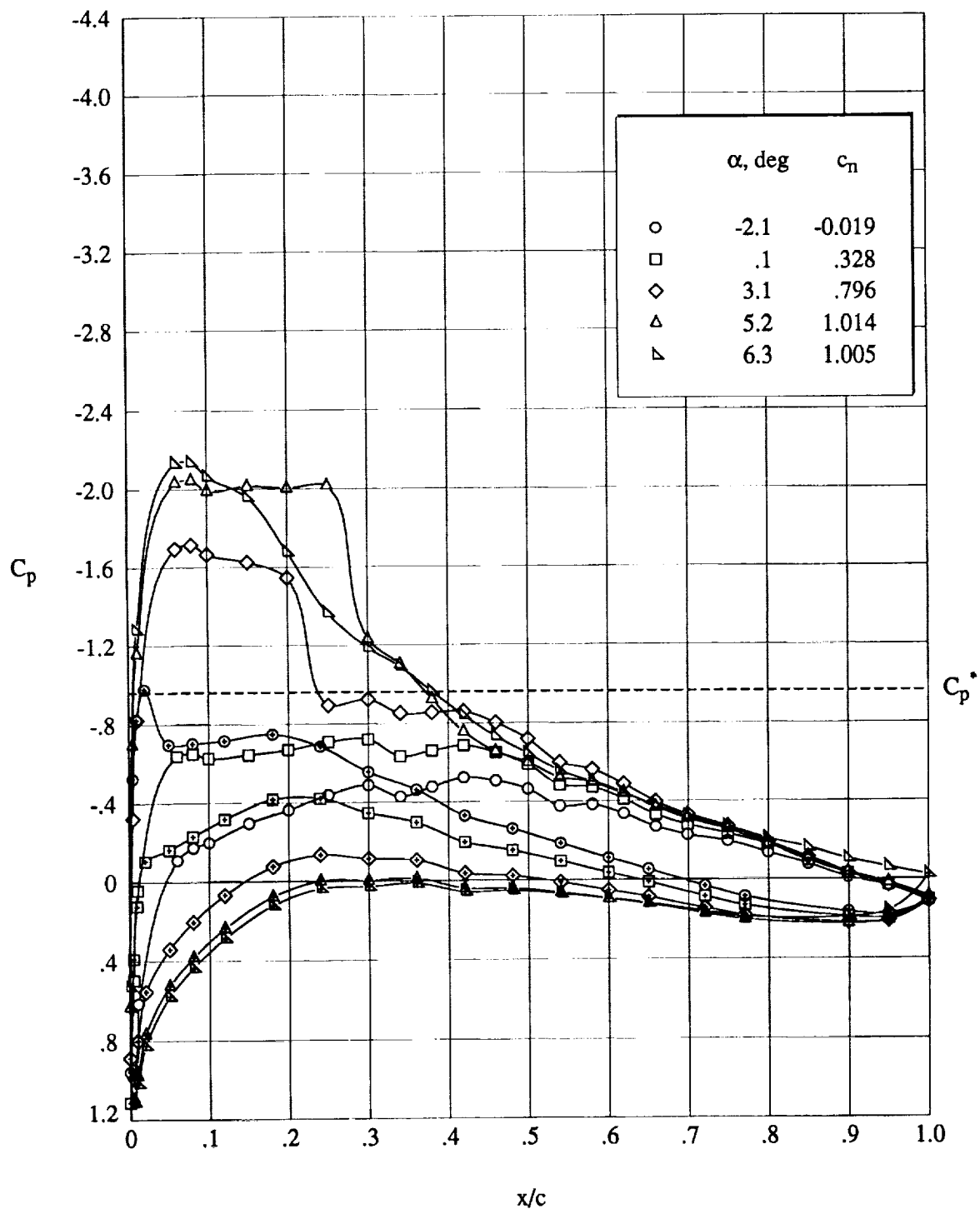
(a) $R_c = 3.0 \times 10^6$.

Figure 19. Effect of angle of attack at $M_\infty \approx 0.655$. Open symbols denote upper surface; "+" within symbol denotes lower surface.



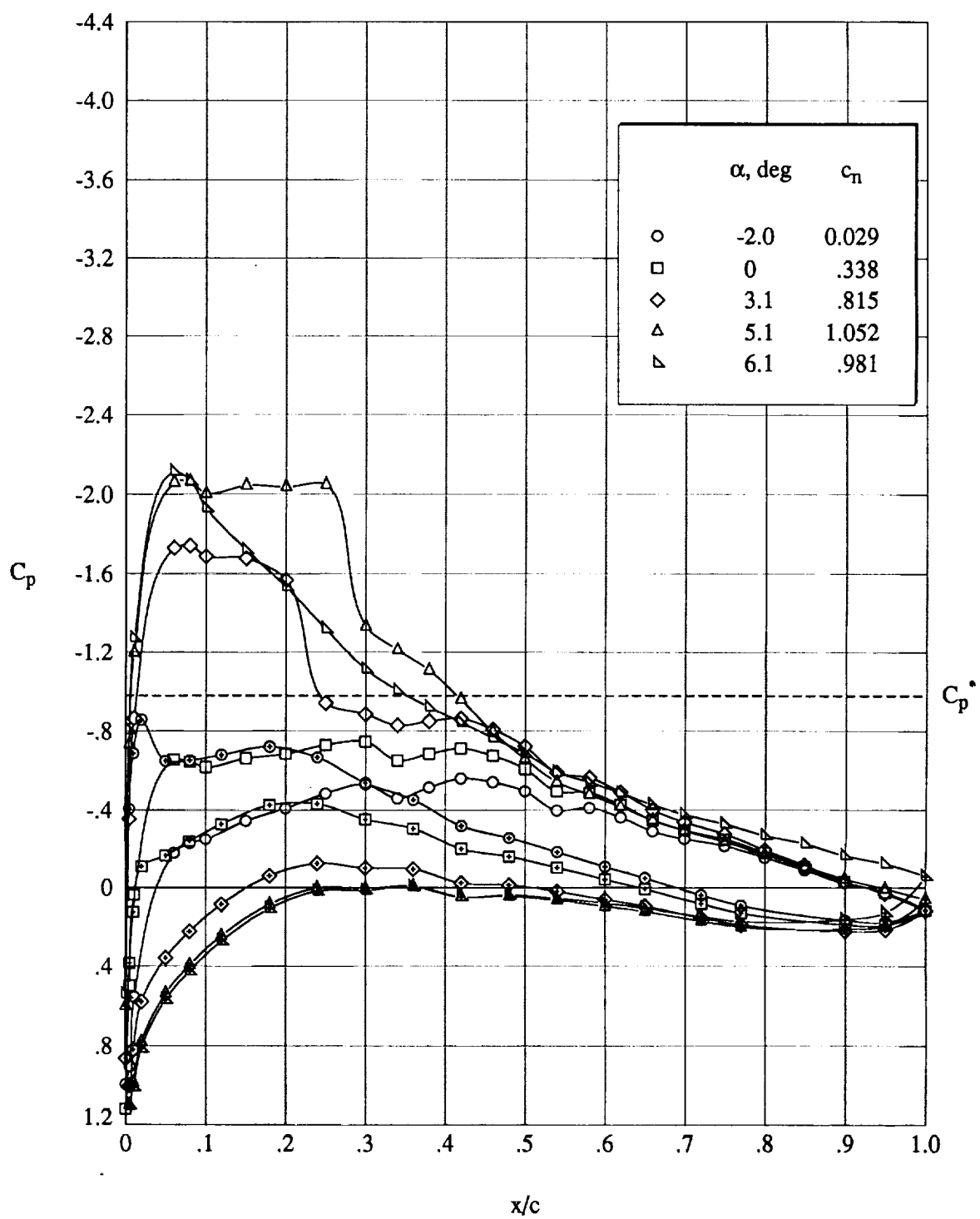
(b) $R_c = 4.5 \times 10^6$.

Figure 19. Continued.



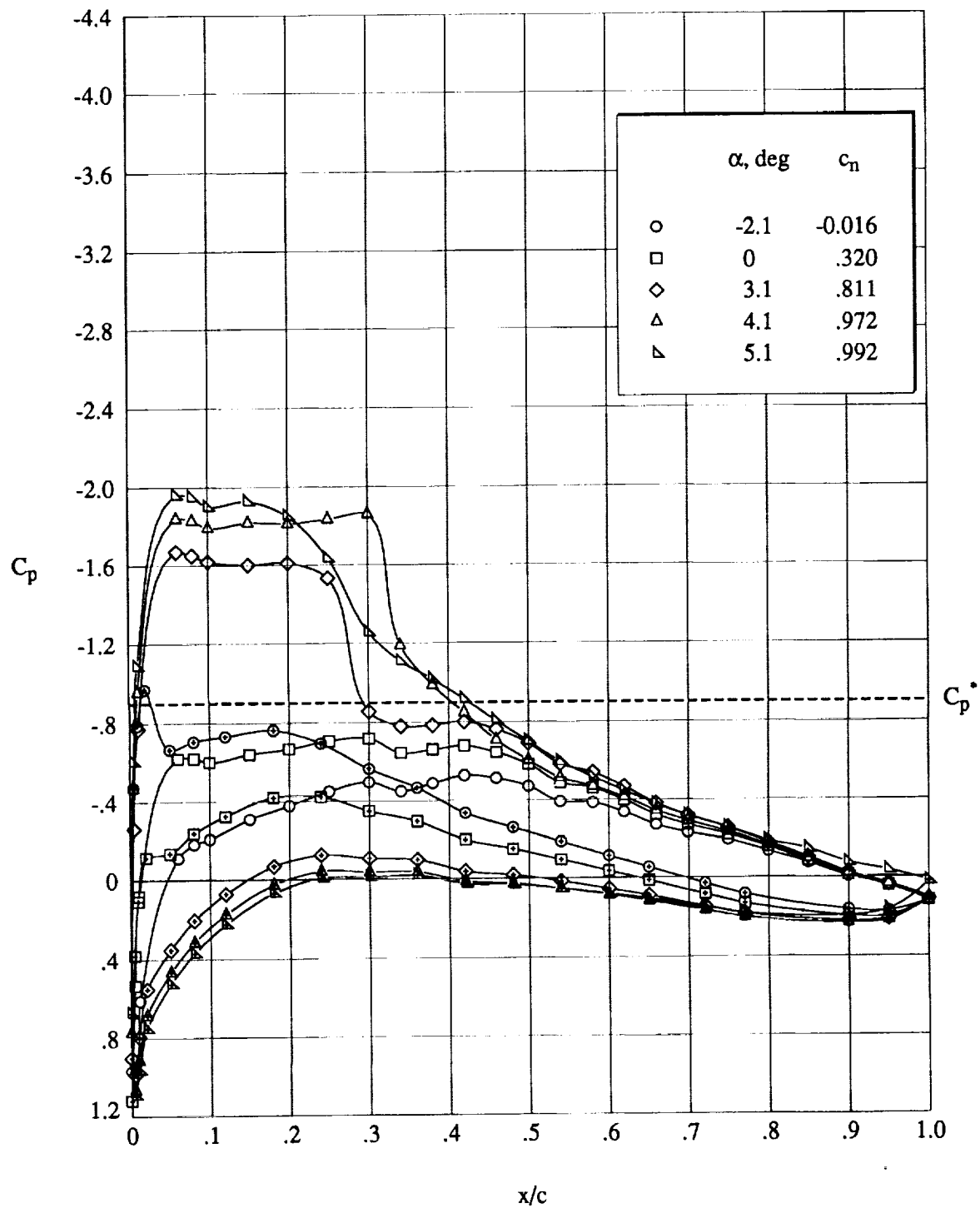
(c) $R_c = 6.5 \times 10^6$.

Figure 19. Continued.



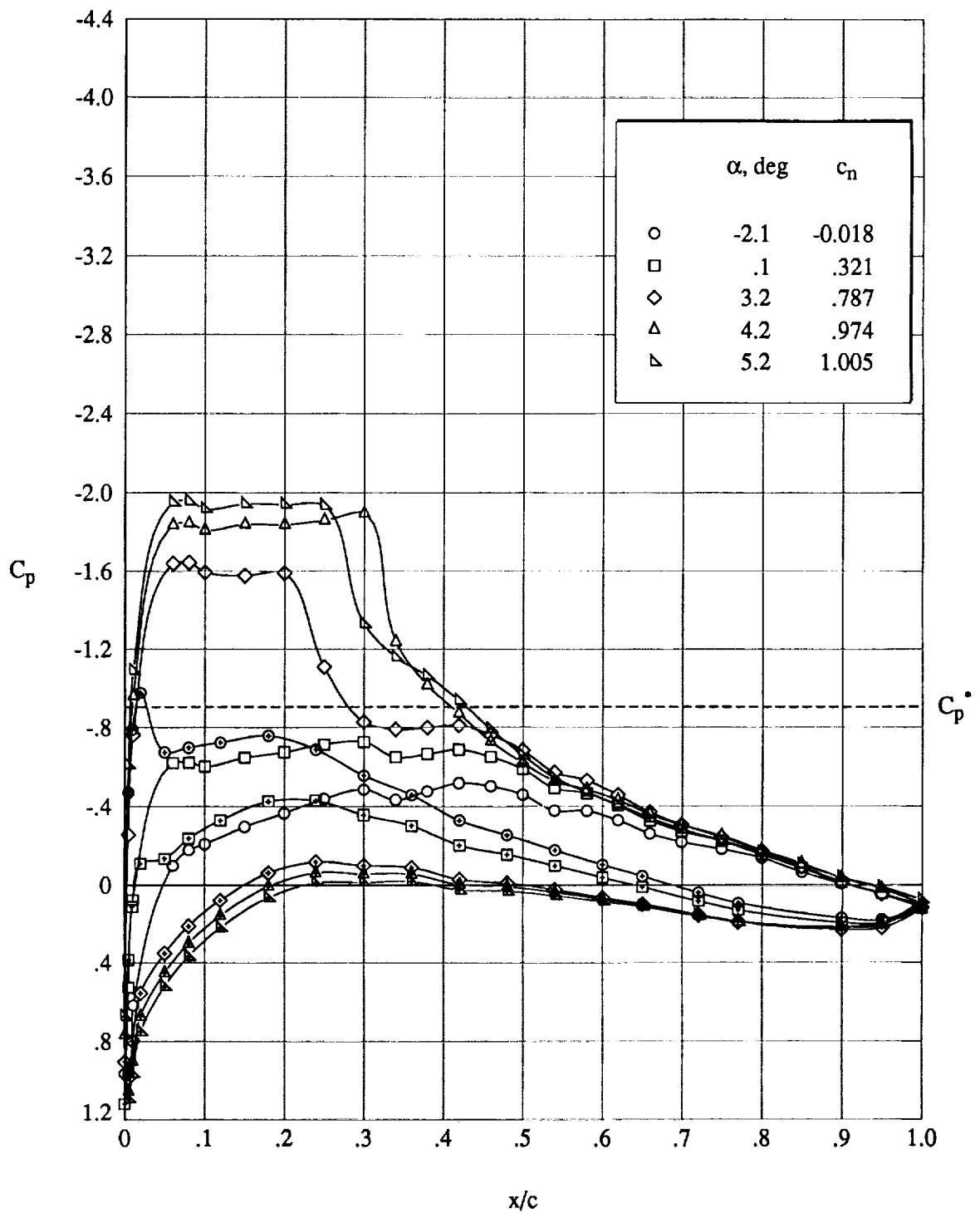
(d) $R_c = 9.0 \times 10^6$.

Figure 19. Concluded.



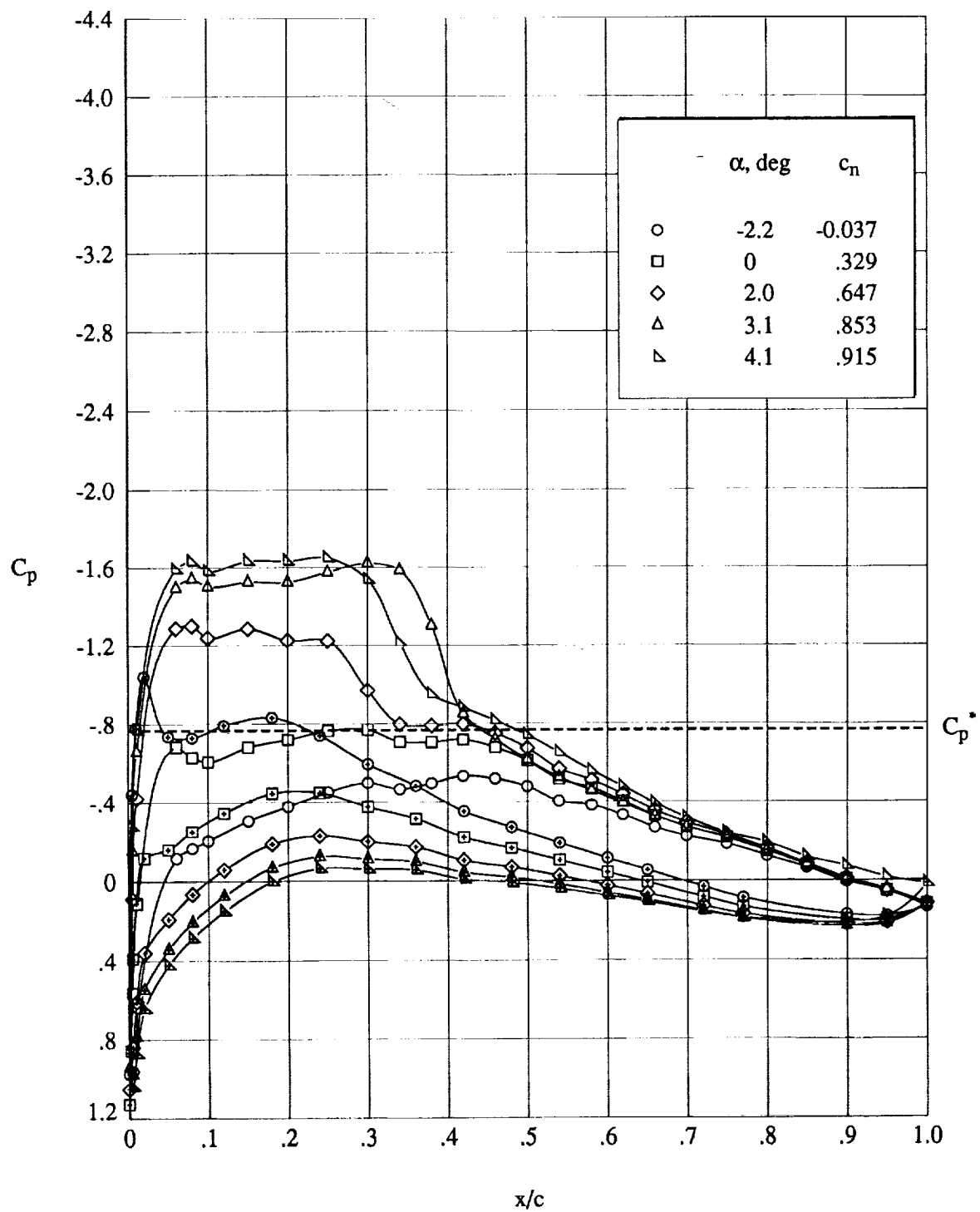
(a) $R_c = 4.5 \times 10^6$.

Figure 20. Effect of angle of attack at $M_\infty \approx 0.670$. Open symbols denote upper surface; "+" within symbol denotes lower surface.



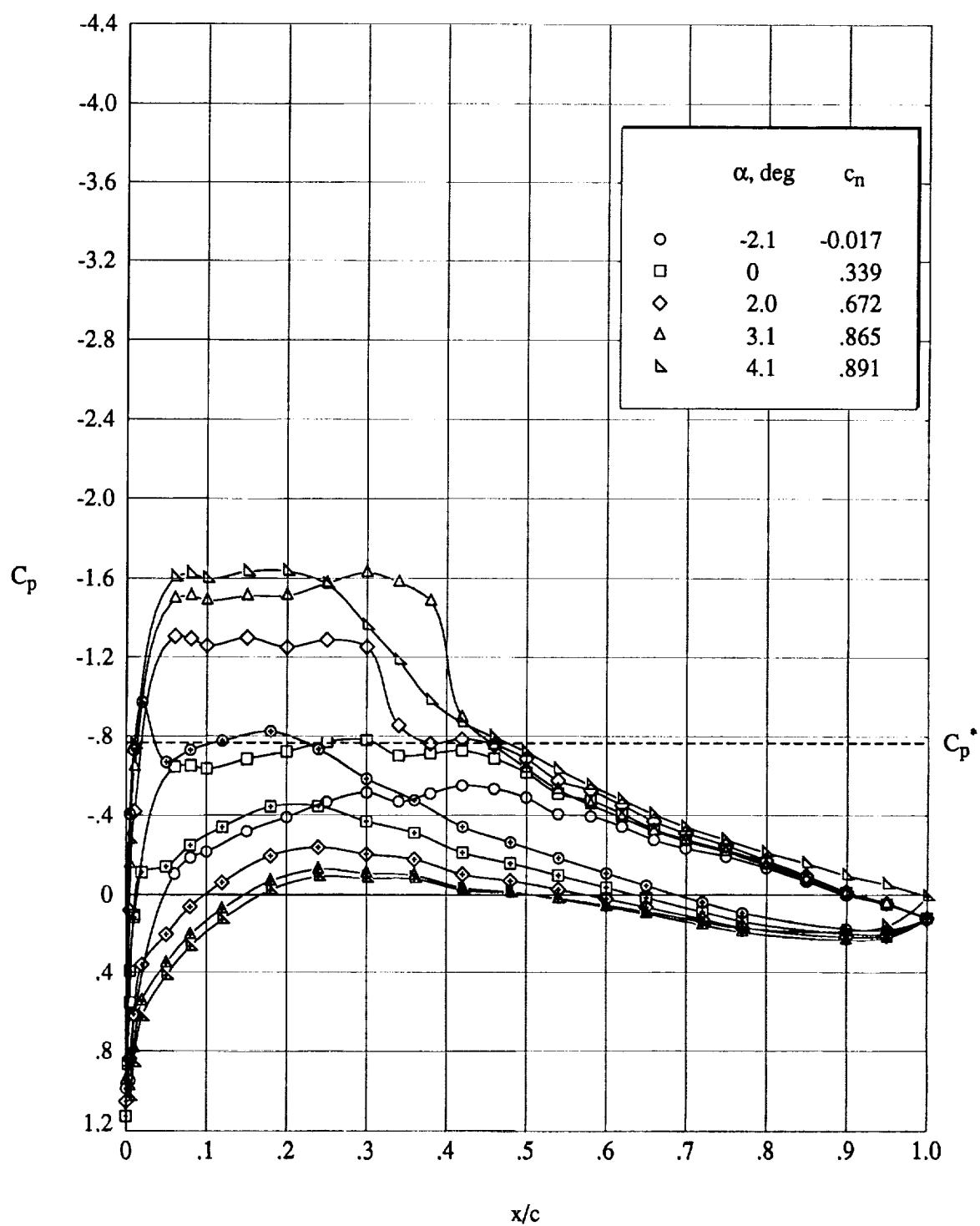
(b) $R_c = 5.0 \times 10^6$.

Figure 20. Concluded.



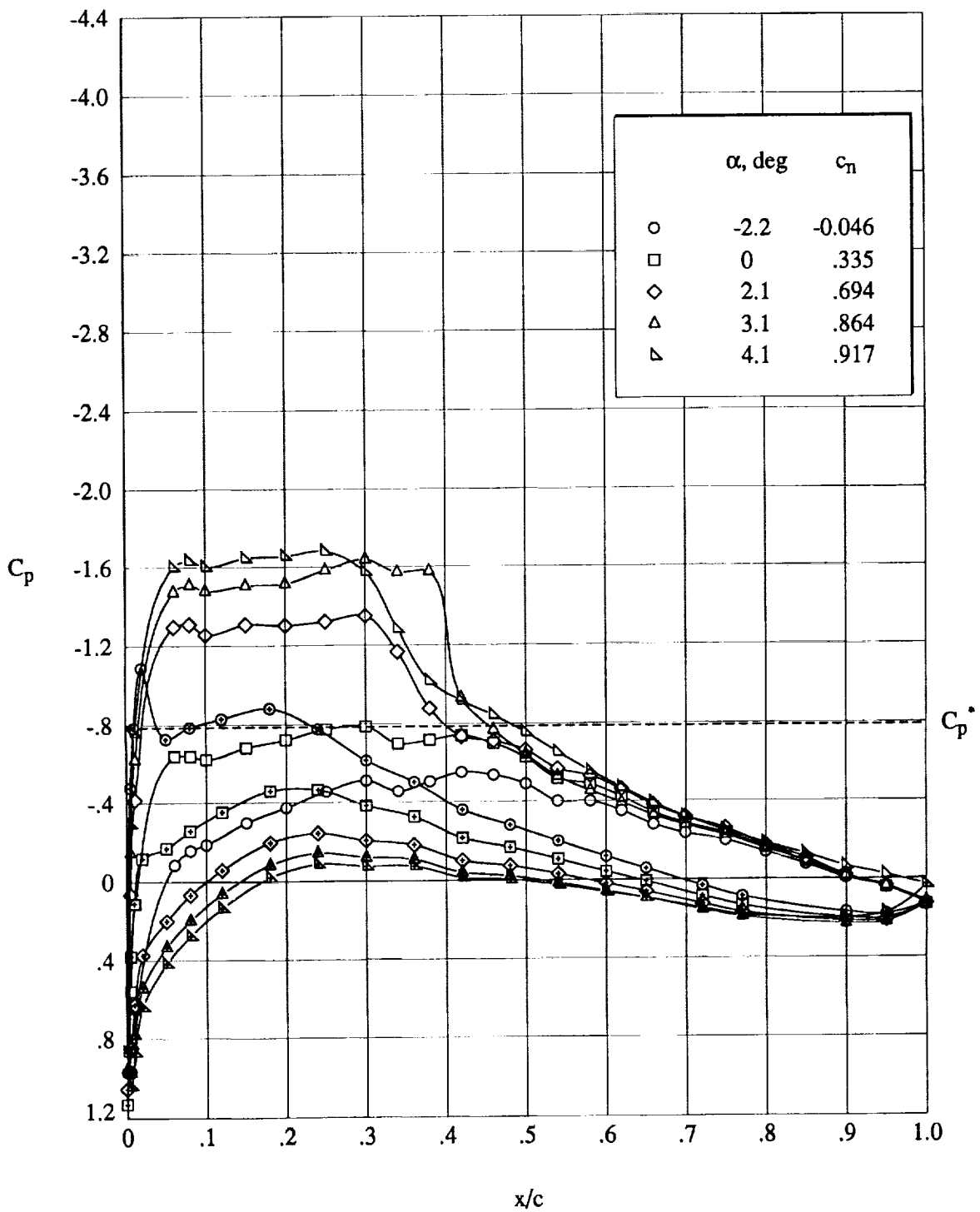
(a) $R_c = 3.0 \times 10^6$.

Figure 21. Effect of angle of attack at $M_\infty \approx 0.700$. Open symbols denote upper surface; "+" within symbol denotes lower surface.



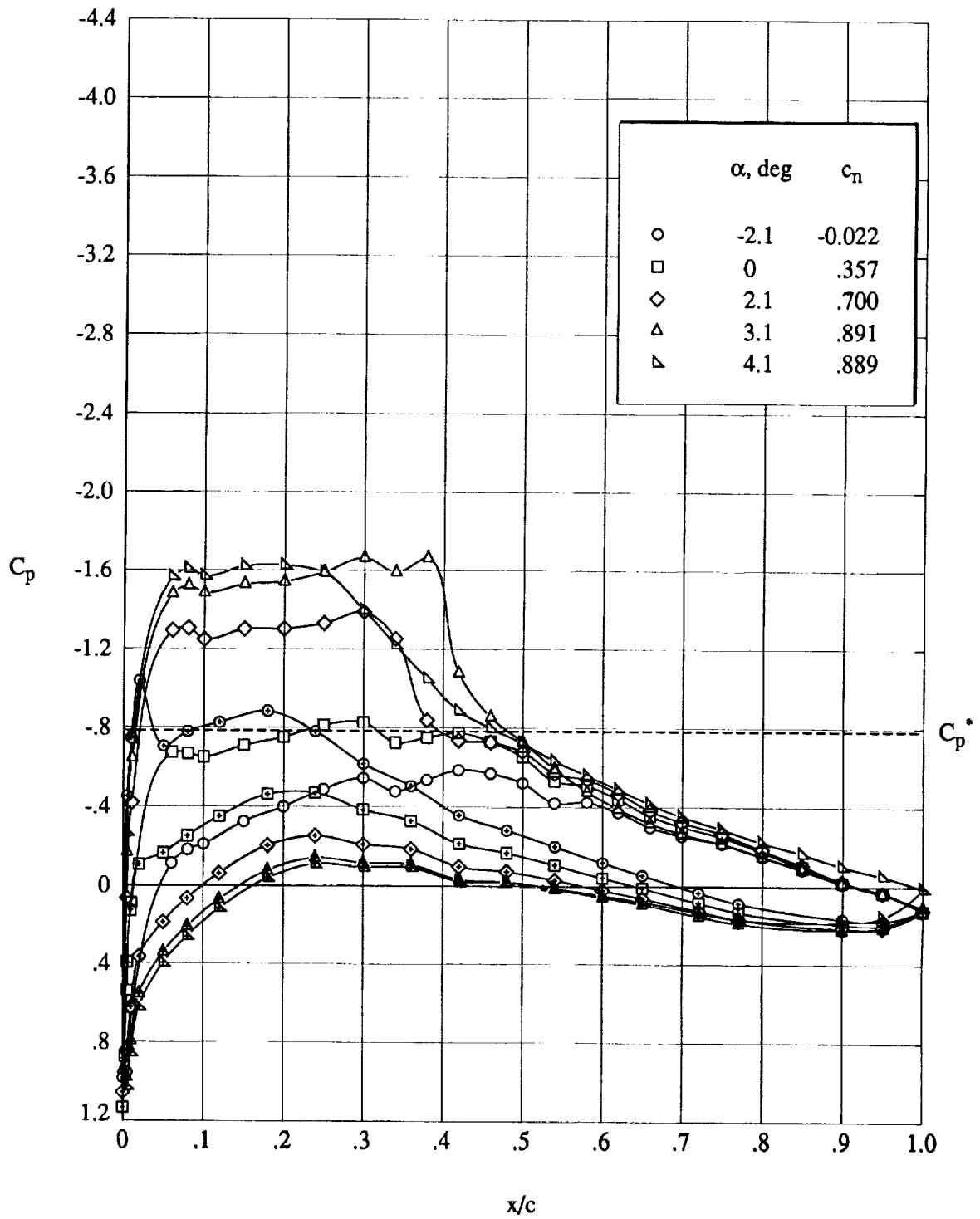
(b) $R_c = 4.5 \times 10^6$.

Figure 21. Continued.



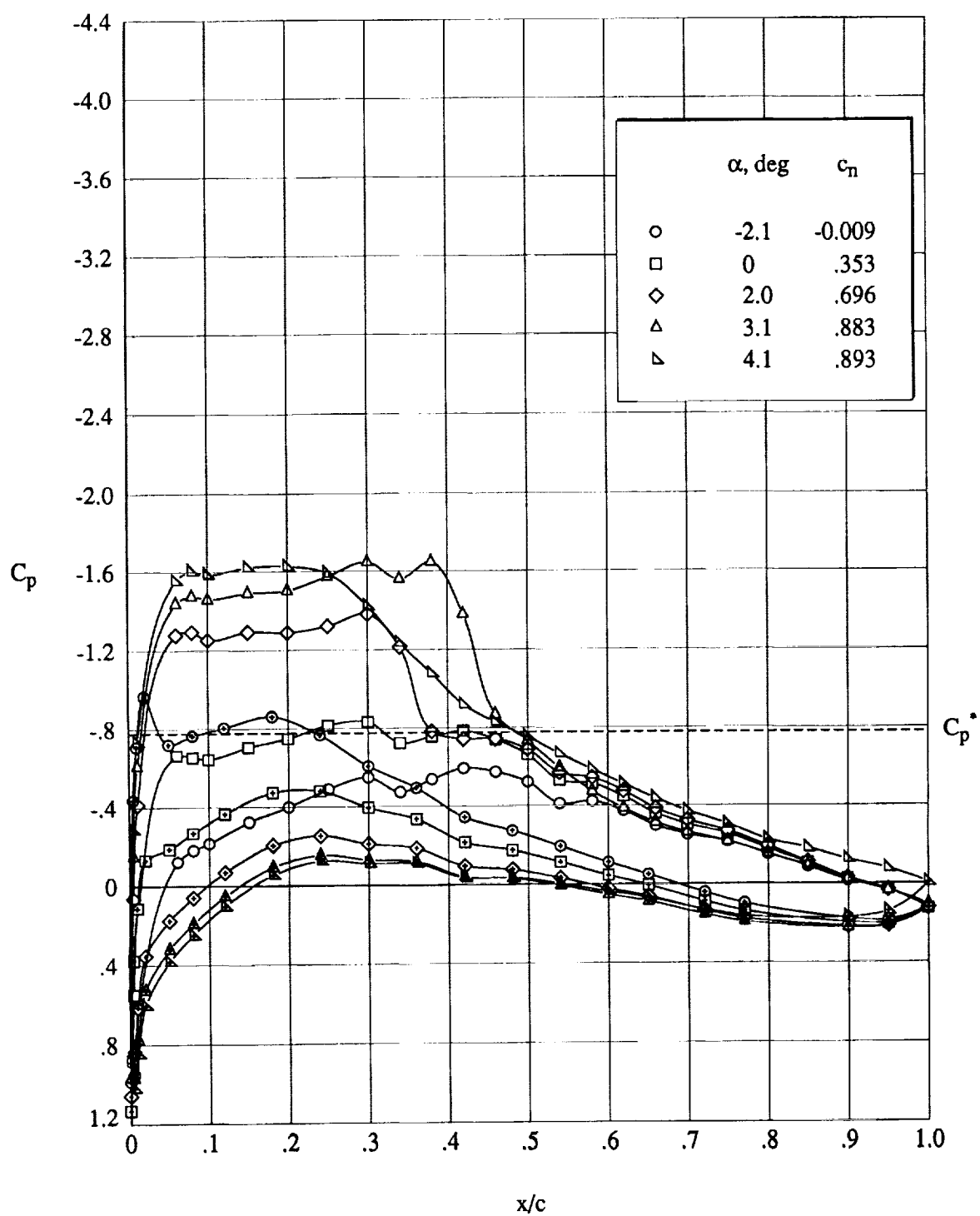
(c) $R_c = 6.5 \times 10^6$.

Figure 21. Continued.



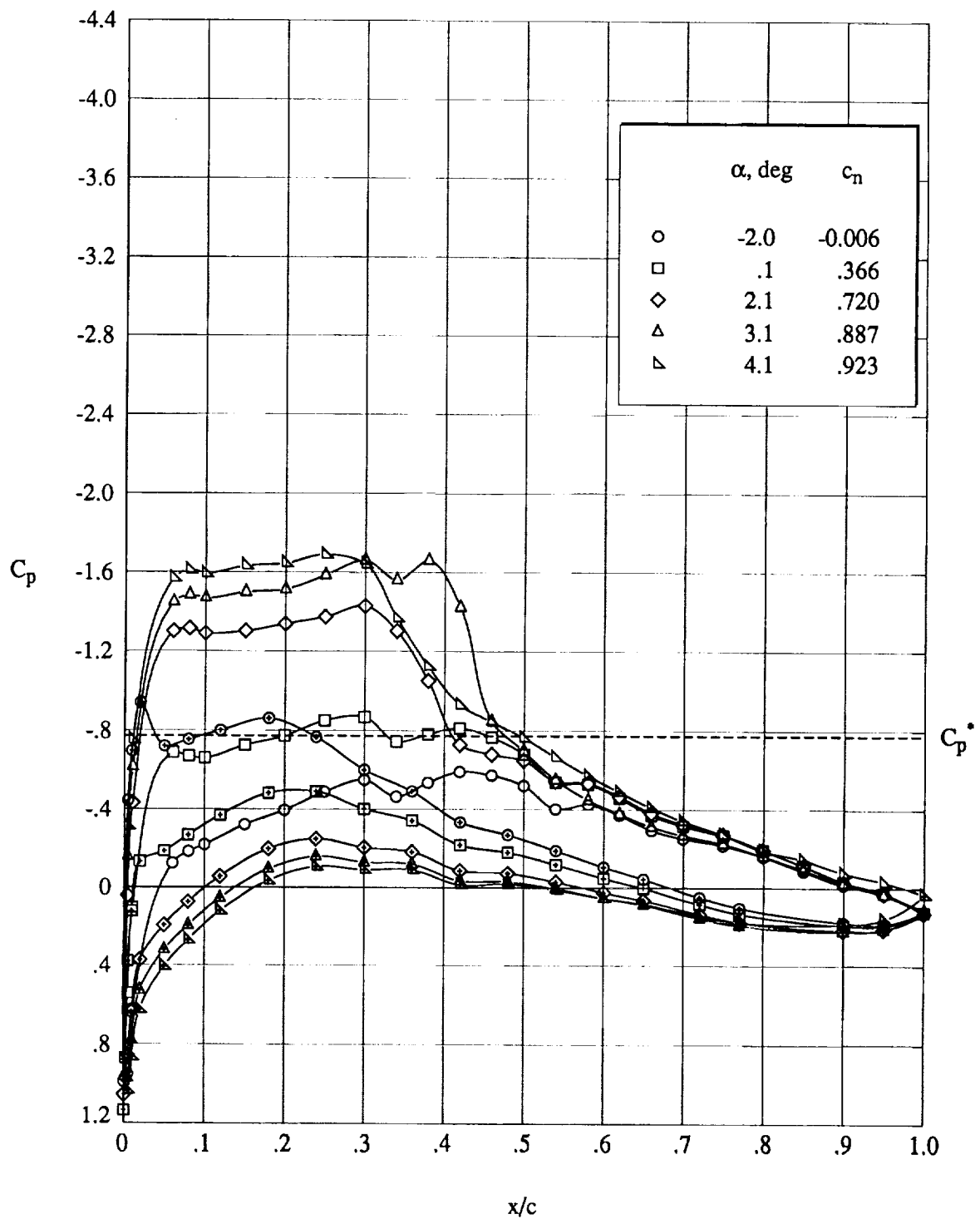
(d) $R_c = 9.0 \times 10^6$.

Figure 21. Continued.



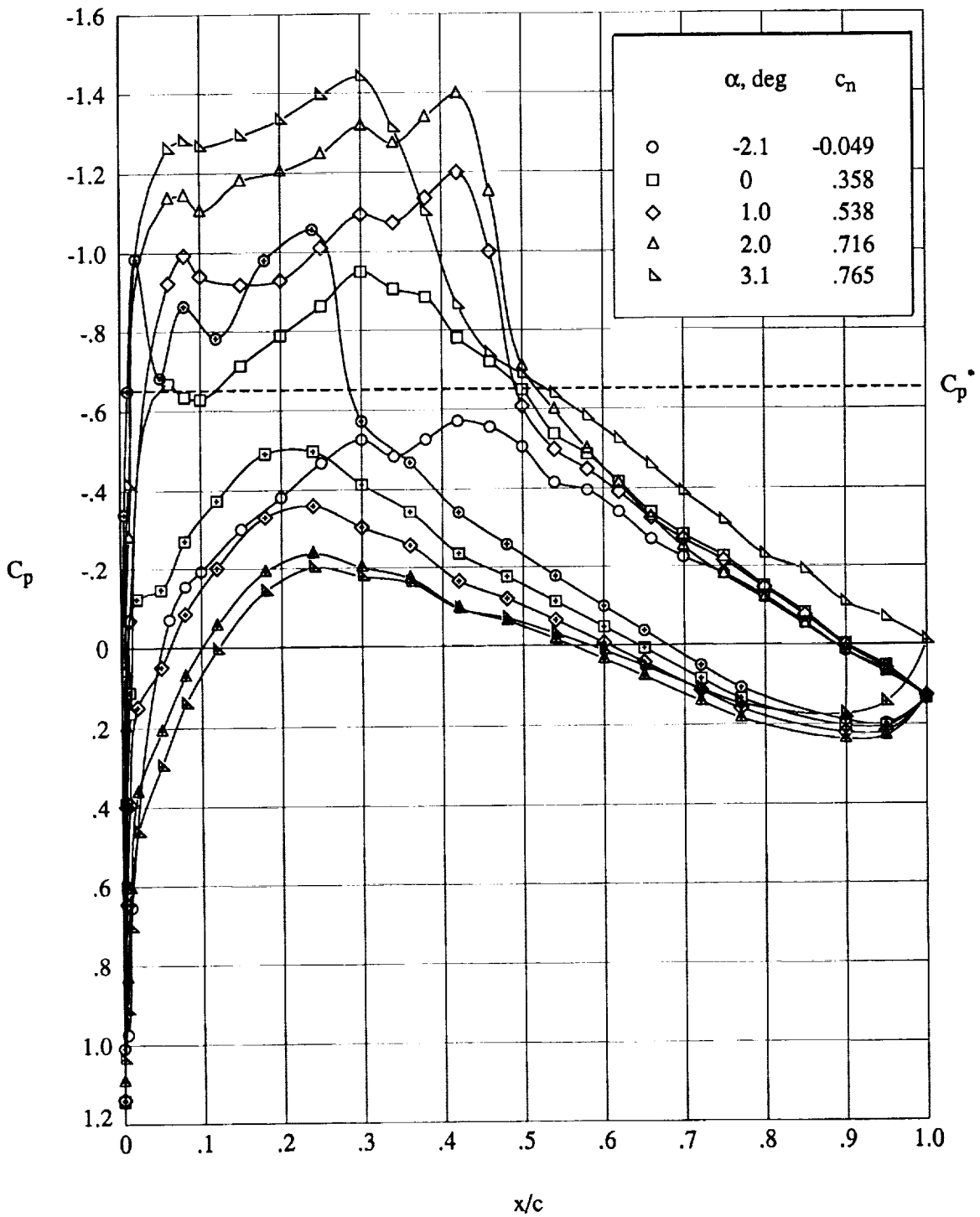
(e) $R_e = 13.5 \times 10^6$.

Figure 21. Continued.



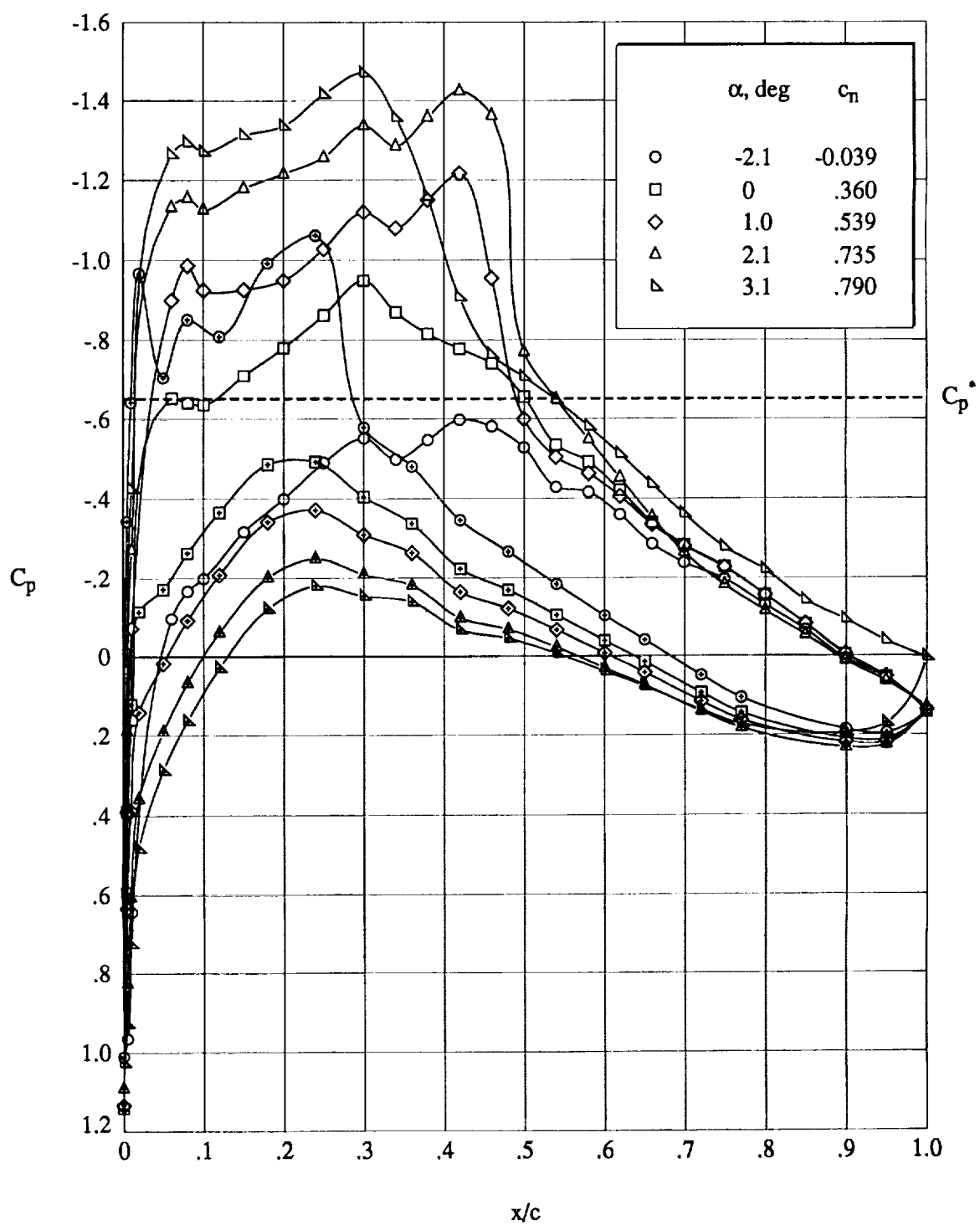
(f) $R_c = 18.0 \times 10^6$.

Figure 21. Concluded.



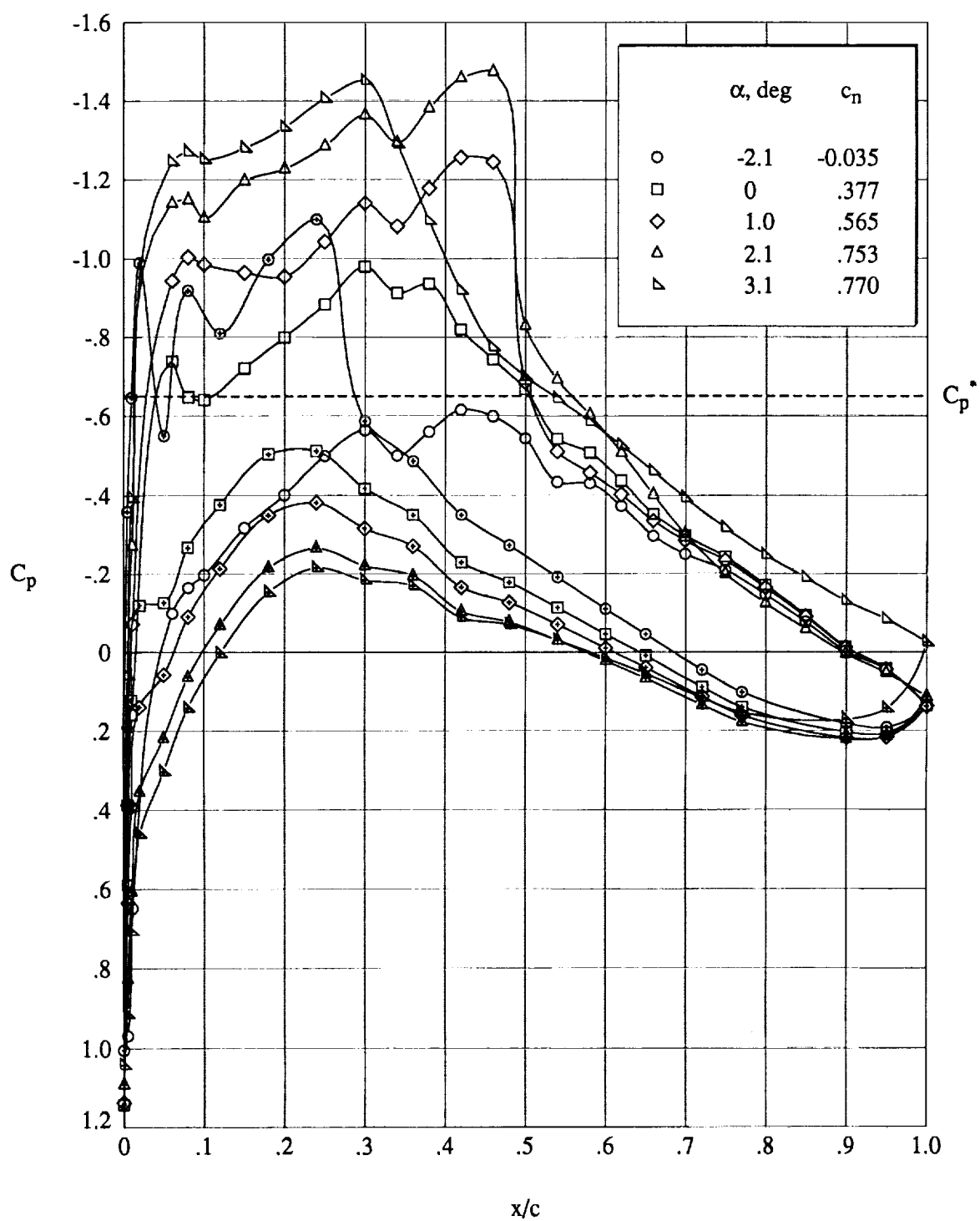
(a) $R_c = 4.5 \times 10^6$.

Figure 22. Effect of angle of attack at $M_\infty \approx 0.735$. Open symbols denote upper surface; "+" within symbol denotes lower surface.



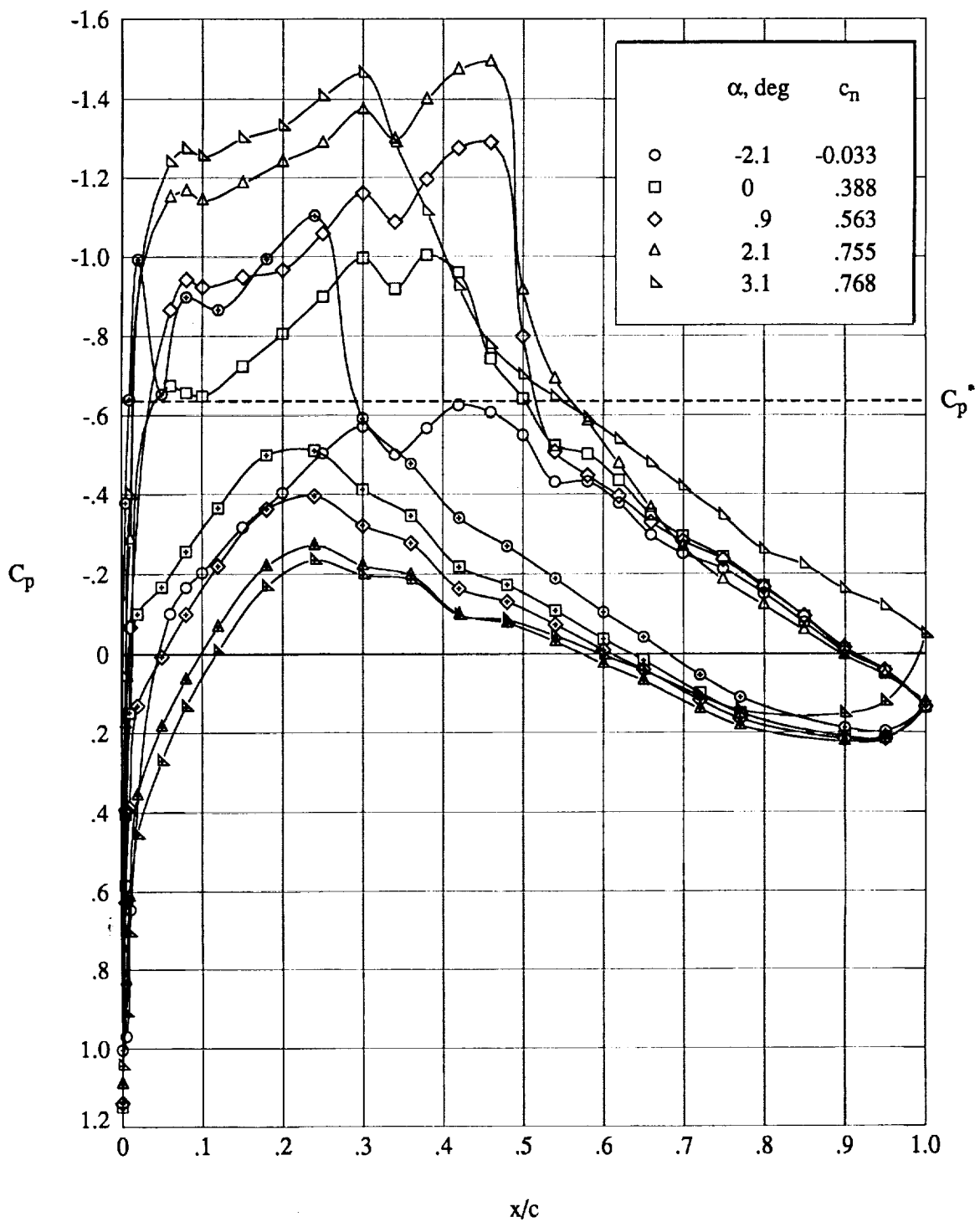
(b) $R_c = 6.5 \times 10^6$.

Figure 22. Continued.



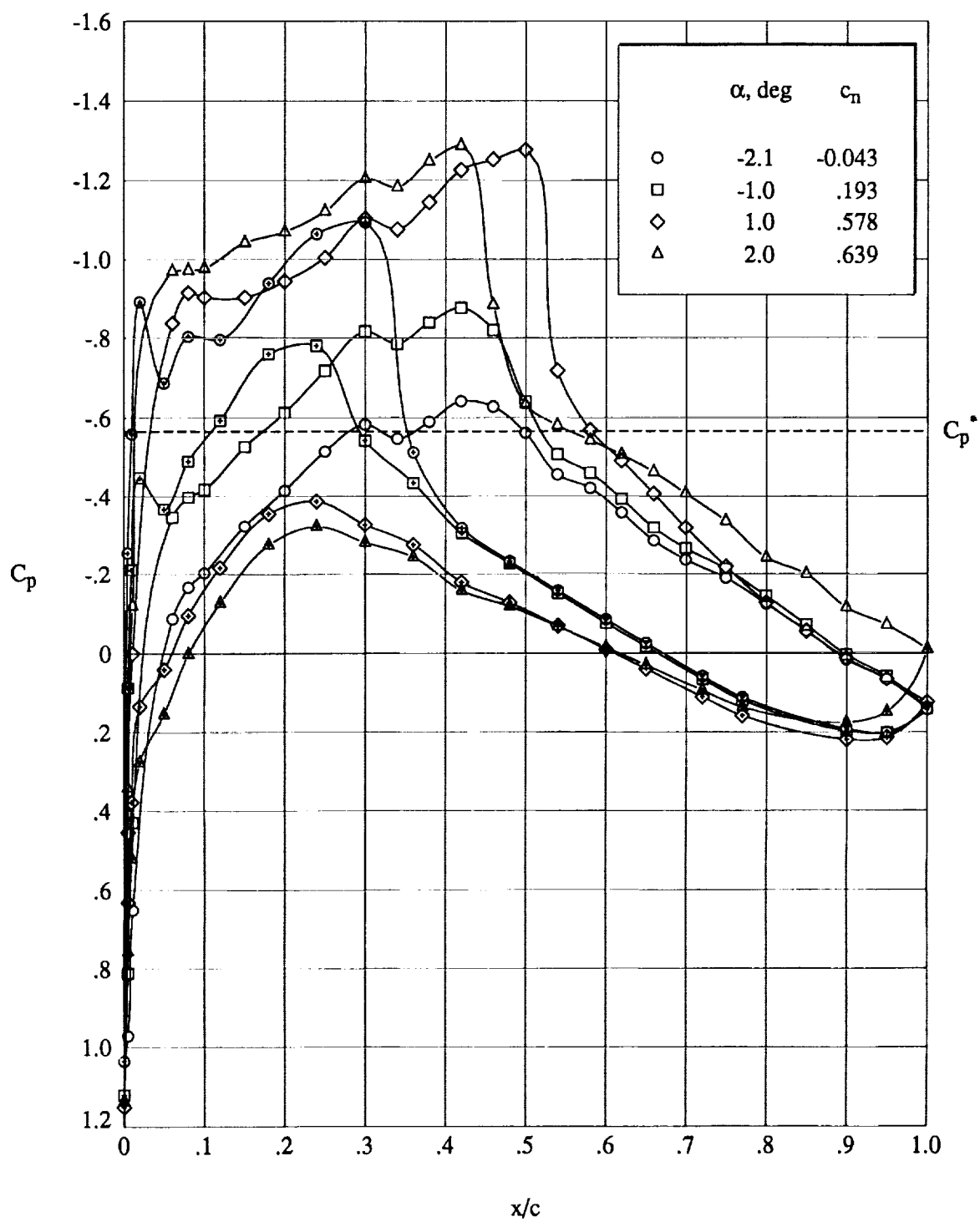
(c) $R_c = 9.0 \times 10^6$.

Figure 22. Continued.



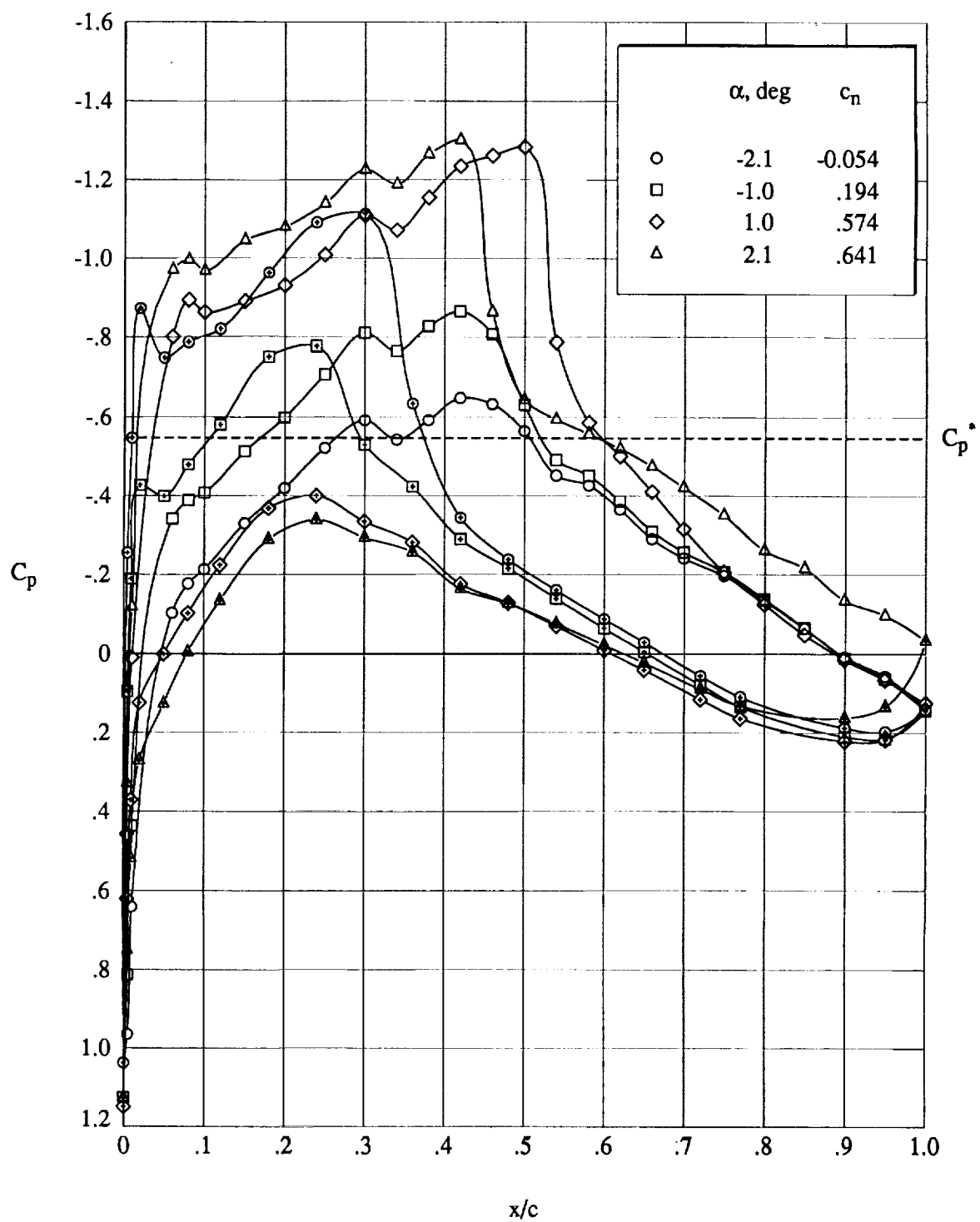
(d) $R_c = 13.5 \times 10^6$.

Figure 22. Concluded.



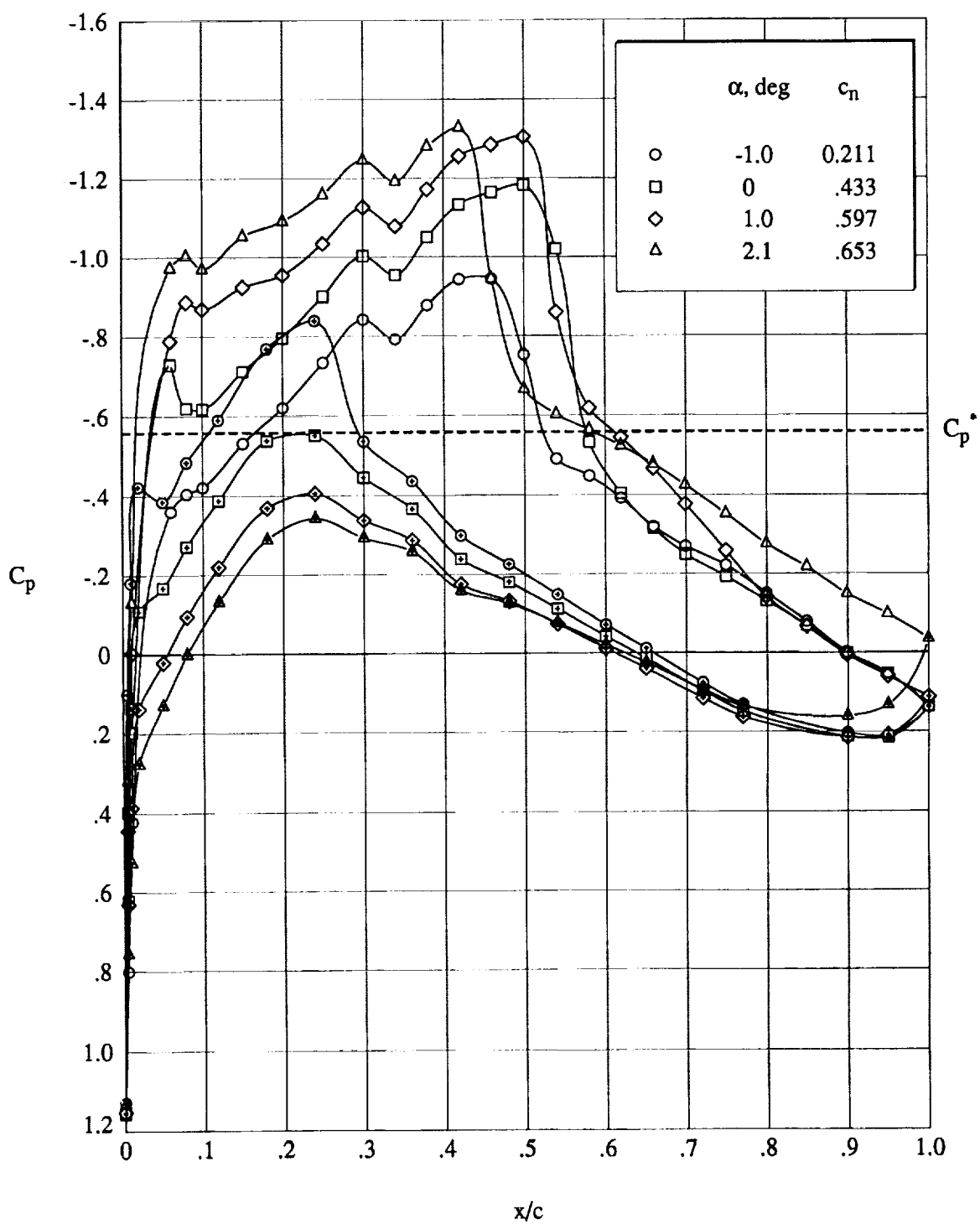
(a) $R_c = 4.5 \times 10^6$.

Figure 23. Effect of angle of attack at $M_\infty \approx 0.760$. Open symbols denote upper surface; “+” within symbol denotes lower surface.



(b) $R_c = 6.5 \times 10^6$.

Figure 23. Continued.



(c) $R_c = 9.0 \times 10^6$.

Figure 23. Concluded.

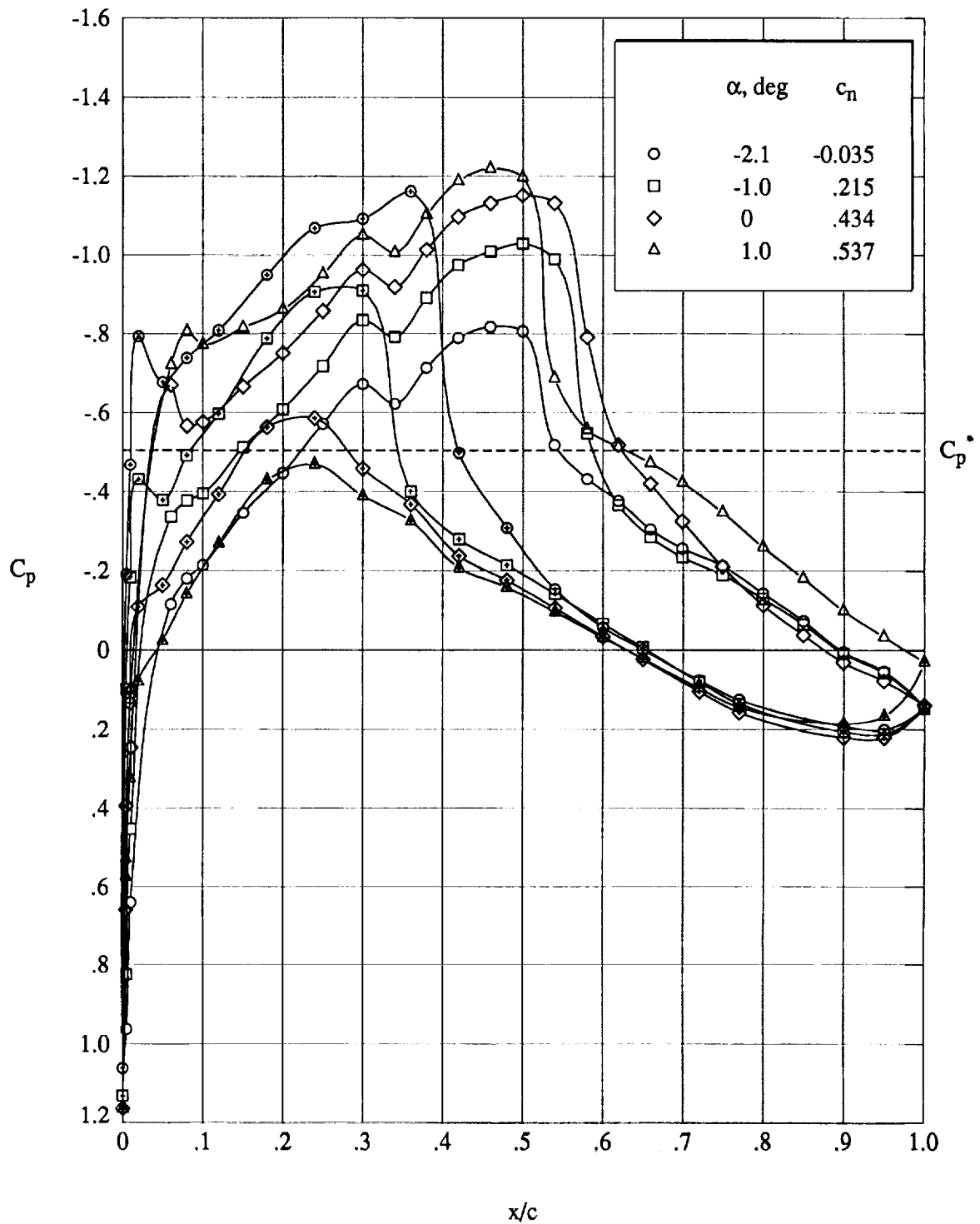
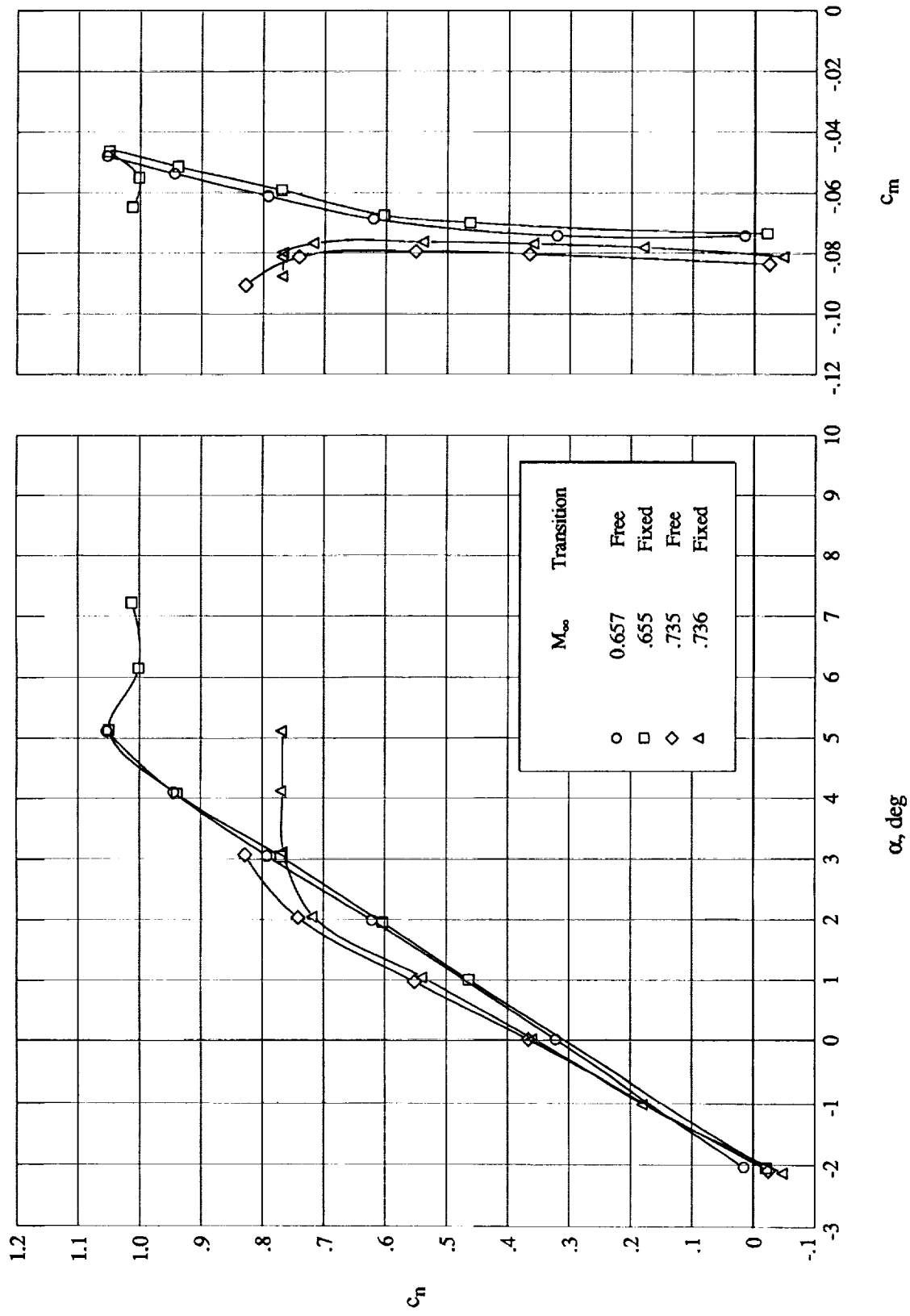
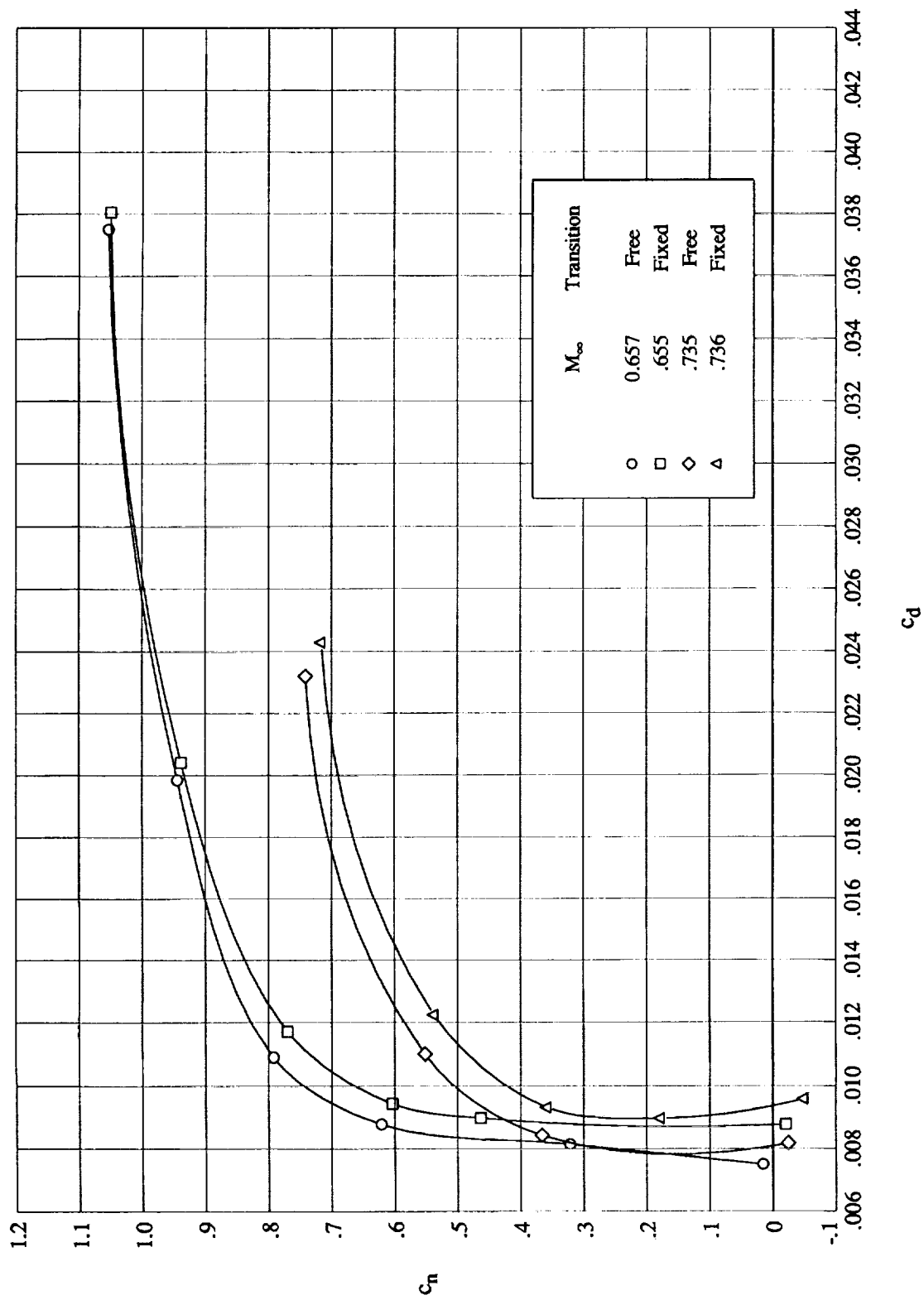


Figure 24. Effect of angle of attack at $M_\infty \approx 0.780$ and $R_c = 9.0 \times 10^6$. Open symbols denote upper surface; "+" within symbol denotes lower surface.



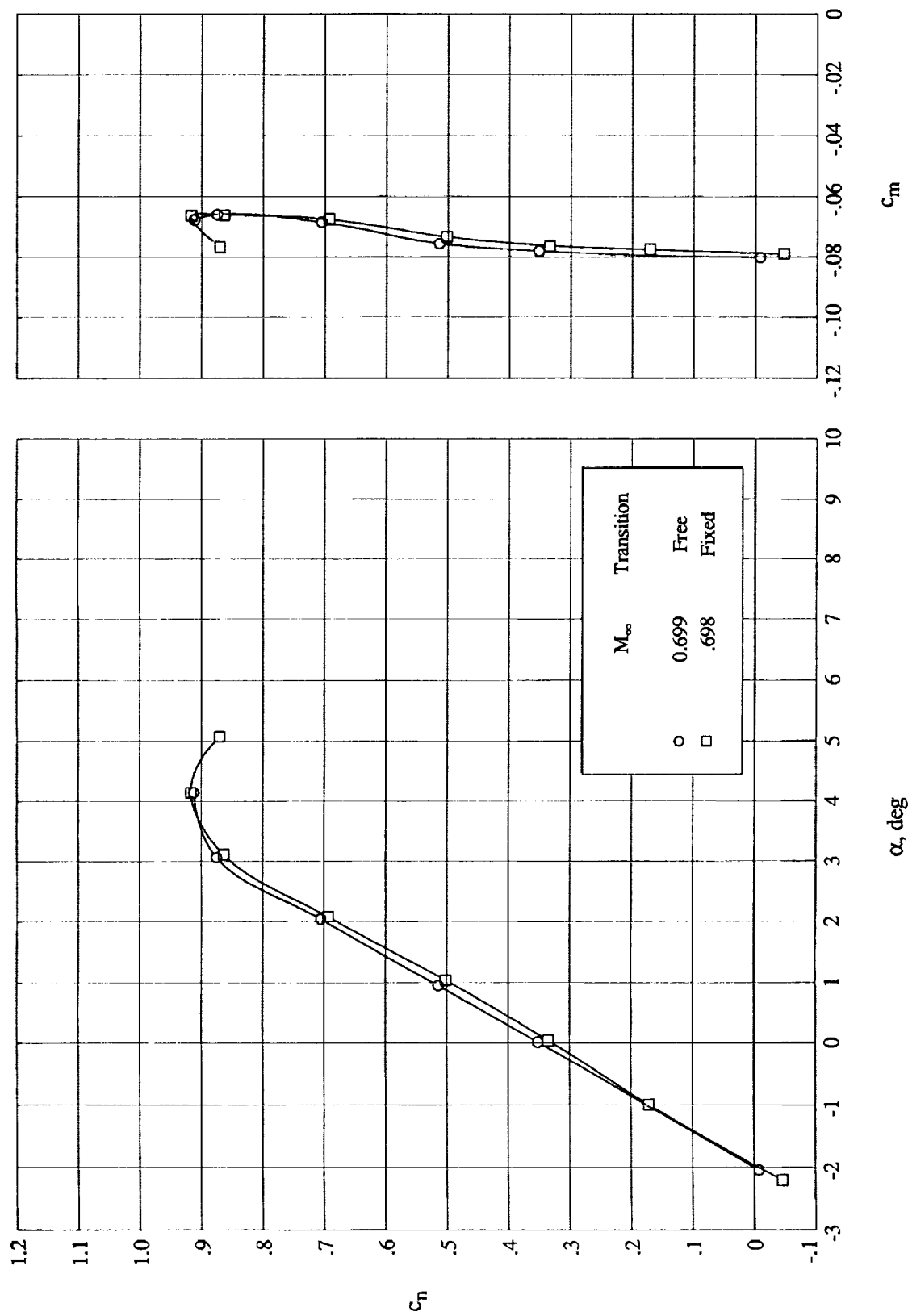
(a) Normal-force and pitching-moment coefficients. $R_c = 4.5 \times 10^6$.

Figure 25. Effect of fixed transition.



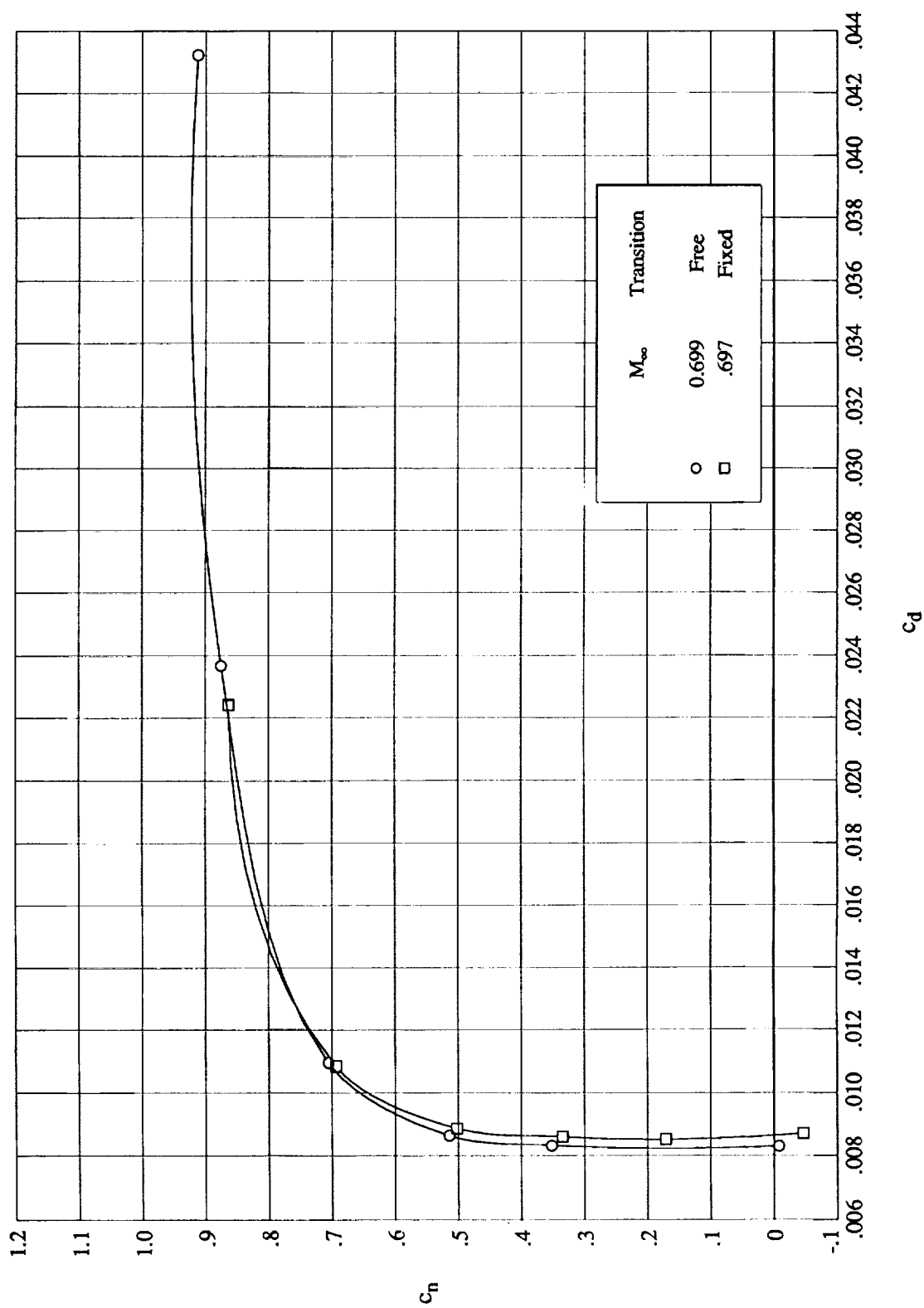
(b) Drag coefficient. $R_c = 4.5 \times 10^6$.

Figure 25. Continued.



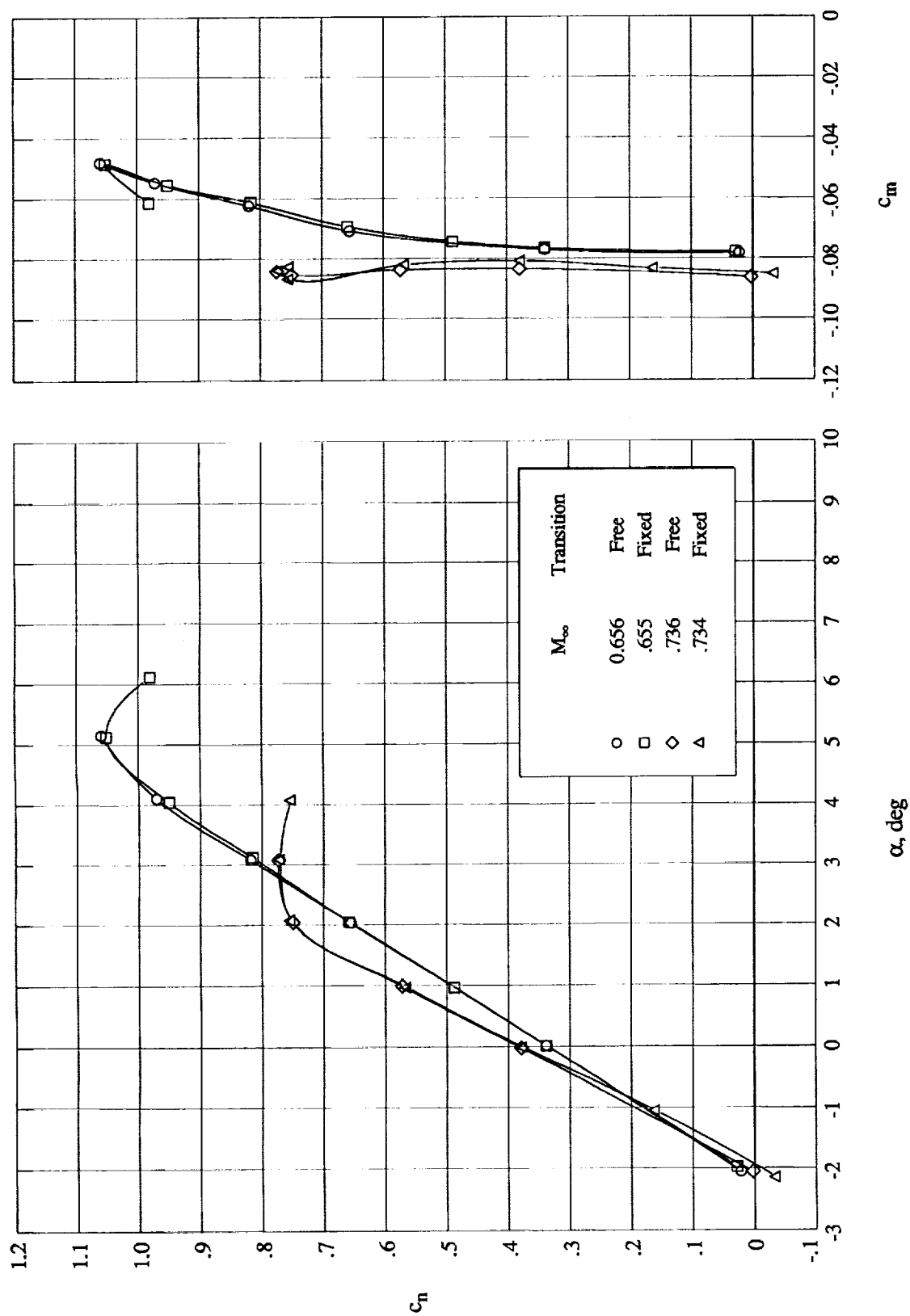
(c) Normal-force and pitching-moment coefficients. $R_e = 6.5 \times 10^6$.

Figure 25. Continued.



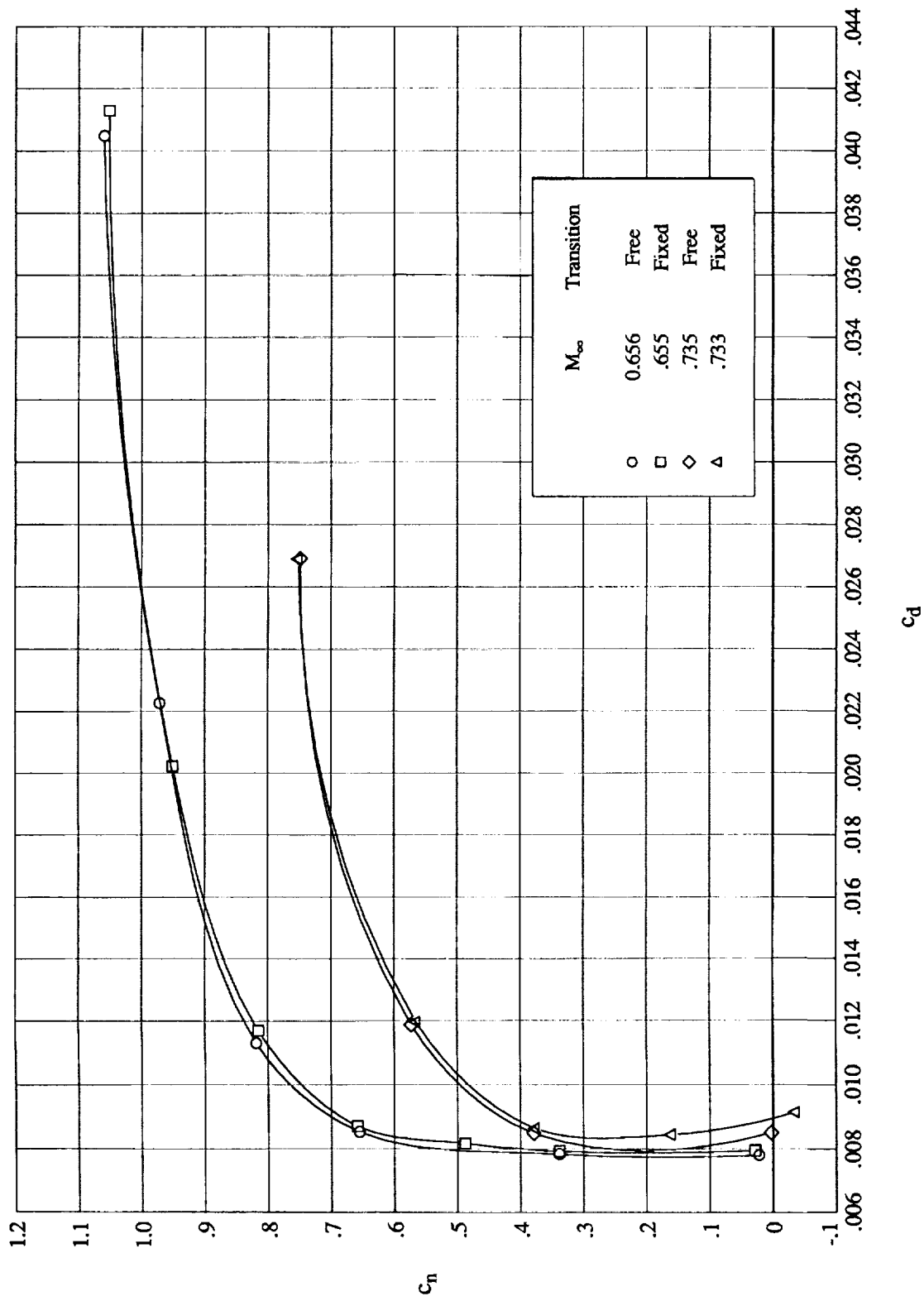
(d) Drag coefficient. $R_c = 6.5 \times 10^6$.

Figure 25. Continued.



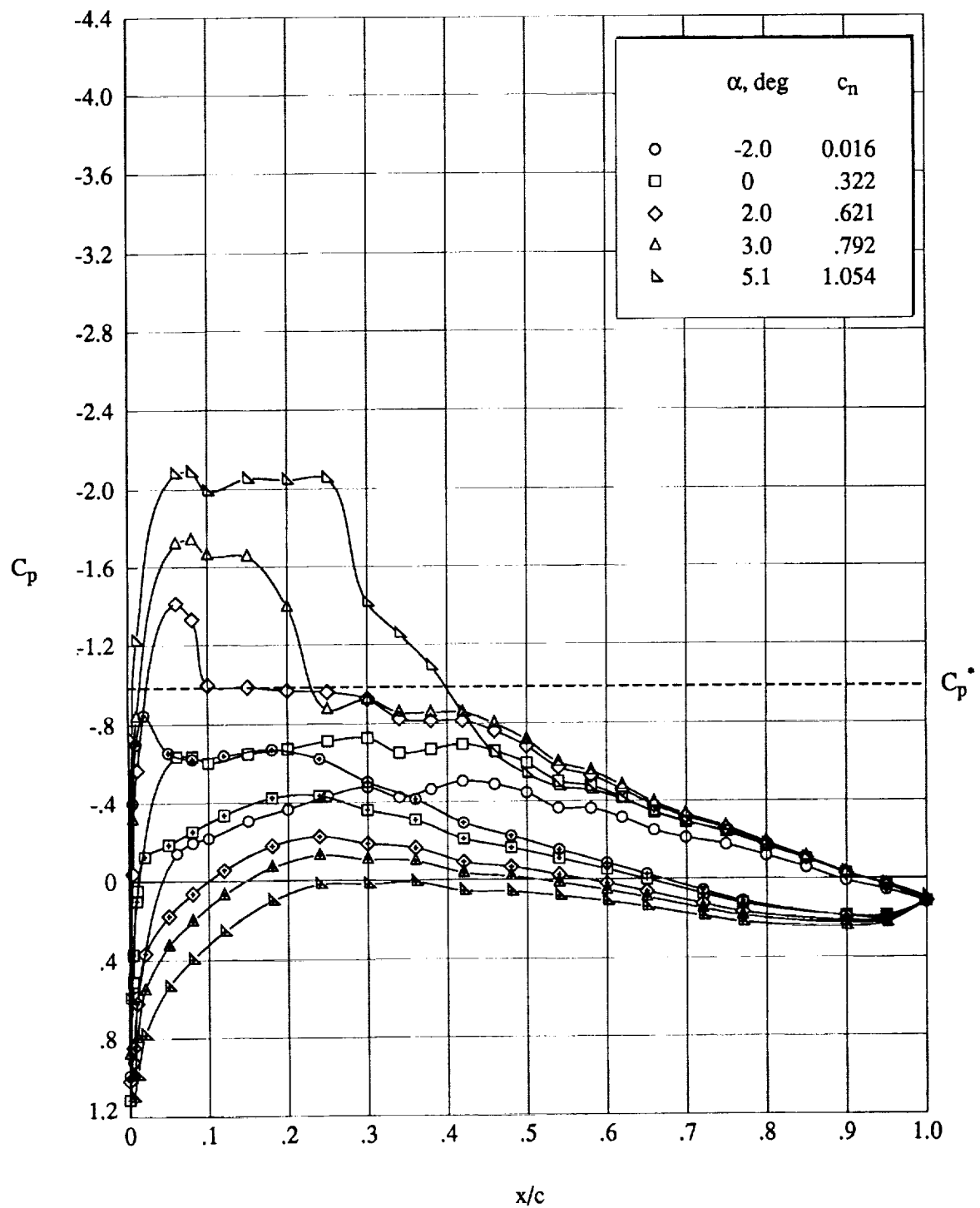
(e) Normal-force and pitching-moment coefficients. $R_c = 9.0 \times 10^6$.

Figure 25. Continued.



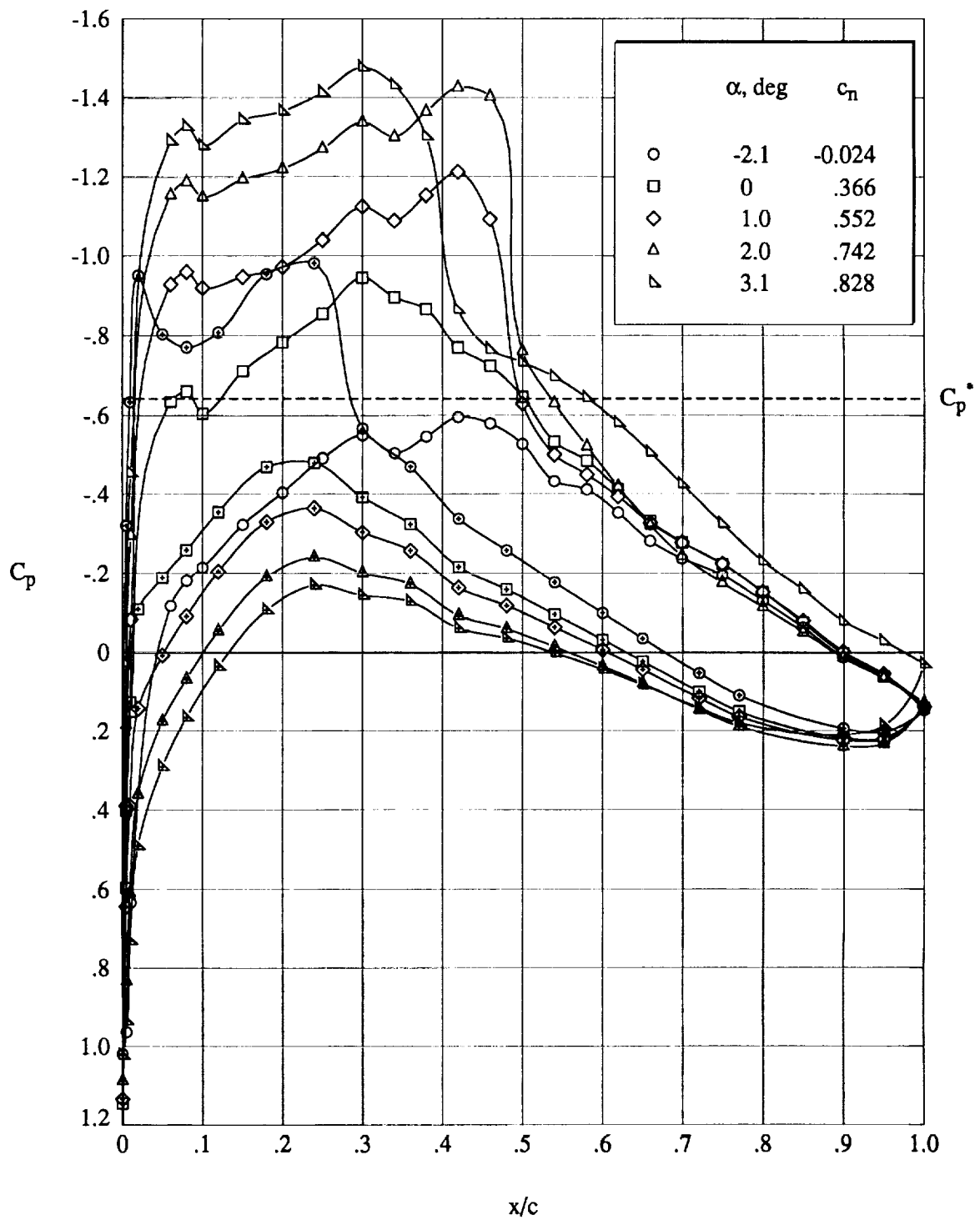
(f) Drag coefficient. $R_c = 9.0 \times 10^6$.

Figure 25. Concluded.



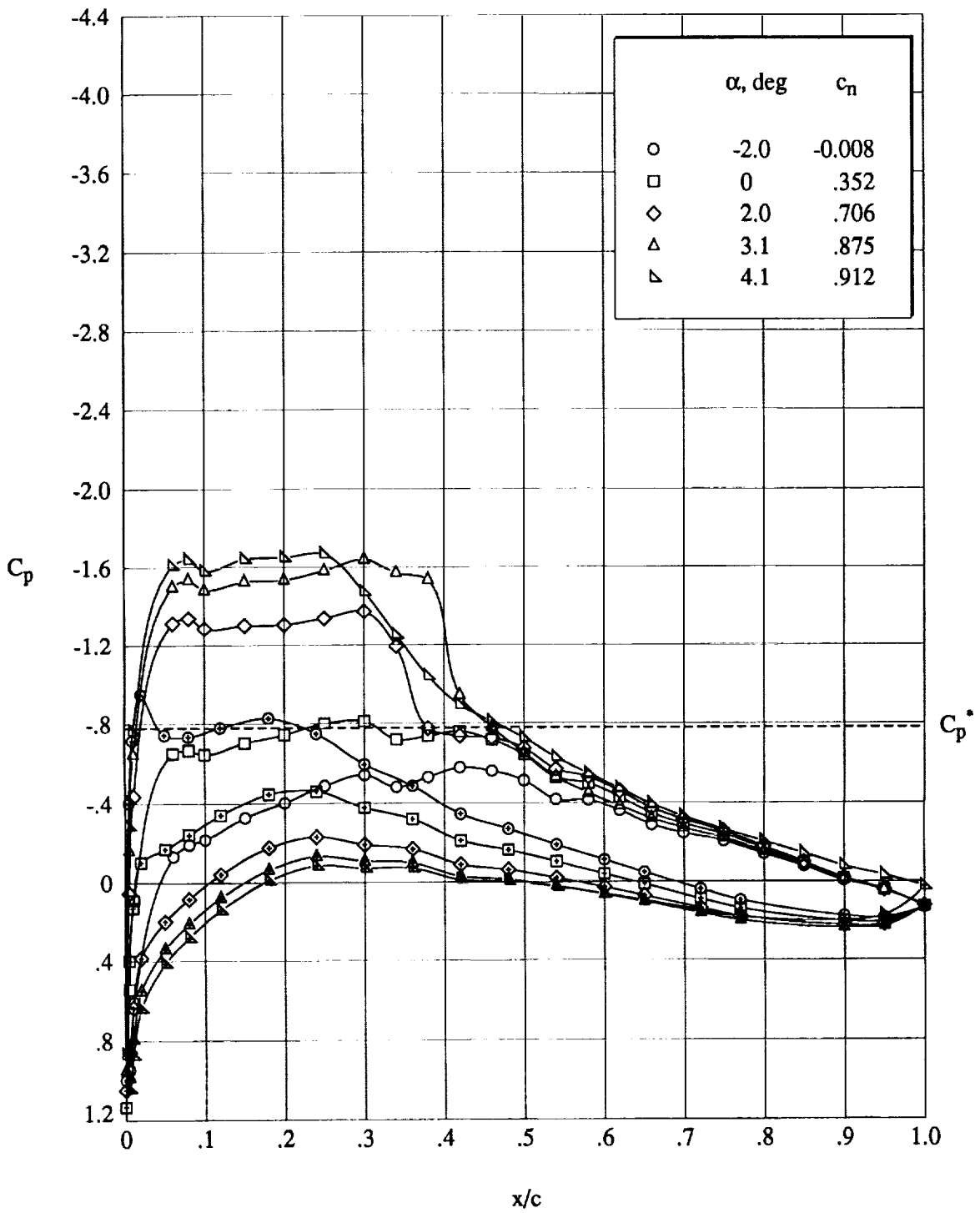
(a) $M_\infty \approx 0.655$; $R_c = 4.5 \times 10^6$.

Figure 26. Effect of angle of attack with free transition. Open symbols denote upper surface; "+" within symbol denotes lower surface.



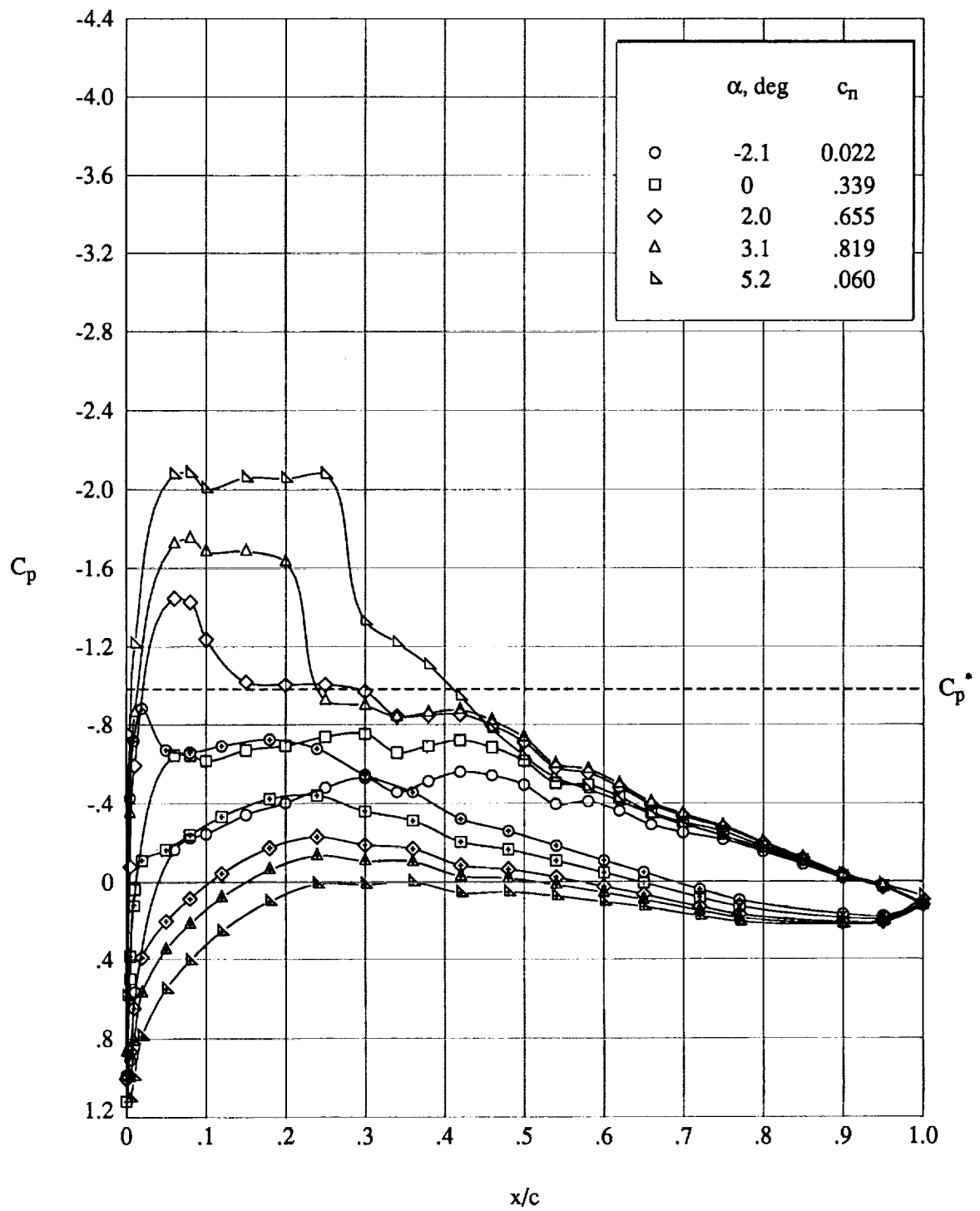
(b) $M_\infty \approx 0.735$; $R_c = 4.5 \times 10^6$.

Figure 26. Continued.



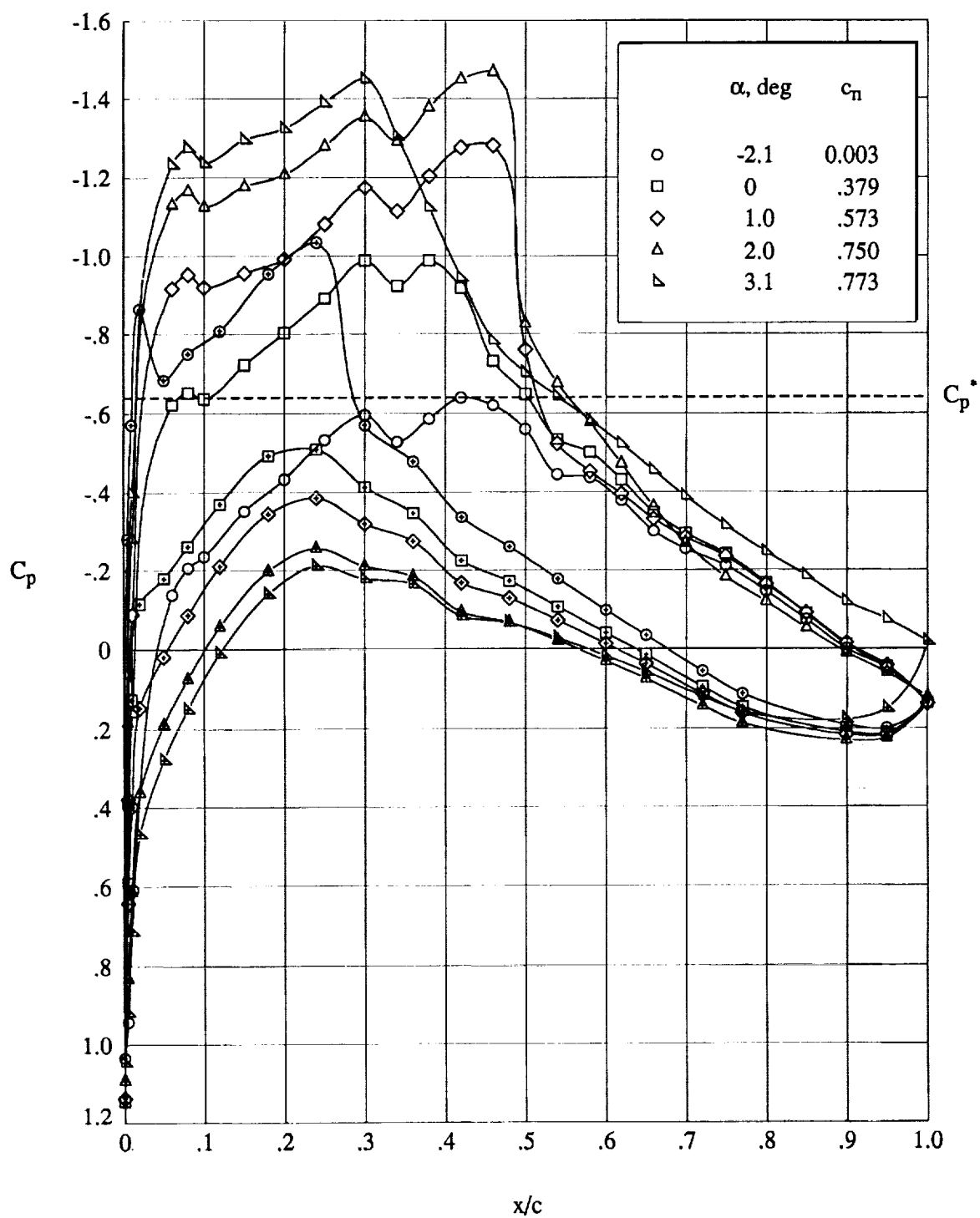
(c) $M_\infty \approx 0.700$; $R_c = 6.5 \times 10^6$.

Figure 26. Continued.



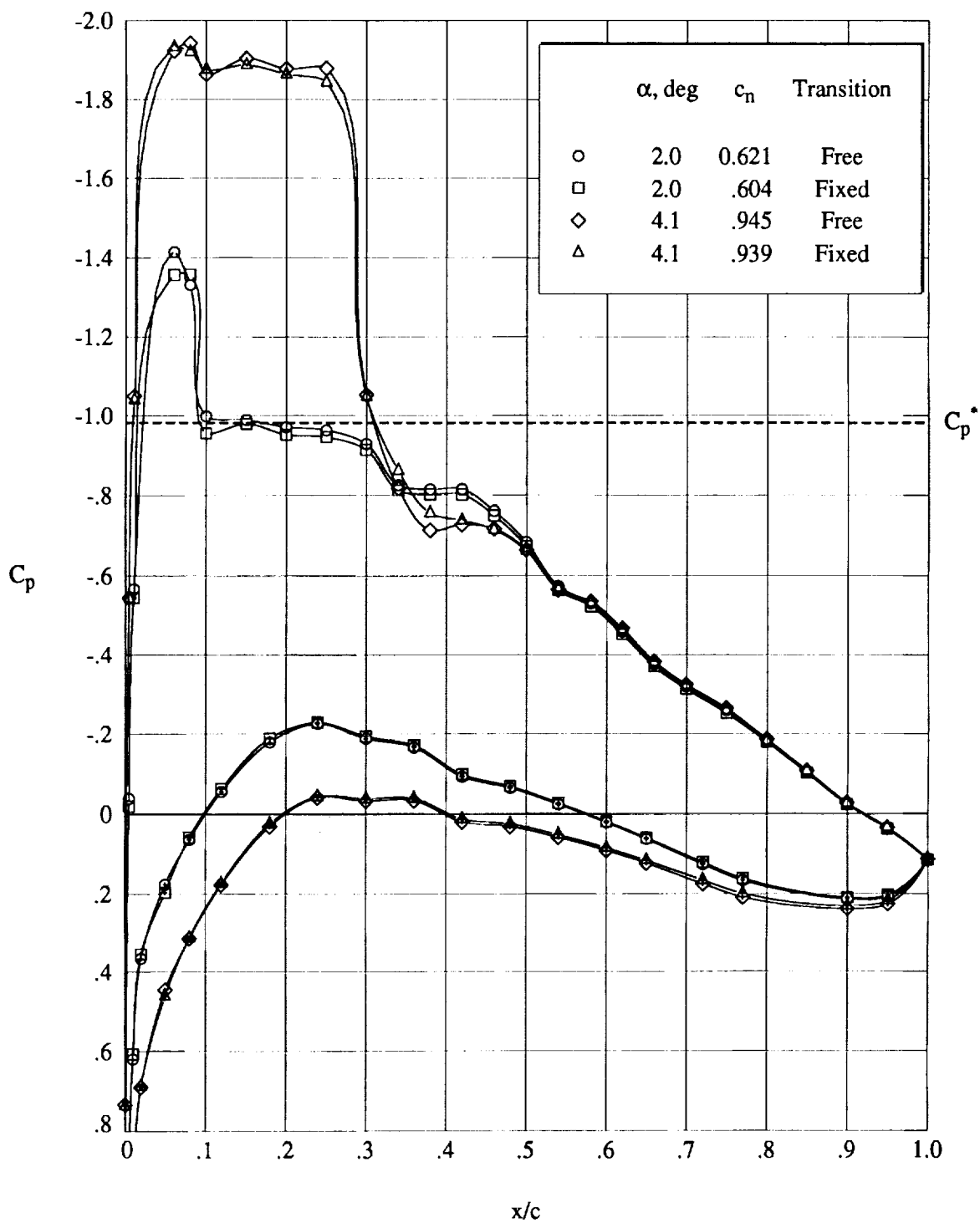
(d) $M_\infty \approx 0.655$; $R_c = 9.0 \times 10^6$.

Figure 26. Continued.



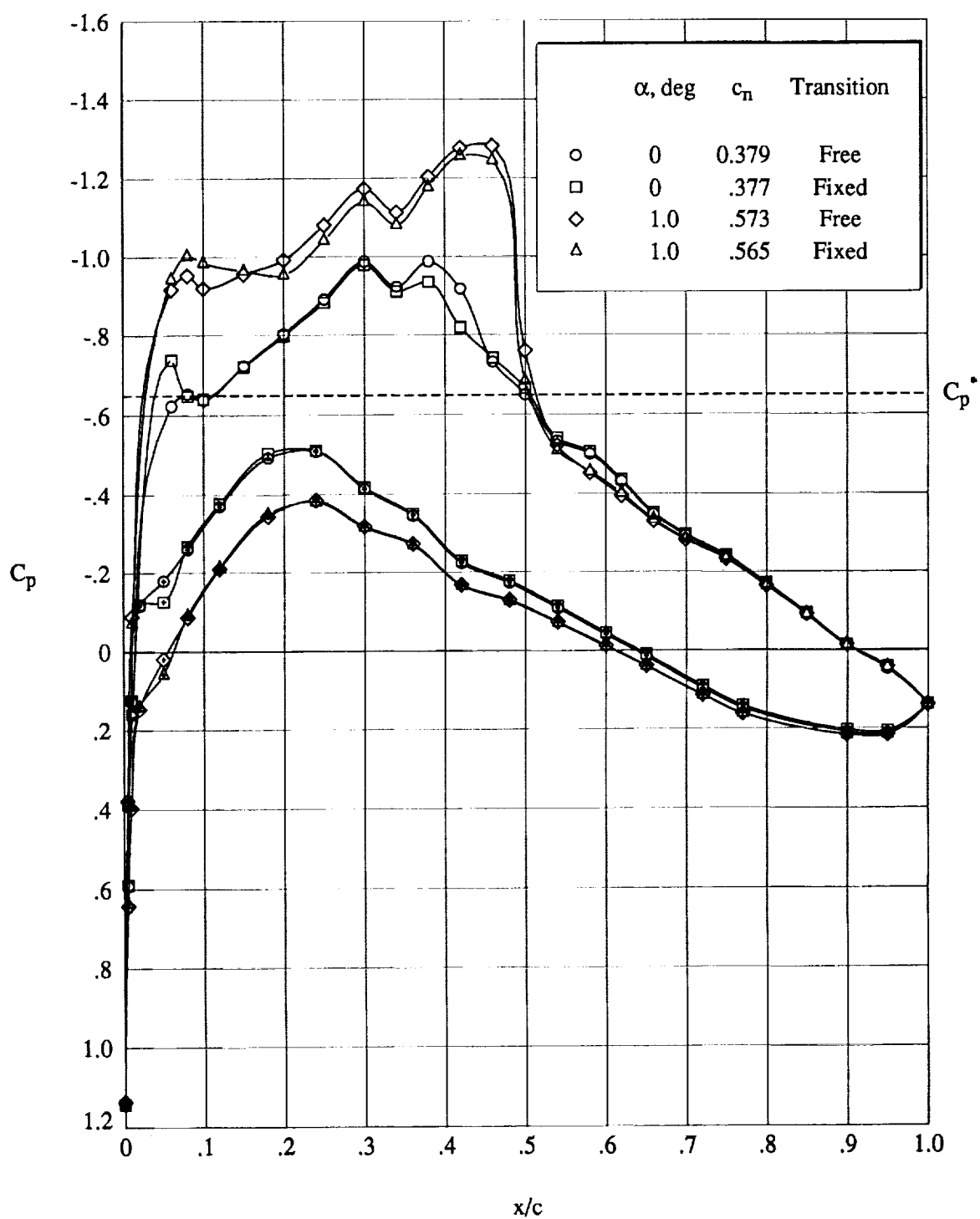
(e) $M_\infty \approx 0.735$; $R_e = 9.0 \times 10^6$.

Figure 26. Concluded.



(a) $M_\infty \approx 0.655$; $R_c = 4.5 \times 10^6$.

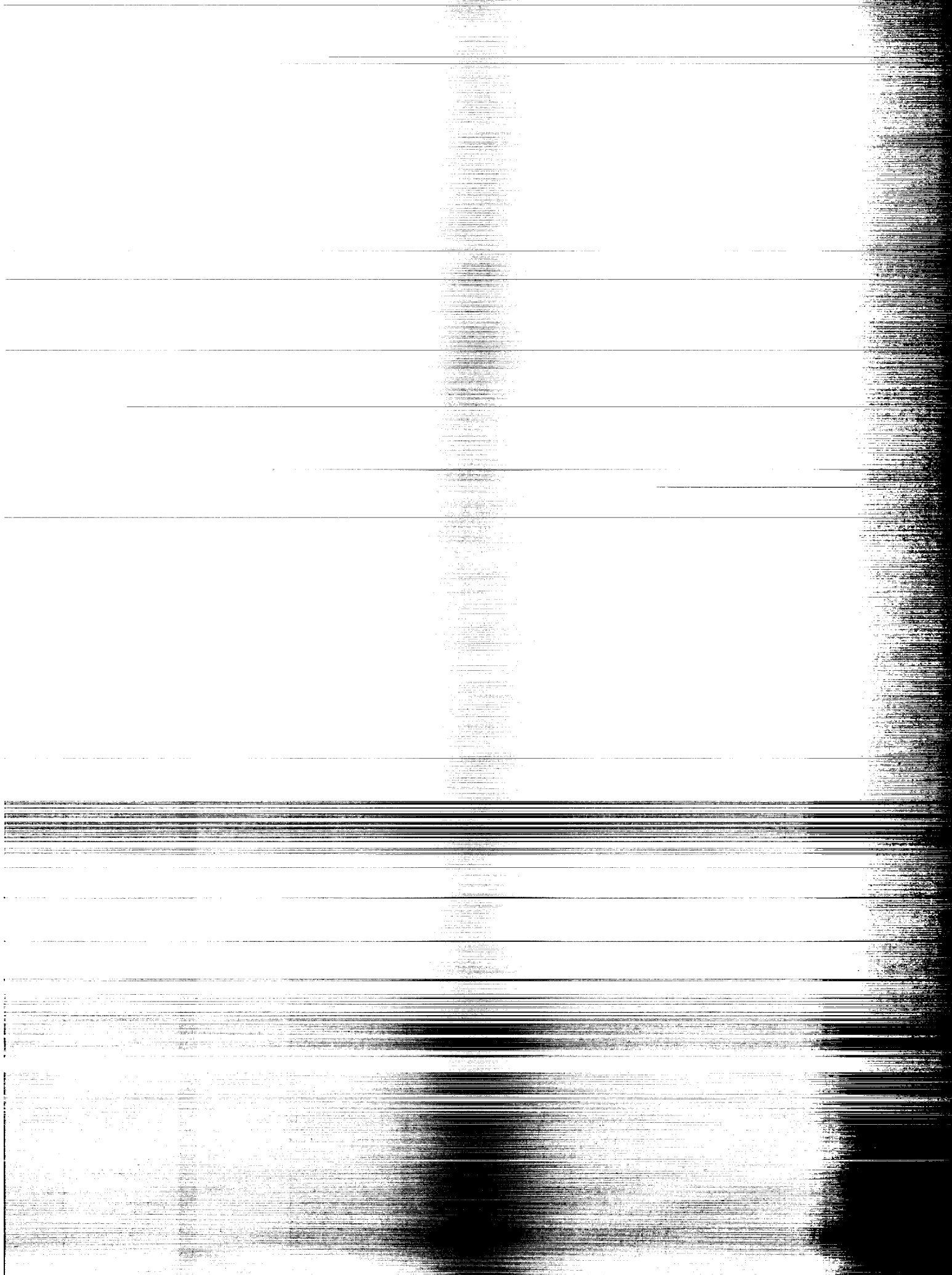
Figure 27. Effect of fixed transition on pressure distributions. Open symbols denote upper surface; "+" within symbol denotes lower surface.



(b) $M_\infty \approx 0.735$; $Re = 9.0 \times 10^6$.

Figure 27. Concluded.

REPORT DOCUMENTATION PAGE			Form Approved OMB No. 0704-0188	
Public reporting burden for this collection of information is estimated to average 1 hour per response, including the time for reviewing instructions, searching existing data sources, gathering and maintaining the data needed, and completing and reviewing the collection of information. Send comments regarding this burden estimate or any other aspect of this collection of information, including suggestions for reducing this burden, to Washington Headquarters Services, Directorate for Information Operations and Reports, 1215 Jefferson Davis Highway, Suite 1204, Arlington, VA 22202-4302, and to the Office of Management and Budget, Paperwork Reduction Project (0704-0188), Washington, DC 20503.				
1. AGENCY USE ONLY(Leave blank)		2. REPORT DATE December 1993		3. REPORT TYPE AND DATES COVERED Technical Memorandum
4. TITLE AND SUBTITLE Aerodynamic Characteristics and Pressure Distributions for an Executive-Jet Baseline Airfoil Section			5. FUNDING NUMBERS WU 505-59-10-30	
6. AUTHOR(S) Dennis O. Allison and Raymond E. Mineck				
7. PERFORMING ORGANIZATION NAME(S) AND ADDRESS(ES) NASA Langley Research Center Hampton, VA 23681-0001			8. PERFORMING ORGANIZATION REPORT NUMBER L-17228	
9. SPONSORING/MONITORING AGENCY NAME(S) AND ADDRESS(ES) National Aeronautics and Space Administration Washington, DC 20546-0001			10. SPONSORING/MONITORING AGENCY REPORT NUMBER NASA TM-4529	
11. SUPPLEMENTARY NOTES				
12a. DISTRIBUTION/AVAILABILITY STATEMENT Unclassified-Unlimited Subject Category 02			12b. DISTRIBUTION CODE	
13. ABSTRACT (Maximum 200 words) A wind tunnel test of an executive-jet baseline airfoil model was conducted in the adaptive-wall test section of the NASA Langley 0.3-Meter Transonic Cryogenic Tunnel. The primary goal of the test was to measure airfoil aerodynamic characteristics over a wide range of flow conditions that encompass two design points. The two design Mach numbers were 0.654 and 0.735 with corresponding Reynolds numbers of 4.5×10^6 and 8.9×10^6 based on chord, respectively, and normal-force coefficients of 0.98 and 0.51, respectively. The tests were conducted over a Mach number range from 0.250 to 0.780 and a chord Reynolds number range from 3×10^6 to 18×10^6 . The angle of attack was varied from -2° to a maximum below 10° with one exception in which the maximum was 14° for a Mach number of 0.250 at a chord Reynolds number of 4.5×10^6 . Boundary-layer transition was fixed at 5 percent of chord on both the upper and lower surfaces of the model for most of the test. The adaptive-wall test section had flexible top and bottom walls and rigid sidewalls. Wall interference was minimized by the movement of the adaptive walls, and the airfoil aerodynamic characteristics were corrected for any residual top and bottom wall interference.				
14. SUBJECT TERMS Airfoil section; Pressure distributions; Aerodynamic characteristics; Transonic conditions; Executive jet; Business jet			15. NUMBER OF PAGES 103	
			16. PRICE CODE A06	
17. SECURITY CLASSIFICATION OF REPORT Unclassified		18. SECURITY CLASSIFICATION OF THIS PAGE Unclassified		19. SECURITY CLASSIFICATION OF ABSTRACT
				20. LIMITATION OF ABSTRACT



National Aeronautics and
Space Administration
Langley Research Center
Mail Code 180
Hampton, VA 23681-00001

Official Business
Penalty for Private Use, \$300

BULK RATE
POSTAGE & FEES PAID
NASA
Permit No. G-27